UNIVERSITY OF LEEDS

Characterisation and State Estimation of Magnetic Soft Continuum Robots

Tomás da Veiga

Submitted in accordance with the requirements for the degree of Doctorate of Philosophy

The University of Leeds

Faculty of Engineering

School of Electronic and Electrical Engineering

August 2023

Abstract

Minimally invasive surgery has become more popular as it leads to less bleeding, scarring, pain, and shorter recovery time. However, this has come with counter-intuitive devices and steep surgeon learning curves. Magnetically actuated Soft Continuum Robots (SCR) have the potential to replace these devices, providing high dexterity together with the ability to conform to complex environments and safe human interactions without the cognitive burden for the clinician. Despite considerable progress in the past decade in their development, several challenges still plague SCR hindering their full realisation. This thesis aims at improving magnetically actuated SCR by addressing some of these challenges, such as material characterisation and modelling, and sensing feedback and localisation.

Material characterisation for SCR is essential for understanding their behaviour and designing effective modelling and simulation strategies. In this work, the material properties of commonly employed materials in magnetically actuated SCR, such as elastic modulus, hyper-elastic model parameters, and magnetic moment were determined. Additionally, the effect these parameters have on modelling and simulating these devices was investigated.

Due to the nature of magnetic actuation, localisation is of utmost importance to ensure accurate control and delivery of functionality. As such, two localisation strategies for magnetically actuated SCR were developed, one capable of estimating the full 6 degrees of freedom (DOFs) pose without any prior pose information, and another capable of accurately tracking the full 6-DOFs in real-time with positional errors lower than 4 mm. These

will contribute to the development of autonomous navigation and closed-loop control of magnetically actuated SCR.

Contents

List of Figures

List of Tables

Chapter 1

Introduction

Minimally invasive procedures have been at the forefront of the surgical revolution of the past century. This push has mainly put the patient at its core by reducing bleeding, scarring, post-operative pain and recovery time. This has seen the advent of endoscopes and catheters, which are able to enter the patient's body through natural orifices, or small incisions. The development of these tools, however, has not been kind to surgeons, requiring high dexterity and steep learning curves, especially when the target is of difficult access. Robotics, with its computation and dexterous intelligence, has the potential to reduce this cognitive burden and enable access to challenging anatomical areas. In fact, the development of continuum robots to reach deeper inside the anatomy in a minimally invasive way has recently become a hot topic of research [1].

Due to the nature of such robots, a key factor in their development is safety and scalability. This has attracted the use of soft materials which are inherently safe for human interaction and able to conform to their environment. Three main types of actuation have been reported in soft continuum robots (SCR): mechanical (e.g. concentric tube) [2], fluidic (e.g. pneumatic) [3], and magnetic [4]. One of the main differences between these is that both mechanical and fluidic actuation require tethering, while magnetic actuation is achieved remotely and contact free. Additionally, mechanical and fluidic dexterity are directly proportional to diameter due to the need for additional cables and fluidic

chambers respectively. For these reasons, the interest in magnetically actuated robots has exploded over recent decades, as it allows for the delivery of the robot to areas of limited access in the human body [5; 6; 7; 8; 9; 10]. However, this tetherless and remote actuation requires accurate localisation of the robot in order to ensure controlled actuation, delivery of functionally and ultimately closed-loop control [11; 12; 13].

Magnetic actuation relies on placing a magnetically responsive robot under external magnetic fields. These fields and their gradients generate a torque and force respectively on the robot, providing actuation [14]. Both the generation of the external magnetic fields, as well as conferring magnetic properties onto the robot, can be done in several ways. Catheters containing small permanent magnets at their tip have long been in the market and used for cardiac ablation [15; 16]. However, in a push to deliver smaller robots with a more continuous magnetic profile, the use of magnetic micro- or nano-particles has risen in popularity [10]. The use of magnetically hard [17; 4], soft [18; 19], and superparamagnetic [20; 21] particles has been described. A key difference between these types of magnetic materials is their ability to, or lack of, retaining magnetisation after the removal of a saturating magnetic field [4]. Hard-magnetic materials are able to retain this magnetisation, and therefore, can be seen as having a constant magnetic moment. This makes their actuation and control more intuitive, whereas soft and superparamagnetic materials must rely on geometry patterning in order to achieve enhanced functionality [20; 21]. Soft and superparamgnetic materials however, allow smaller particle sizes enabling further fabrication techniques and miniaturisation to the nano-scale [20].

Lastly, generating these external magnetic fields can be done with either coil systems or external permanent magnets (EPM) [22; 23; 24; 25; 26]. Coil-based systems are more intuitive as the relationship between current and generated magnetic field is linear and well-defined, allowing for easier and quickly implemented magnetic field strategies such as oscillating or rotating magnetic fields [27; 28]. However, they suffer from small workspace dimensions, high energy consumption and require cooling systems. Conversely, the use of EPM mounted on the end effectors of robotic arms is a viable solution as it provides large workspace compatible with surgical procedures and low energy consumption [24; 29].

However, it suffers from complex control and actuation strategies, due to the highly non-linear magnetic fields generated [30].

This present thesis' overall aim is to improve and advance the capabilities of surgical SCR, more specifically magnetically actuated SCR, through the development of a magnetically actuated SCR compatible with real-time pose tracking. A schematic representation of the system can be seen in Figure 1.1.

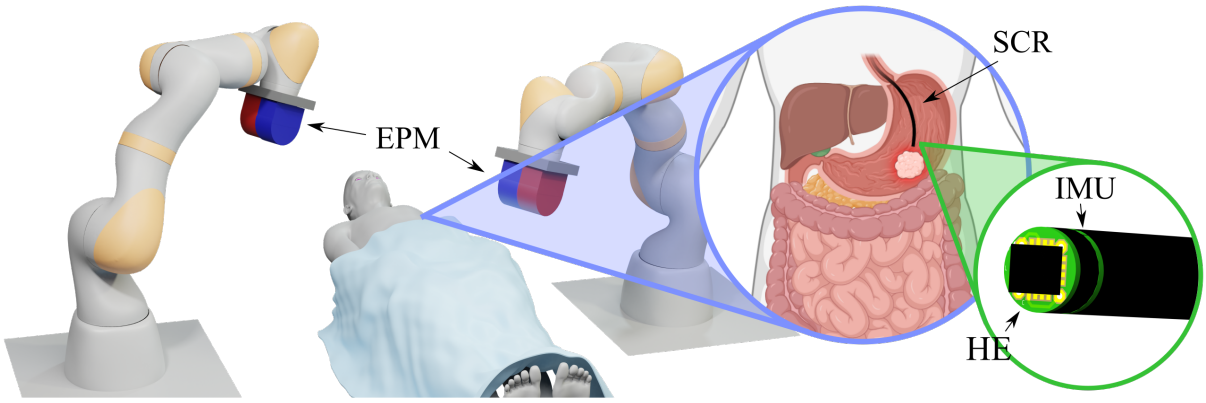

Figure 1.1: SCR for minimally invasive surgery actuated via 2 EPMs mounted on robotic arms. The SCR contains and Hall effect sensor (HE) and an inertial measurement unit (IMU) for real-time pose tracking.

This was achieved through three main areas of interest and development which are detailed over the following subsections. The main goal of each area is as follows:

- **Literature Review:** Carry a deep look into the literature and state-of-the-art of medical continuum robots, and identify the gaps in the research and development of such robots. This will provide the foundation of knowledge needed to develop the next generation of magnetically actuated SCR.

- **Materials and Fabrication of magnetically actuated SCR:** Identify commonly employed soft materials and fabrication techniques, and characterise and model these materials' mechanical and magnetic behaviour. This will allow the fabrication and prototyping of the SCR, as well as information on the expected behaviour when under actuation.

- **Pose estimation of magnetically actuated SCR:** Develop localisation tech-

niques for magnetically actuated robots under multiple EPM control which are compatible with closed-loop control. This will effectively allow the tracking of the SCR when under actuation, contributing to accurate actuation, closed-loop control, and delivery of functionality.

1.1 Review of Medical Continuum Robots

The application of continuum robots to the medical field is a fairly new endeavour which has rapidly made progress. With the recent release of commercial systems based on this type of robots, such as the Monarch™or the Ion platforms, medical continuum robots are becoming a reality in the operating room. From bronchoscopy to endovascular interventions, continuum robots have the potential to completely change the panorama of surgical interventions.

Despite these achievements and clear potential, continuum robots suffer from specific issues due to their inherent design. From dexterity and scalability to modelling and sensory feedback, these robots still face challenges which prevent their full realisation.

Given this panorama, Chapter 2 serves to summarise the recent progress and developments in this field while highlighting the active areas of research and the challenges that these systems face. Starting with an overview of the main medical applications, the chapter progresses to showcasing the variety of actuation designs covering mechanical, fluidic, and magnetic methods. This is then followed by the challenges this field faces in terms of fabrication, modelling, control and sensing.

1.2 Material Characterization for Magnetic Soft Robots

Given the new and innovative nature of the topic, magnetically loaded silicone elastomers commonly employed in soft robots had not been studied in depth. This led to a lack of understanding of how these particles affect the raw material properties, but also the use of the undopped material parameters in modelling and simulation of such materials.

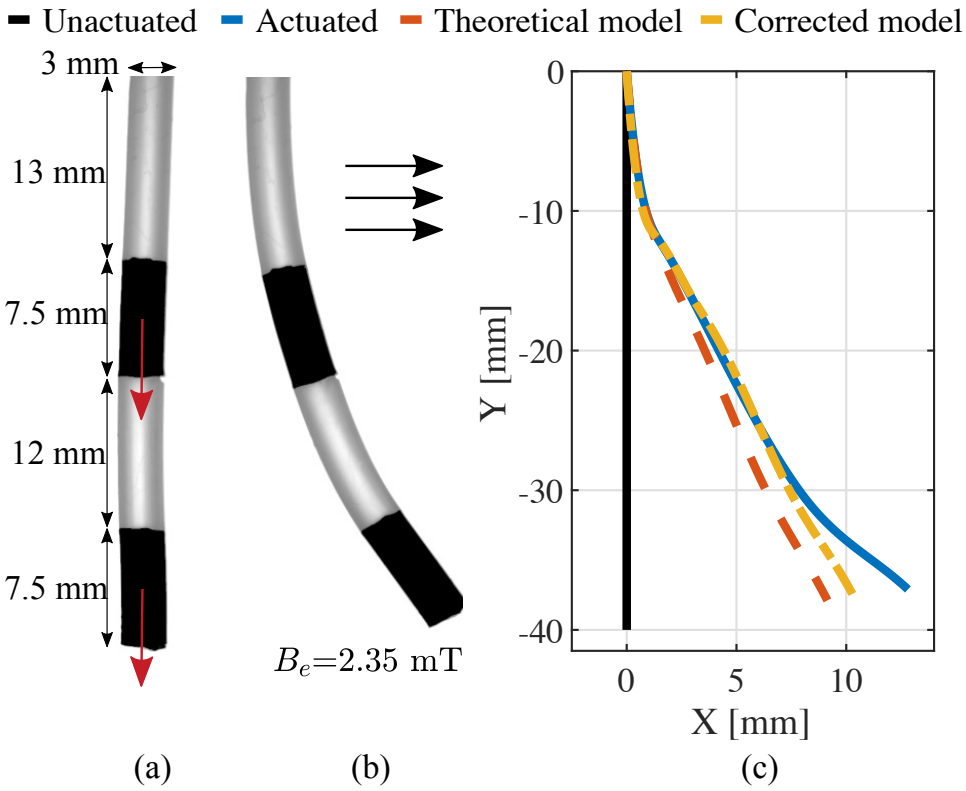

Figure 1.2: (a) Fully soft discrete magnetic continuum robot. The red arrows represent the direction of magnetization. (b) The robot under actuation in an uniform magnetic field with direction represented by the black arrows. (c) Simulation results considering our correct model and the theoretical model.

Since the use of the right material parameters is fundamental in the modelling and simulation of soft robots to ensure accurate actuation and control strategies, a material characterisation, both in the mechanical and magnetic domains, of commonly employed magnetic elastomers was carried. Chapter 3 introduces this characterisation. Two different elastomers with varying concentrations of hard magnetic particles were characterised. The mechanical characterisation consisted on uni-axial tensile testing, and subsequent hyper-modelling fitting on the resulting stress-strain curves. The magnetic characterisation saw the development of a novel magnetic characterisation technique based on a 6 degrees-of-freedom (DOF) load cell. By measuring the force and torque exerted on an elastomeric sample by an external magnetic field, the magnetisation vector, and therefore the material's magnetic remanence, can be found. Lastly, the effect that accurate material parameters have on the modelling and simulation of SCRs was assessed. SCRs were fabrication and actuated under homogeneous fields. Two simulation models, one

with theoretical values and one with the experimental measured values, were matched to the observed real actuation, as shown in Figure 1.2. Simulation errors were reduced from 8.5% to 5.4% when using accurate material models.

1.3 Pose estimation of Magnetically Actuated Robots

As mentioned earlier, due to the nature of the contact-free actuation mode, magnetically actuated robots need localisation in order to ensure accurate actuation, closed-loop control, and delivery of functionality [11].

As such, localisation of magnetic robots has long been a big topic of research [12]. Several localisation methods based on imaging modalities, such as fluoroscopy [31], ultrasound [32; 33; 34], and MRI [35], have been reported with varying number of DOF, accuracy, and refresh rate. Despite promising results, these methods require additional equipment into the operating theatre with added costs and footprint. Additionally, methods based on fluoroscopy expose the patient and physician to harmful radiation making them incompatible with closed-loop control. Localisation based on magnetic field measurements has long been in use but commercial systems are incompatible with magnetic actuation systems. The use of magnetic fields for both actuation and localisation of medical robots has gained a lot of attention as it simplifies the system without the need for additional localisation equipment [36; 37; 38].

The placement of the magnetic field sensors, such as Hall effect (HE), can either be internal or external to the robot. External methods rely on the placement of magnetic field sensor arrays somewhere within the workspace. By measuring the change in magnetic field, these are able to track the device [39; 40; 41]. These easily allow miniaturisation and tetherless actuation. However, the size of the array limits the workspace dimensions, it requires calibration of a large amount of sensors, as well as high sensitivity sensor or very magnetically strong devices in order to accurately measure their magnetic fields. Alternatively, internal methods see the embedding of the magnetic field sensor together with an inertial measuring unit (IMU) inside the device [38]. This greatly reduces the

number of sensors needed, it does not restrict the workspace dimensions, and eliminates the need for any localisation-specific internal magnetic requirement. Even though miniaturisation is more challenging for internal methods, when considering magnetic actuation platforms with large workspaces and particle based continuum robots, these are better suited.

The problem of localising the full 6 DOF pose can be split into finding the 3D position, and finding the 3D orientation. Common orientation methods use the Earth's gravity and magnetic field as an inertial reference frame, and a gyroscope reading the angular velocities. However, in a magnetic actuation system the Earth's magnetic field is not measurable, loosing the reference for the rotation around gravity. Although, a homogeneous actuation magnetic field could be used instead, provided it is not parallel to gravity, this would make the estimation of position impossible, as this requires non-homogeneous magnetic fields. If instead, non-homogeneous magnetic fields are generated, then, either the position or the orientation must be known to solve the other. This makes the problem not solvable, as a single measurement of magnetic field, gravity, and angular velocity, are not enough for the full estimation of position and orientation. However, if the orientation is initialised accurately, then the accelerometer and gyroscope are able to track the change in orientation. This, together with a measurement of the magnetic field, makes the estimation of position possible.

These issues with magnetic localisation have been explored in detail for systems with a single EPM [38]. However, as platforms move into the addition of multiple EPMs, new localisation strategies which take into account and leverage for this are needed. Chapter 4 first looks into how the number of EPMs in a given system affects the localisation within its workspace. It then continues to the development of a localisation observer which is able to estimate the full 6 DOF pose by taking multiple measurements of the magnetic field for different EPM configurations. This was then implemented and tested on a quasi-static device. Building on top of this, Chapter 5 sees the development of a real-time 6 DOF localisation algorithm. This algorithm relies on accurate initialisation of the orientation, which can be done with the algorithm described in Chapter 4. This was then

implemented and tested on a magnetically actuated SCR, Figure 1.3. Additionally, the relative pose between two EPMs and the singularity regions induced across the workspace are analysed, and alternative EPM configurations which produce the same SCR deflection and tip position are found. The algorithm's update rate was of 280 Hz being compatible with closed-loop control, providing a stepping stone towards autonomous navigation and control of magnetically actuated continuum robots.

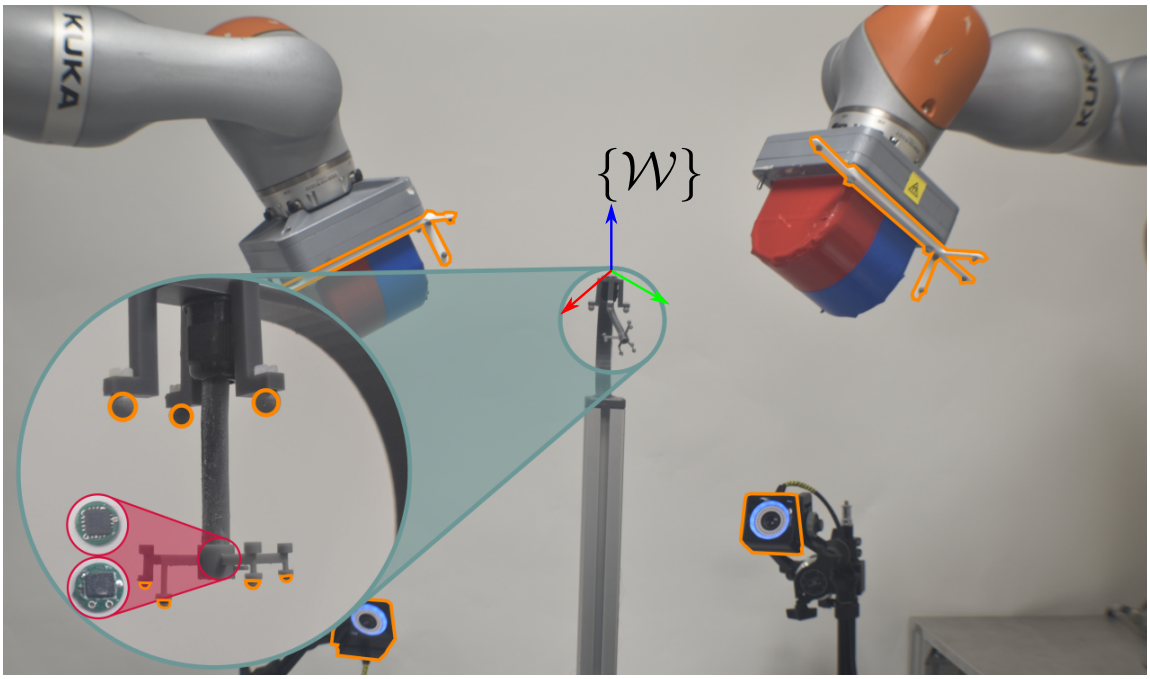

Figure 1.3: Soft Continuum Robot containing an IMU and Hall Effect sensor (in red) at the tip for localisation under two external permanent magnets.

1.4 Summary and Contributions

The thesis is structured into 6 additional chapters. The contributions of each are as follows

- **Chapter 2:** In-depth literature review on medical continuum robots, identifying the main challenges yet to solve across fabrication, modelling, control, and sensing.
- **Chapter 3:** Framework to characterise soft materials commonly employed in magnetic soft robots; best practices for accurate magnetic material modelling; effect of magnetic micro-particles on material behaviour; reduction of simulation errors by

37%.

- **Chapters 4:** Analysis of the effect that multiple EPMs on the workspace have on magnetic localisation as well as its update rate; six-DOF quasi-static localisation algorithm without the need of any prior pose information or the Earth's magnetic field; errors of 8 mm in norm position and update rate of 2.5 Hz.

- **Chapter 5:** Observability analysis and definition of singularity regions when 2 EPMs are present in the workspace; optimization of EPM configurations to achieve best localisation performance and actuation while avoiding singularity regions; implementation of a six-DOF localisation algorithm with running errors of 4 mm and update rate of 280 Hz.

- **Chapter 6:** Discussion of the main results from the previous chapters and their impact on the current state-of-the-art.

- **Chapter 7:** Final conclusions and future directions.

During the course of the PhD, I have had the opportunity to publish several papers and, as such, this is a thesis by publication. Therefore, Chapters 2, 3 and 4 are published, and Chapter 5 is currently under review, as of August 2023.

List of Publications The present thesis contains material from the following publications:

- **T. da Veiga**, J. H. Chandler, P. Lloyd, G. Pittiglio, N. J. Wilkinson, A. K. Hoshiar, R. A. Harris, and P. Valdastri, "Challenges of medical continuum robots in clinical context: a review", Progress in Biomedical Engineering, vol. 2, no. 3, pp. 032003, 2020.

- **T. da Veiga**, J. H. Chandler, G. Pittiglio, P. Lloyd, M. Holdar, O. Onaizah, A. Alazmani, and P. Valdastri, "Material Characterization for Magnetic Soft Robots", IEEE 4th International Conference on Soft Robotics (RoboSoft), pp. 335-342, 2021.

- **T. da Veiga**, G. Pittiglio, M. Brockdorff, J. H. Chandler, and P. Valdastri, "Six-

degree-of-freedom Localization Under Multiple Permanent Magnets Actuation", IEEE Robotics and Automation Letters, vol. 8, no. 6, pp. 3422 - 3429, 2023.

- **T. da Veiga**, M. Brockdorff, G. Pittiglio, J. H. Chandler, and P. Valdastri, "Magnetic Localization in Case of Manipulation by Two Permanent Magnets", IEEE Transactions on Robotics, Under Review - submitted March 2023

The following publications have also contributed to the work discussed in the present thesis:

- P. Lloyd, A. K. Hoshiar, **T. da Veiga**, A. Attanasio, N. Marahrens, J. H. Chandler, and P. Valdastri, "A Learnt Approach for the Design of Magnetically Actuated Shape Forming Soft Tentacle Robots", IEEE Robotics and Automation Letters, vol. 5, no. 3, pp. 3937-3944, 2020.

- G. Pittiglio, P. Lloyd, **T. da Veiga**, O. Onaizah, C. Pompili, J. Chandler, and P. Valdastri, "Patient-specific Magnetic Catheters for Atraumatic Autonomous Endoscopy", Soft Robotics, 2022.

- G. Pittiglio, M. Brockdorff, **T. da Veiga**, J. Davy, J. H. Chandler, P. Valdastri, "Collaborative Magnetic Manipulation via Two Robotically Actuated Permanent Magnets", IEEE Transactions on Robotics, 2022.

- S. Taccola, **T. da Veiga**, J. H. Chandler, O. Cespedes, P. Valdastri, and R. A. Harris, "Micro-scale Aerosol Jet Printing of Superparamagnetic Fe_3O_4 Nanoparticle Patterns", Scientific Reports, vol. 12, no. 1, pp. 17931, 2022.

- J. Davy, **T. da Veiga**, G. Pittiglio, J. H. Chandler, and P. Valdastri, "Independent Control of Two Magnetic Robots s using External Permanent Magnets: A Feasibility Study", 2023 International Symposium on Medical Robotics, 2023.

- G. Pittiligio, A. L. Orekhov , **T. da Veiga**, S. Calò, J. H. Chandler, N. Simaan, and P. Valdastri, "Closed Loop Static Control of Multi-Magnet Soft Continuum Robots", IEEE Robotics and Automation Letters, vol. 8, no. 3, pp. 3980-3987.

- Z. Koszowska, M. Brockdorff, **T. da Veiga**, G. Pittiglio, P. Lloyd, T. Khan-White, R.A. Harris, J.W. Moor, J.H. Chandler, P. Valdastri, "Independently Actuated Soft Magnetic Manipulators for Bimanual Operations in Confined Anatomical Cavities", Advanced Intelligent Systems, 2300062, 2023.

- G. Pittiligio, J. H. Chandler, **T. da Veiga**, Z. Koszowska, M. Brockdorff, P. Lloyd, K. Barry, R. Harris, J. McLaughlan, C. Pompili, and P. Valdastri, "Magnetic Personalized tentacles for targeted photothermal cancer therapy in peripheral lungs", Communications Engineering, 2, 50, 2023.

Bibliography

[1] P. E. Dupont, B. J. Nelson, M. Goldfarb, B. Hannaford, A. Menciassi, M. K. O'Malley, N. Simaan, P. Valdastri, and G.-Z. Yang, "A decade retrospective of medical robotics research from 2010 to 2020," *Science Robotics*, vol. 6, no. 60, p. eabi8017, 2021.

[2] H. Alfalahi, F. Renda, and C. Stefanini, "Concentric tube robots for minimally invasive surgery: Current applications and future opportunities," *IEEE Transactions on Medical Robotics and Bionics*, vol. 2, no. 3, pp. 410–424, 2020.

[3] P. Berthet-Rayne, S. H. Sadati, G. Petrou, N. Patel, S. Giannarou, D. R. Leff, and C. Bergeles, "Mammobot: A miniature steerable soft growing robot for early breast cancer detection," *IEEE Robotics and Automation Letters*, vol. 6, no. 3, pp. 5056–5063, 2021.

[4] Y. Kim and X. Zhao, "Magnetic soft materials and robots," *Chemical reviews*, vol. 122, no. 5, pp. 5317–5364, 2022.

[5] Y. Kim, G. A. Parada, S. Liu, and X. Zhao, "Ferromagnetic soft continuum robots," *Science Robotics*, vol. 4, no. 33, p. eaax7329, 2019.

[6] B. J. Nelson, S. Gervasoni, P. W. Chiu, L. Zhang, and A. Zemmar, "Magnetically

actuated medical robots: an in vivo perspective," *Proceedings of the IEEE*, vol. 110, no. 7, pp. 1028–1037, 2022.

[7] Y. Kim, E. Genevriere, P. Harker, J. Choe, M. Balicki, R. W. Regenhardt, J. E. Vranic, A. A. Dmytriw, A. B. Patel, and X. Zhao, "Telerobotic neurovascular interventions with magnetic manipulation," *Science Robotics*, vol. 7, no. 65, p. eabg9907, 2022.

[8] G. Pittiglio, P. Lloyd, T. da Veiga, O. Onaizah, C. Pompili, J. H. Chandler, and P. Valdastri, "Patient-specific magnetic catheters for atraumatic autonomous endoscopy," *Soft Robotics*, vol. 9, no. 6, pp. 1120–1133, 2022.

[9] J. Lussi, S. Gervasoni, M. Mattille, R. Dreyfus, Q. Boehler, M. Reinehr, N. Ochsenbein, B. J. Nelson, and U. Moehrlen, "Magnetically guided laser surgery for the treatment of twin-to-twin transfusion syndrome," *Advanced Intelligent Systems*, vol. 4, no. 11, p. 2200182, 2022.

[10] W. Hu, G. Z. Lum, M. Mastrangeli, and M. Sitti, "Small-scale soft-bodied robot with multimodal locomotion," *Nature*, vol. 554, no. 7690, pp. 81–85, 2018.

[11] J. W. Martin, B. Scaglioni, J. C. Norton, V. Subramanian, A. Arezzo, K. L. Obstein, and P. Valdastri, "Enabling the future of colonoscopy with intelligent and autonomous magnetic manipulation," *Nature machine intelligence*, vol. 2, no. 10, pp. 595–606, 2020.

[12] F. Bianchi, A. Masaracchia, E. Shojaei Barjuei, A. Menciassi, A. Arezzo, A. Koulaouzidis, D. Stoyanov, P. Dario, and G. Ciuti, "Localization strategies for robotic endoscopic capsules: a review," *Expert review of medical devices*, vol. 16, no. 5, pp. 381–403, 2019.

[13] J. W. Martin, L. Barducci, B. Scaglioni, J. C. Norton, C. Winters, V. Subramanian, A. Arezzo, K. L. Obstein, and P. Valdastri, "Robotic autonomy for magnetic endoscope biopsy," *IEEE Transactions on Medical Robotics and Bionics*, vol. 4, no. 3, pp. 599–607, 2022.

[14] J. J. Abbott, E. Diller, and A. J. Petruska, "Magnetic methods in robotics," *Annual Review of Control, Robotics, and Autonomous Systems*, vol. 3, pp. 57–90, 2020.

[15] J. Bradfield, R. Tung, R. Mandapati, N. G. Boyle, and K. Shivkumar, "Catheter ablation utilizing remote magnetic navigation: a review of applications and outcomes," *Pacing and Clinical Electrophysiology*, vol. 35, no. 8, pp. 1021–1034, 2012.

[16] S. Jeon, A. K. Hoshiar, K. Kim, S. Lee, E. Kim, S. Lee, J.-y. Kim, B. J. Nelson, H.-J. Cha, B.-J. Yi, *et al.*, "A magnetically controlled soft microrobot steering a guidewire in a three-dimensional phantom vascular network," *Soft robotics*, vol. 6, no. 1, pp. 54–68, 2019.

[17] T. Xu, J. Zhang, M. Salehizadeh, O. Onaizah, and E. Diller, "Millimeter-scale flexible robots with programmable three-dimensional magnetization and motions," *Science Robotics*, vol. 4, no. 29, p. eaav4494, 2019.

[18] J. J. Abbott, O. Ergeneman, M. P. Kummer, A. M. Hirt, and B. J. Nelson, "Modeling magnetic torque and force for controlled manipulation of soft-magnetic bodies," *IEEE Transactions on Robotics*, vol. 23, no. 6, pp. 1247–1252, 2007.

[19] J. Seifert, S. Roitsch, and A. M. Schmidt, "Covalent hybrid elastomers based on anisotropic magnetic nanoparticles and elastic polymers," *ACS Applied Polymer Materials*, vol. 3, no. 3, pp. 1324–1337, 2021.

[20] S. Taccola, T. da Veiga, J. H. Chandler, O. Cespedes, P. Valdastri, and R. A. Harris, "Micro-scale aerosol jet printing of superparamagnetic fe3o4 nanoparticle patterns," *Scientific Reports*, vol. 12, no. 1, p. 17931, 2022.

[21] J. Kim, S. E. Chung, S.-E. Choi, H. Lee, J. Kim, and S. Kwon, "Programming magnetic anisotropy in polymeric microactuators," *Nature materials*, vol. 10, no. 10, pp. 747–752, 2011.

[22] S. Salmanipour, O. Youssefi, and E. D. Diller, "Design of multi-degrees-of-freedom microrobots driven by homogeneous quasi-static magnetic fields," *IEEE Transactions on Robotics*, vol. 37, no. 1, pp. 246–256, 2020.

[23] P. Ryan and E. Diller, "Magnetic actuation for full dexterity microrobotic control using rotating permanent magnets," *IEEE Transactions on Robotics*, vol. 33, no. 6, pp. 1398–1409, 2017.

[24] G. Pittiglio, M. Brockdorff, T. da Veiga, J. Davy, J. H. Chandler, and P. Valdastri, "Collaborative magnetic manipulation via two robotically actuated permanent magnets," *IEEE Transactions on Robotics*, 2022.

[25] J. Edelmann, A. J. Petruska, and B. J. Nelson, "Magnetic control of continuum devices," *The International Journal of Robotics Research*, vol. 36, no. 1, pp. 68–85, 2017.

[26] M. Yousefi and H. Nejat Pishkenari, "Independent position control of two identical magnetic microrobots in a plane using rotating permanent magnets," *Journal of Micro-Bio Robotics*, vol. 17, pp. 59–67, 2021.

[27] Q. Boehler, S. Gervasoni, S. L. Charreyron, C. Chautems, and B. J. Nelson, "On the workspace of electromagnetic navigation systems," *IEEE Transactions on Robotics*, 2022.

[28] J. Sikorski, I. Dawson, A. Denasi, E. E. Hekman, and S. Misra, "Introducing bigmag—a novel system for 3d magnetic actuation of flexible surgical manipulators," in *2017 IEEE International Conference on Robotics and Automation (ICRA)*, pp. 3594–3599, IEEE, 2017.

[29] F. Carpi and C. Pappone, "Stereotaxis niobe® magnetic navigation system for endocardial catheter ablation and gastrointestinal capsule endoscopy," *Expert review of medical devices*, vol. 6, no. 5, pp. 487–498, 2009.

[30] L. Barducci, G. Pittiglio, J. C. Norton, K. L. Obstein, and P. Valdastri, "Adaptive dynamic control for magnetically actuated medical robots," *IEEE robotics and automation letters*, vol. 4, no. 4, pp. 3633–3640, 2019.

[31] J. Hwang, S. Jeon, B. Kim, J.-y. Kim, C. Jin, A. Yeon, B.-J. Yi, C.-H. Yoon, H.-J. Park, S. Pané, *et al.*, "An electromagnetically controllable microrobotic in-

terventional system for targeted, real-time cardiovascular intervention," *Advanced Healthcare Materials*, vol. 11, no. 11, p. 2102529, 2022.

[32] S. Pane, G. Faoro, E. Sinibaldi, V. Iacovacci, and A. Menciassi, "Ultrasound acoustic phase analysis enables robotic visual-servoing of magnetic microrobots," *IEEE Transactions on Robotics*, vol. 38, no. 3, pp. 1571–1582, 2022.

[33] S. Pane, M. Zhang, V. Iacovacci, L. Zhang, and A. Menciassi, "Contrast-enhanced ultrasound tracking of helical propellers with acoustic phase analysis and comparison with color doppler," *APL bioengineering*, vol. 6, no. 3, p. 036102, 2022.

[34] X. Liu, D. Esser, B. Wagstaff, A. Zavodni, N. Matsuura, J. Kelly, and E. Diller, "Capsule robot pose and mechanism state detection in ultrasound using attention-based hierarchical deep learning," *Scientific Reports*, vol. 12, no. 1, p. 21130, 2022.

[35] M. E. Tiryaki, S. O. Demir, and M. Sitti, "Deep learning-based 3d magnetic microrobot tracking using 2d mr images," *IEEE Robotics and Automation Letters*, vol. 7, no. 3, pp. 6982–6989, 2022.

[36] C. Fischer, Q. Boehler, and B. J. Nelson, "Using magnetic fields to navigate and simultaneously localize catheters in endoluminal environments," *IEEE Robotics and Automation Letters*, vol. 7, no. 3, pp. 7217–7223, 2022.

[37] M. E. Tiryaki and M. Sitti, "Magnetic resonance imaging-based tracking and navigation of submillimeter-scale wireless magnetic robots," *Advanced Intelligent Systems*, vol. 4, no. 4, p. 2100178, 2022.

[38] A. Z. Taddese, P. R. Slawinski, M. Pirotta, E. De Momi, K. L. Obstein, and P. Valdastri, "Enhanced real-time pose estimation for closed-loop robotic manipulation of magnetically actuated capsule endoscopes," *The International journal of robotics research*, vol. 37, no. 8, pp. 890–911, 2018.

[39] M. Zhang, L. Yang, C. Zhang, Z. Yang, and L. Zhang, "A 5-d large-workspace magnetic localization and actuation system based on an eye-in-hand magnetic sensor

array and mobile coils," *IEEE Transactions on Instrumentation and Measurement*, vol. 72, pp. 1–11, 2023.

[40] C. Watson and T. K. Morimoto, "Permanent magnet-based localization for growing robots in medical applications," *IEEE Robotics and Automation Letters*, vol. 5, no. 2, pp. 2666–2673, 2020.

[41] D. Son, X. Dong, and M. Sitti, "A simultaneous calibration method for magnetic robot localization and actuation systems," *IEEE Transactions on Robotics*, vol. 35, no. 2, pp. 343–352, 2018.

Chapter 2

Review of Medical Continuum Robots

Chapter source: T. da Veiga, J. H. Chandler, P. Lloyd, G. Pittiglio, N. J. Wilkinson, A. K. Hoshiar, R. A. Harris, and P. Valdastri, "Challenges of medical continuum robots in clinical context: a review", Progress in Biomedical Engineering, vol. 2, no. 3, pp. 032003

Abstract

With the maturity of surgical robotic systems based on traditional rigid-link principles, the rate of progress slowed as limits of size and controllable degrees of freedom were reached. Continuum robots came with the potential to deliver a step change in the next generation of medical devices, by providing better access, safer interactions, and making new procedures possible. Over the last few years, several continuum robotic systems have been launched commercially and have been increasingly adopted in hospitals. Despite the clear progress achieved, continuum robots still suffer from design complexity hindering their dexterity and scalability. Recent advances in actuation methods have looked to address this issue, offering alternatives to commonly employed approaches. Additionally, continuum structures introduce significant complexity in modelling, sensing, control and fabrication; topics which are of particular focus in the robotics community. It is, therefore, the aim of the presented work to highlight the pertinent areas of active research, and to

discuss the challenges to be addressed before the potential of continuum robots as medical devices may be fully realised.

2.1 Introduction

In the last two centuries, healthcare procedures have changed dramatically. This has been possible due to technological breakthroughs that have enabled the development of new medical devices and techniques [1]. One of the most successful examples is the endoscope. This device allowed surgeons, for the first time in the ^{19} century, to look into their patients' bodies through natural orifices and wounds as opposed to making fresh incisions [2; 3]. This has impacted screening and intervention, which has also shifted towards less invasive methods and given rise to minimally invasive surgeries (MIS) such as laparoscopy or natural orifice trans-luminal endoscopic surgery (NOTES) [4]. These present several benefits to the patient when it comes to blood loss, recovery time, post-operative trauma, scarring and wound site infection [5]. However, they can be challenging from the surgeons' point of view due to differences in ergonomic control, sensory feedback, dexterity and intuitiveness [6; 7; 8].

These limitations and the need for better and improved medical procedures have paved the way to robotically-assisted medical interventions. This has in turn allowed clinicians to perform procedures with more precision, flexibility, and control while decreasing procedural times and complications to the patient [9]. Medical robots have come a long way since their inception in the 80s when a standard industrial robot was used to secure a fixture in place for neurosurgery [10]. The release of the da Vinci Surgical System (Intuitive Surgical, Inc., Sunnyvale, CA, USA) in the early 2000's further heightened the interest in this field. In 2018 more than 1 million procedures worldwide were carried out with the da Vinci system alone [11].

The majority of medical robotic systems in use today rely on rigid instruments with dexterous wrists at the tip. This restricts their movements due to the low number of degrees of freedom (DOF) exhibited [12; 13], hindering the robot's adaptability and safe patient

interaction [14]. More recently, continuum robots (CRs) have emerged and are gaining major interest as an alternative to standard rigid-link robots. CRs are able to generate smooth curvilinear motions exhibiting infinite DOFs and, as such, have the potential to reach further into the body with reduced tissue trauma through MIS and NOTES (Figure 2.1) [13]. The use of CRs in medical robotic platforms consequently allows for improvements in existing procedures and the development of new and better techniques. This has recently been illustrated by the launch of several continuum platforms such as Monarch™ (Auris Health, Inc., Redwood City, CA, USA) and Ion (Intuitive Surgical, Inc., Sunnyvale, CA, USA).

Despite previous reviews on the topic of medical CRs [15; 16; 17; 18], the abundance of attention and development on the topic warrants an updated review. Therefore, in this article we provide an overview of the current challenges that this class of robots face which currently inhibit the realisation of their full potential. We begin the review by presenting the main application areas for medical continuum robots given the current state of the art. We then provide an introduction to the field of CRs followed by an overview of the current actuation methods. We then describe the challenges that these robots face according to their fabrication, modelling, control and sensing; and conclude by providing a comparison between methods and recommendation for future research.

2.2 Applications of medical continuum robots

2.2.1 Brain interventions

Open brain surgery is still a common procedure, especially in emergency situations, however MIS has been gaining popularity such as in electrode implantation and endovascular coiling for intracranial aneurysm [19; 20; 21]. Since 2010, the robotic system ROSA® Brain (MEDTECH, Inc., Montpelier, France) has been used to perform a variety of these procedures. Lower procedural times and higher accuracy and precision are among its

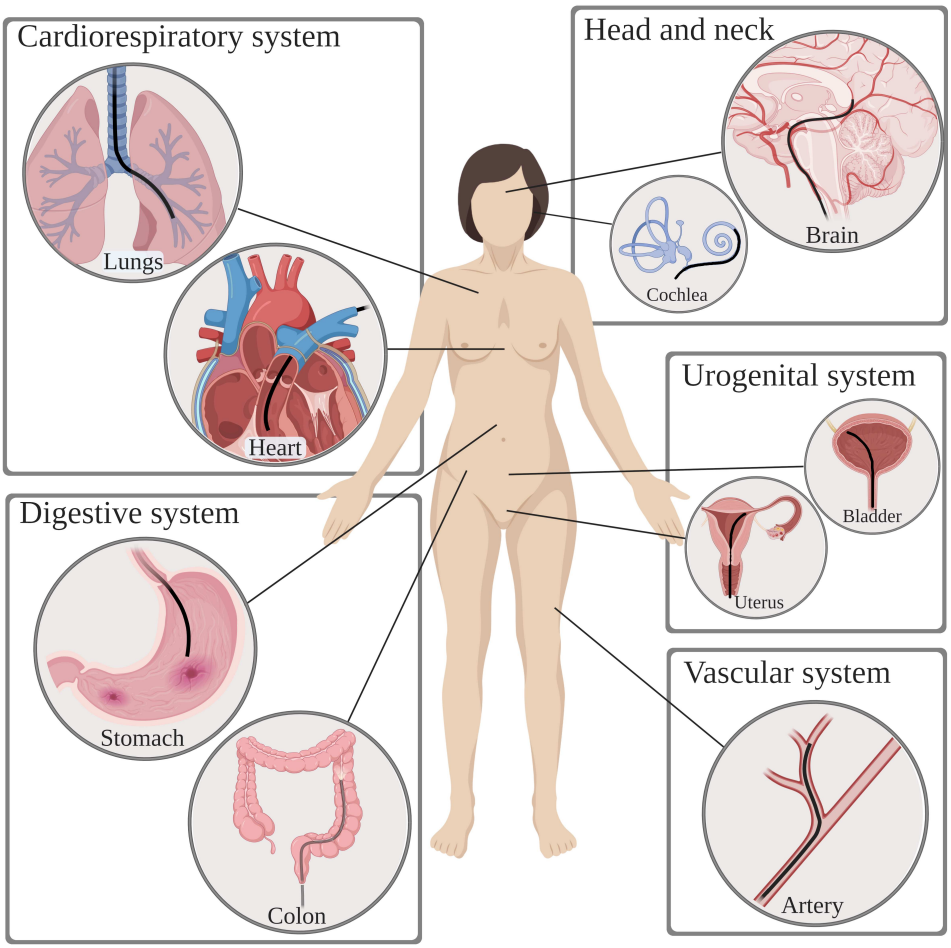

Figure 2.1: Applications of medical continuum robots to access hard-to-reach areas in a minimally invasive manner. These include the cardiorespiratory system, the digestive system, head and neck, the urogenital system and the vascular system.

benefits, proving the effectiveness of robot-assisted brain interventions over conventional methods [22].

Most brain procedures (manual or robotic) still employ rigid, straight instruments, limiting the possible paths between the entry point and the target [19]. The use of continuum robotic systems that are able to conform to curvilinear paths will enhance brain MIS; delivering wider freedom to suitable procedures. To this end, some flexible devices, such as magnetic needles [23], have been emerging but remain too stiff to provide increased path freedom.

2.2.2 Lung interventions

Effective trans-oral bronchoscopy for lung biopsy is a key element in early diagnosis of lung cancer [24; 25]. However, traditional bronchoscopes are restricted to movements only along the lung's bronchial tree limiting procedural efficacy [26]. Continuum robotic systems for a deeper, more consistent and stable bronchoscopy have long been an area of interest. The commercial release of the Monarch™ (Auris Health, Inc., Redwood City, CA, USA) and Ion (Intuitive Surgical, Inc., Sunnyvale, CA, USA) platforms, in 2018 and 2019 respectively, are great examples of systems targeting this need. By using ultra-thin bronchoscopes and catheters, these robotic devices are able to reach further into the lung when compared to conventional bronchoscopes [27; 28; 29]. The use of CRs for lung biopsy has resulted in improved control, dexterity and freedom of movement through the airways.

Beyond diagnosis, robotics for treatment of pathologies of the respiratory system has also been emerging; including standard medical robotic platforms alongside newer continuum systems, such as the cable-driven Flex® Robotic System (Medrobotics, Raynham, MA, USA) [30; 31]. However, due to their lack of dexterity and increased size, these systems have thus so far been limited to head and neck interventions [32]. As such, there have been considerable efforts to allow robotic surgery deeper into the trachea and bronchial tree. Indeed, the Virtuoso Surgical (Virtuoso Surgical Inc., Nashville, TN, USA) system recently demonstrated treatment of a central airway obstruction [33] and is an example of progress in this direction

2.2.3 Endovascular interventions

Continuum structures have long been manually inserted into blood vessels and manipulated to the desired location to treat endovascular and heart conditions in a minimally invasive manner [15]. As can be expected, precise manual catheter navigation and place-

ment is challenging, requiring the surgeon to undergo extensive training. Aligning these existing devices and procedures with robotic navigation and steering is a potential solution to overcome this limitation.

Over the last decade, several robotic navigation and steering systems for guide-wires, stents and catheters have been released, such as Magellan and Sensei (Hansen Medical, Mountain View, CA, USA), and CorPath GRX (Corindus, Inc., Waltham, MA, USA). These systems have been used in a variety of procedures from peripheral vascular to neurovascular interventions [34; 35; 36; 37; 38; 39; 40]. Robotic navigation of magnetic catheters has also seen significant progress with systems such as the Stereoaxis Niobe® Robotic Magnetic Navigation System (Stereotaxis, Inc., St. Louis, MO, USA) [41]. These navigation systems, in addition to enabling higher accuracy and precision, are also capable of reducing exposure to radiation and contrast agent for patients and clinicians by being remotely controlled and cutting procedural times [42]. Building on robotic control, autonomous catheter navigation is also now being investigated, however this is still at an early development stage [43].

2.2.4 Gastroenterological interventions

Currently early screening of cancers of the gastrointestinal (GI) tract is performed via traditional endoscopy or wireless capsule endoscopy (WCE) and, despite their achievements, both methods have their limitations [24; 44; 45; 46; 47]. Endoscopes are known to cause tissue damage and discomfort for the patient, whereas WCE lacks active locomotion, tissue interaction and lumen diameter adaptation [48; 49; 47; 46].

To this extent, robotic alternatives to these two methods have been reported. Robotically actuated endoscopes are able to improve comfort and reduce pain for the patient by providing an alternative to manual handling and navigation [50; 31; 51]. Robotic alternatives to WCE have mainly focused on achieving active locomotion [52; 53], but ultimately, the capsules' wireless characteristic limits their application to screening only. Additionally,

robot assisted GI surgery is common across several procedures, such as removal of liver tumours or the gallbladder, using systems such as the da Vinci [54; 55; 56; 57]. Due to the lack of dexterity exhibited by the instruments, open surgery is still the preferred method in some cases. Emerging treatment procedures using continuum micro-robots have been reported, such as the deployment of patches for stomach ulcers [58] or targeted drug delivery [59; 60]. These technologies, however, are still at a very initial development stage.

2.2.5 Urogenital interventions

Robotic interventions in the urogenital system have long been common for specific procedures such as prostatectomy or nephroureterectomy [61; 62]. However, single-port systems deployable through natural orifices are required to further reduce invasiveness and to treat alternate pathologies. To this extent, a lot of attention has been given to research on continuum robots for urogenital interventions.

Continuum robots to replace rigid resectoscopes used in bladder cancer diagnosis [63; 64], hand-held manipulators for laser prostate surgery [65], or even flexible fetoscopic instruments addressing twin-to-twin transfusion syndrome [66; 67] are some of the proposed devices in the area. However, currently there are no commercial platforms available. Given the presence of a natural orifice, such as vagina and urethra, the use of continuum robots in this area may deliver several benefits.

2.3 The Rise of Continuum Manipulators

2.3.1 Past and present of continuum robots

Traditional robots are composed of discrete rigid links connected by joints and are able to move with high precision and accuracy, making them highly suitable for tightly controlled and repeatable tasks. However, there are often limitations when operating in small and

confined spaces where adaptability, dexterity and safe interactions with the patient are necessary [17; 13]. As previously mentioned, the recent coupling of manually steered continuum structures with robotic actuation and control has provided more intuitive and easier to use systems increasing the benefits to both the surgeon and the patient.

Continuum robotic systems can be the innovation needed across several areas of medicine, where current healthcare practices have limited efficacy due to access and safety. Furthermore, replacing straight rigid devices with continuously deformable structures may allow better navigation inside the body through conformation to the patient's anatomy and provide safer physical interaction. Steering and navigating such devices, however, poses significant challenges.

2.3.2 Definition and classification of continuum robots

CRs can be defined as actuated structures that form curves with continuous tangent vectors [17]. These robots are considered to have an infinite number of joints and DOF, allowing them to change their shape at any point along their length [14]. These characteristics make them ideal for variable environments where flexibility and adaptability to external conditions are necessary.

Continuum manipulators (CMs), structures that resemble an elephant's trunk or an octopus' tentacle, have been gaining popularity for medical applications. These typically have a small diameter and exhibit high dexterity in order to reach confined spaces, such as the lung's bronchi. The design of such structures is, on its own, a challenge given that higher dexterity normally comes associated with a higher number of actuators. This increases the diameter of the structure, which in turn decreases the range of motion [17].

The demand for safer tissue interactions has led to the development of soft robots. This emerging field comprises robots made of intrinsically soft elastomeric materials, giving the robot the ability to absorb energy and deform to their surroundings and external constraints [68]. They are, therefore, highly compliant and flexible, enabling a vast range of complex motions [69]. Soft robots are by definition CRs as they can deform

continuously having infinite DOF [70; 71]. Additionally, they exhibit deformation whereas hard CRs only exhibit flexibility. Medical soft robotics have shown possibilities from targeted drug delivery to minimally invasive procedures [59; 72].

2.4 Actuation of Continuum Manipulators

2.4.1 Mechanical Actuation

Mechanical actuation refers to the use of solid elements to directly transmit forces and torques through or within the actuator structure. Driven in part by the requirement of high dexterity at small scales for medical interventions, mechanically driven continuum robots have successfully branched from classical serial designs. Given the variety of approaches taken, an abundance of robot designs have emerged, being broadly categorised into steerable needles, concentric tubes and backbone-based [17; 73; 74]. Generally, the order presented here reflects an increase in design complexity and force output, although specific implementations vary. Figure 2.2 illustrates example implementations utilising these design principles, and Table 2.1 summarises many of the mechanically actuated designs proposed in the literature for specific medical interventions.

(a) (b) (c) (d)

Figure 2.2: Mechanically actuated continuum robot designs for varied actuation principles; showing: (a) the steerable needle concept [75], (b) a typical concentric tube design [76], and backbone-based designs (c) tendon driven [77] and (d) multi-backbone [78].

2.4.1.1 Steerable needle designs

Steerable needles form their continuum shape exclusively through interaction with the

Table 2.1: Summary of mechanically actuated medical robots.

Ref	**Design principle**	**Application**	**Actuation**	**Diameter (mm)**	**Controllable DOF**	**Length (mm)**	**Min. bending radius (mm)**
[78]	Bevel tipped steerable needle	MIS		0.7	3	-	-
[79; 80]	Notched steerable needle	Brachytherapy	Ultrasound guided	3.2	3	-	171
[81; 82]	Concentric tube	MRI guided surgery	3 piezoelectrically actuated tubes	-	6	567	72
[33]	Concentric tube	Central airway obstruction	2 motor driven dexterous arms	<2	3 each	-	-
[83]	Monarch™: Concentric tube	Bronchoscopy	Cable driven	4.2	10	-	-
[84]	Backbone	Neuroendoscope	2 tendon driven bending sections	3.4	1 each	120	-
[85]	Backbone	Single-site partial nephrectomy	2 tendon driven segments	26	2 each	240	76
[86]	Backbone	Laparoscopy	Cable driven with compressible spring backbone	8	-	-	-
[87]	Backbone	Neurosurgery	Tendon driven extensible backbone segments with tendon driven bending	21	-	340	-
[88; 89]	Backbone	Cardiac surgery	50 tendon driven serial links	10	105 in total	300	35
[90]	Backbone	Throat MIS	2 multi-backbone segments with push-pull actuation	4.2	20	35	8.13

tissues. Development of robotically controlled needle insertion methods has been driven by the aim of accurately and precisely reaching target locations within tissues through non-linear pathways in order to avoid obstacles or delicate structures. Initial designs typically relied on the uneven forces produced at the bevel tip of the needle to steer along curved trajectories [75]. Rotation of the needle with variable duty cycle enabled path control [76; 77].

Over the years, a number of developments have been proposed in an attempt to minimise tissue damage during insertion and reduce the radius of curvature. Needles with kinked bevel tips [91], or with a concentric sleeve and needle stylet [92] have been reported. Furthermore, needles with flexures [93] and notches [79; 80] to reduce tip stiffness have also been proposed. Different steering methods have also been developed using tendons [94; 95], through magnetic actuation [23; 19], and by using water jets [96]. Steering has also been achieved utilising interlocking translating sections inspired by the wasp [97; 98], and an over tube [99]. Despite their achievements, this type of continuum robots ultimately relies on tissue damage for actuation.

2.4.1.2 Concentric tube designs

As their name implies concentric tube actuators result from the nesting of pre-curved tubes, typically made from nitinol (NiTi), within one another [100; 101; 102]. With relative rotation and translation, varied sets of curvature are achievable with a further increase in workspace possible through coupled motions. Although first presented for generic needle-steering, and surgical applications [100; 101], specific formulations have since been presented for: neurosurgery [103] including endonasal [104; 105]; transurethral prostate surgery [106; 81]; lung access [107] for biopsy [108] and central airway obstruction removal [33]; and needle driving through elastic instability [109].

These applications highlight the immediate benefit of concentric designs as their ability to be realised at small scales, allowing access through the narrow tortuous pathways of the body. However, unlike steerable needles, concentric tubes rely on a change in

length to induce varying curvature. Additionally, limitations in pre-curvature of tubes limit their path-following capabilities and require design parameter optimization to match application specific trajectories [110]. Furthermore, the payload that can be supported through concentric tube implementations is an important limitation of their interventional capacity.

2.4.1.3 Backbone-based designs

A widely adopted approach for realising continuum actuator design is the use of an elastic central backbone. This 'spine' supports the elements required for actuation while its elastic properties produce continuous bending and restoration forces; returning the actuator to a neutral (ordinarily straight) position upon the removal of actuation forces. A number of materials have been employed for this function, such as springs [111; 84; 112], polymers [113; 114; 115], and NiTi rods/tubes [90; 116].

With a central elastic structure in place, tendons or rods are routed along the length of the backbone, held to the desired routing pathway through the use of spacing discs, and fixed to a specific distal point. Although similar in form tendon driven embodiments produce actuation force only under cable tension, while rod driven (multi backbone) is rigid in tension and compression, resulting in a stiffer overall design. Upon loading, the tendons/rods transmit forces to the termination point resulting in bending-inducing torques. Increased DOF can be achieved by serially stacking actuation segments of this design.

Routing of the actuation element is a key variable in determining the manipulator's performance. Usually, routing configurations per segment are comprised of one or two antagonistic pairs for single or bi-planar bending respectively, or three actuating elements spaced evenly around the central axis of the actuator. A generalised model for tendon routing for single-segment designs [117] and two-segment designs [118] has been proposed. These show that helical tendon routing increases workspace and enhances obstacle avoidance. Radial variation in tendon path routing has also been recently explored [119],

illustrating the ability to significantly increase tip stiffness with non-parallel tendons. Although tuning of this nature enables varied actuator design, once implemented the kinematic and dynamic properties are largely invariant. However, features to allow variation in design during operation have also been investigated. Magnetic spacing discs have been used to form extensible segments [116], leading to the possibility of follow-the-leader and path following motions [120; 110]. Alternative designs for achieving extension/contraction include a tendon driven concentric backbone [87] and the use of two interlaced lockable continuum robots [121]. In addition to variable kinematics, designs have also been presented to allow stiffness adjustment through antagonistic tendon-fluid bladder configurations [122; 123; 124], pressure/vacuum jamming techniques[125; 126; 127; 85], using shape memory alloys [112], or insertable constraints[128].

The benefits of backbone designs reside in their large range of motion, and configurability. With the addition of multi-segment, variable length designs and tuneable stiffness, they are highly suited to surgical applications. However, scaling down these designs is challenging, in part due to high levels of hysteresis introduced from internal friction and tension loss within actuation cables, which ultimately limits their scope.

2.4.2 Fluidic Actuation

Fluidic actuators operate under the principle that a confined fluid applies any pressure change evenly throughout its volume. Any anisotropic strain limiter included in either the material properties or the material topography will produce correspondingly anisotropic deformation [129]. The fluid employed in these actuators highly influences their performance. In medical applications, the fluids more commonly employed are water and air, hydraulic or pneumatic respectively, given their availability, regulation and disposal, and safety to the patient [130]. Pneumatic systems are preferred due to the low viscosity of air which is crucial for miniaturisation. Its compressibility, however, can reduce the system's controllability and introduce lag [131]. Fluidic actuators are able to achieve bending, twisting, extending and contracting through different designs, such as artificial muscles and fluidic elastomer actuators. In Table 2.2, a summary of medical robots utilising

fluidic actuation is presented.

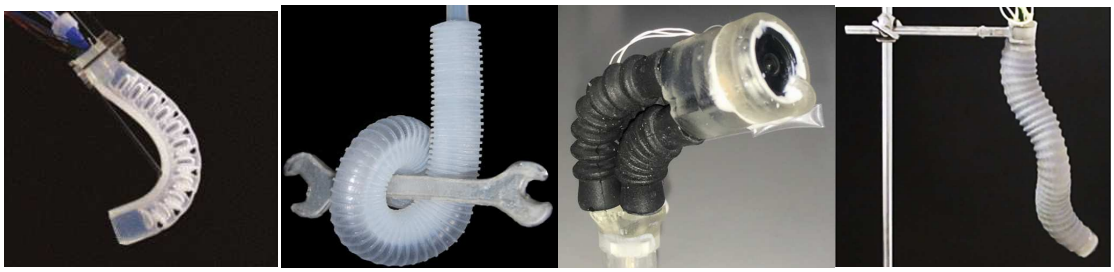

(a) (b) (c) (d)

Figure 2.3: Pneumatically actuated continuum robots; (a) pleated [132] and (b) corrugated [133] FEA manipulators, (c) The "Belloscope" tip driven endoscope [134] and (d) the STIFF-FLOP multi-modal system [135].

2.4.2.1 Artificial Muscles

Artificial muscles are characterised by an axial contraction when pressurised [132; 133]. The McKibben muscle is considered to be the original fluidic actuator and consists of an inner tube enclosed in a flexible double-helix braided sheath responsible for contraction [132]. This actuator is known for providing a high power to weight ratio.

With advances in manufacturing capabilities over the past 25 years, other variants of artificial muscles have emerged, such as Pneumatic Artificial Muscles (PAM) [132]. These employ the same principle as the McKibben muscles but by varying wrap angles and densities of the external sheath, the topology of deformation under pressure can be manipulated [134; 135]. PAMs are able to achieve lighter per unit force than other alternatives, greater compliance and zero static friction, preventing jumps during actuation [132]. These characteristics are of particular interest to the surgical robotics community from a safety perspective, and their use has been reported in cardiac compression devices [133].

2.4.2.2 Fluidic Elastomer Actuator

Fluidic Elastomer Actuators (FEA) consist of synthetic elastomer films with embedded

Table 2.2: Summary of fluidic actuated medical robots.

Ref	**Design principle**	**Application**	**Actuation**	**Diameter (mm)**	**Controllable DOF**	**Length (mm)**	**Maximum bending angle (deg)**	**Maximum pressure (kPa)**	**Max. force (N)**
[133]	PAM	Direct cardiac compression	Pneumatic	<14	-	140	-	100	50
[66]	McKibben artificial muscles	Fetal surgery	Pneumatic	-	2	-	-	-	-
[137]	FEA	MIS	3 pneumatic modules	25	1	165	240	72	-
[31]	FEA	Colonoscopy	Hydraulic	18	5	60	130	6.1	7.9
[138; 139; 140; 141]	FEA	Gastroscopy	Hydraulic waterjet	12	3	-	94	32.8	0.10
[142]	FEA	MIS	2 pneumatic modules	32	-	135	132	65	7.9
[143; 144]	Parallel bellows	Gastroscopy	3 pneumatic bellows at the tip	<14	3	120	65	-	-
[145; 146]	Serial bellows	Endovascular	2 hydraulic segments	3	-	80	-	-	-

channels which expand and/or bend when pressurised[68; 136]. It is a wholly soft structure and its strain limiter is built into the material's geometry. This total absence of rigid material enables a robot with a much greater range of movement and which is, in general, safer in contact with human tissue. FEAs also operate at lower pressures than artificial muscles due to their lack of fibrous support [131]. This enables easier actuation but limits the maximum force the robot can exert.

FEAs come in a range of different topologies offering different solutions to various problems such as cylindrical tubes [137], eccentric tubes [147], pneumatic networks [130; 148], corrugated membranes (ribbed [131] or pleated [149], see Figure 2.3(a) and 2.3(b)) and helically restricted elastomers [150]. All these options offer variants of anisotropic strain limited geometry, generating highly non-linear deformations which, when incorporated with the natural compliance of the material, produce shapes completely unachievable in traditional hard robots or with artificial muscles. This highly non-linear behaviour is, however, difficult to model and control. Furthermore, large deformations can be viewed as problematic when navigating confined spaces such as those within the human body. There is also a risk of rupture due to their unconstrained pneumatic bladders. When operating in sensitive environments and near sharp objects, such as surgical blades, this is rightly considered a real risk.

2.4.2.3 Emerging Actuators

Recently a number of innovative alternative actuators have been developed. One example is actuation via micro-jet propulsion [151]. Despite the potential demonstrated by this method, further safety developments should be addressed such as disposal of actuation fluid in a comfortable manner and ensuring the minimisation of tissue damage by the propulsive jet. Other interesting examples include a robot which is steerable and controllable by growth [152]; and peristaltic motion [153].

In addition to emerging fluidic actuation methods, a large effort has been made to develop safer alternatives from a rupture point of view. One such example is the fibre-reinforced

FEA [154] which dopes the elastomer with microfibres turning any potential rupture into a slow puncture. Approaching the same issue from the opposing perspective, series PAM (sPAM) replace the original fibrous sheath with additional pneumatic actuators creating a fully soft actuator with similar power delivery capabilities to the original PAM [155]. Furthermore, self-sealing polymers [149] and vacuum actuated elastomers [156; 157] have also been reported.

2.4.2.4 Actuator Arrangements

Typically one actuator will provide one primitive motion [158]. Continuum robots, especially for medical applications, must be capable of multi-directional deformations [159]. This is most readily achieved via modular actuation [137].

In modular actuation, several actuators are connected with the ramification that each independent actuator must have its own supply line [137]. Actuators may be connected in series to create slender continuum manipulators [135], in a parallel and un-conjoined arrangement to create, for example, grippers [160], or in a parallel and conjoined arrangement for multi-directional manipulators [161]. A common approach is to connect actuators both in parallel and in series as in the STIFF-FLOP project [137] shown in Figure 2.3(d). This robot features ten independently operated actuators each with a 1.5 mm diameter driveline. The robot itself has a diameter of 25 mm illustrating one of the major limiting factors for the application of fluidic actuators to continuum robots' miniaturisation. Obviously, future improvements in manufacturing technology can assist but the trade-off between manipulability and size is a chronic and yet unresolved issue. Some alternatives to address this issue have been reported, such as the use of Band Pass Valves to reduce the number of drivelines [145] but the traditional limitations of miniaturisation still apply with regards to manufacturing technology.

2.4.3 Magnetic Actuation

Magnetic actuation of robots relies on the use of magnetic forces and torques; generated through manipulation of the magnetisation of the robot and the external magnetic field in which the robot is placed. This type of actuation eliminates the need for bulky on-board systems allowing easy miniaturisation and untethered control, both useful for the medical robot applications. Furthermore, magnetic fields are proven safe for clinical applications, having been in use for several decades [162].

Robot designs with time-varying magnetic properties placed under constant fields are challenging to fabricate and present safety concerns due to heat dissipation [163; 164]. For these reasons, magnetic robots for medical applications almost exclusively have constant magnetic properties and are placed inside a varying magnetic field for manipulation [163]. Over the past two decades, advances in the use of magnetism in robotics have led to different ways of incorporating magnetic properties, and to the development of novel actuation and navigation systems. Table 3 lists several of the magnetically actuated continuum robots presented in the literature.

2.4.3.1 Device's magnetism

Embedding magnetic properties in continuum robots has been easily done by inserting permanent magnets in their structures. By optimising the location, number and distance between the magnets, the robot can achieve the desired application [165]. This approach is fairly common with a variety of designs and applications reported, such as the guidewire for cardiovascular applications shown in Figure 2.4a [166; 167; 168]. The major advantage of using permanent magnets is that their properties are well known, facilitating the modelling and control of the device. Additionally, the use of components already designed for, and used within, clinical settings facilitates the pathway to commercial adoption. In fact, several magnetically steered catheters are already available on the market, such as Polaris X™ Catheter [16; 169]. However, the use of permanent magnets

imposes limitations in terms of size and achieving fully soft structures.

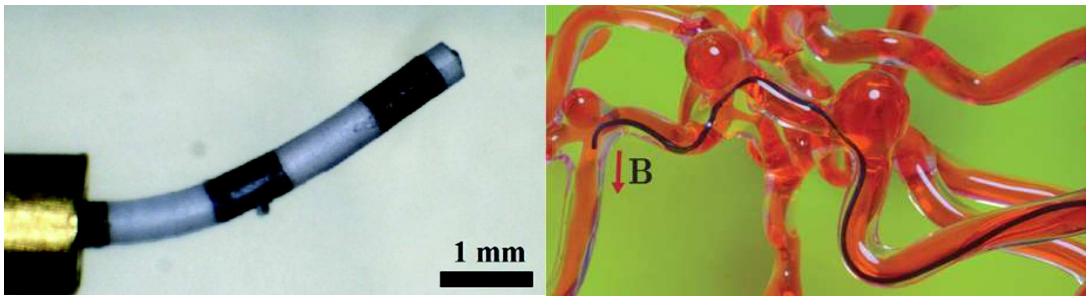

(a) (b)

Figure 2.4: Magnetically actuated continuum robots; (a) embedded permanent magnets (reproduced from [169] originally published under CC BY license); (b) magnetic composite polymers [172].

Alternatively, one can use magnetic composite polymers. These polymers are characterised by the introduction of magnetic micro or nano particles into a polymer matrix [170]. This results in a magnetisable mixture whose characteristics, such as mechanical properties and suitable manufacturing methods resemble the original ones [170]. By inducing a patterned magnetisation profile into structures made out of these polymers, one can achieve fast transformations into complex 3D shapes and locomotion capabilities [171]. An example of continuum robots that employ such composites can be seen in Figure 2.4b. Further information about the challenges of fabrication and inducing magnetisation patterns can be found in Section 2.5.1.

2.4.3.2 Actuation Systems

Unlike the previous actuation methods where the limitations were mainly due to the onboard design, magnetic actuation is limited by the external conditions one can generate, in this case, magnetic fields and magnetic field gradients [172; 173; 174]. Over the past two decades, a number of actuation systems for magnetic robots have been developed and can be fundamentally classified into either coil-based or permanent magnet-based, depending on the source of the magnetic field.

Table 2.3: Summary of magnetically actuated medical robots. Deflection is shown in mm (minimum bending radius) for hard devices, and in degrees (deformation angle) for soft devices.

Ref	**Design principle**	**Application**	**Actuation**	**Diameter (mm)**	**Length (mm)**	**Deflection**	**Inovation**
[166; 168]	Permanent magnet	Heart ablation	Magnetic tip for steering	<2.5	50	7mm	Variable stiffness segments allowing shape forming
[23; 19]	Permanent magnet	Neurosurgery	Magnetic tip for steering	1.3	-	100mm	Magnetically guided steerable needle
[50; 49]	Permanent magnet	Colonoscopy	Magnetic tip for steering	20	22 (active tip)	-	Robotic alternative to manual endoscopes
[167]	Permanent magnet	Endovascular	Two magnets along along the body	0.5	3.8	132.7°	High deformation angles
[186]	Permanent magnet	MIS	Magnetic tip for steering	3	47.5	54°	Titanium robot with flexures along the body
[169]	Polaris X™ Permanent magnet	Electrophysiology	Tendon drive with magnets for steering	2	1500	-	Commercially available soft magnetic catheter
[187]	Magnetic particles	Cerebrovascular	NdFeB in PDMS tip	0.6	3 (active tip)	<90°	Fully sub millimeter magnetic robot
[188]	Magnetic particles	Cerebrovascular	Three NdFeB sections along the body	2	42	-	Fully soft shape forming robot

2.4.3.2.1 Coil-based systems

Coil-based systems are able to generate both homogenous and inhomogeneous magnetic fields by controlling the input electric current. Uniform magnetic fields can be generated by Helmholtz coils [175; 176]. These rely solely on magnetic torques for actuation, given the lack of a magnetic gradient. Maxwell coils, alternatively, achieve both force and torque actuation. Due to their design simplicity, these systems achieve low controllable DOF [177; 178; 179]. Several systems with a high number of electromagnetic coils have been proposed achieving higher number of controllable DOF [180], such as Minimag [181] and OctoMag illustrated in Figure 2.5a [182]. A system capable of fulfilling the theoretical maximum of eight DOF was also recently reported [183]. More recently, emerging systems consisting of moving electromagnetic coils [184] and a magnetic-acoustic hybrid actuation have been reported [185].

Generally, coil-based systems have high controllability and stability [189]. However, they are associated with bulky equipment, small workspace, up-scaling limitations and prohibitively high cost. In fact, adapting these systems to a clinical setting might be a difficult task without loss of the DOF achieved in the research environment.

2.4.3.2.2 Permanent magnet-based systems

Permanent magnet-based systems provide a feasible alternative to electromagnetic coils. These do not rely on real time electrical currents to generate a magnetic field, allowing for stronger fields and field gradients while not suffering from overheating problems [190; 50]. Two approaches using permanent magnets have been reported, rotating permanent magnets, and robotic manipulation of permanent magnets. Rotating permanent magnets, while providing the advantages of permanent magnets, still suffer from reduced workspace [191; 190]. Alternatively, mounting permanent magnets at the end effectors of robotic manipulators and moving them around the desired workspace can be easily translated into the clinical environment given its much larger workspace [192; 193]. This method has been used for a variety of continuum devices, such as that depicted in Figure 2.5b [194; 50].

Despite the advantages of permanent magnets over electromagnetic coils, these systems come with their own limitations. Any changes to the generated fields are performed via mechanical methods, introducing mechanical noise in the system. Furthermore, the non-linear relationship between the magnetic field and induced wrench makes robotic control less straightforward.

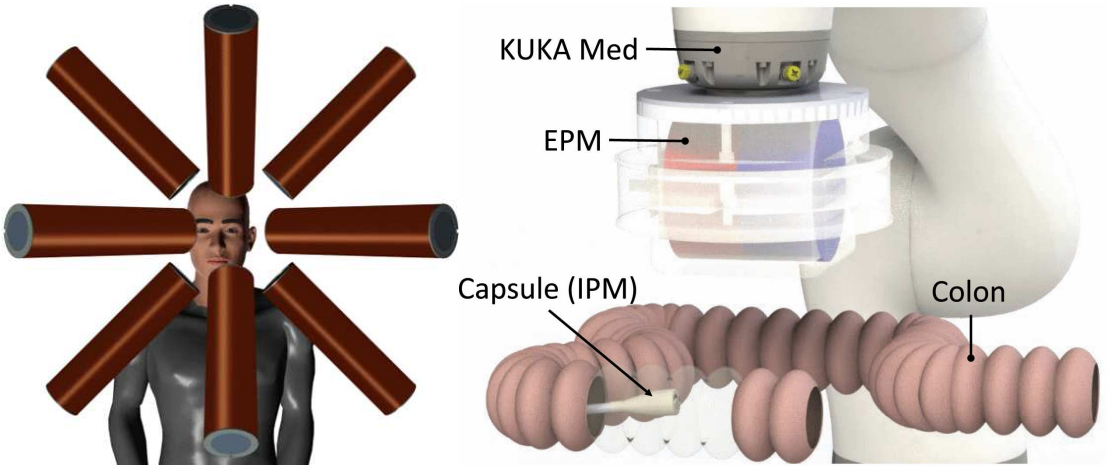

(a) (b)

Figure 2.5: Magnetic actuation systems; (a) Coil-based system Octomag [185] and (b) permanent magnet-based system [50].

2.4.3.3 Magnetic navigation systems

Successful magnetic steering depends not only on reliable magnetic actuation but also on simultaneous monitoring. Magnetic navigation systems based on imaging techniques and electromagnetic tracking have emerged to address this issue.

2.4.3.3.1 Imaging

The high quality and real-time nature of X-ray monitoring systems made them the favoured technique for magnetic navigation. Both coil-based and permanent magnet-based systems using X-ray have been reported [41; 195; 168; 165]. Despite the good results achieved, the risks associated with X-ray exposure are a major limiting factor and have encouraged further development of monitoring systems.

Modified Magnetic Resonance Imaging (MRI) machines have emerged as a candidate

navigation system [196; 196; 197; 198; 199]. In fact, MRI fringe fields have been used for steering continuum magnetic robots [200]. However, the lack of simultaneous monitoring and feedback and the need for more reliable control hinder these systems' use. Ultrasound based monitoring provides a safe, cheap and reliable alternative approach. Their usage in magnetic navigation has been explored [59] and used to provide closed loop navigation in endoscopy [201].

2.4.3.3.2 Electromagnetic Tracking

Navigation of other actuation methods can be done with the aid of common electromagnetic tracking systems, such as Aurora (Northern Digital Inc., Waterloo, Canada). However, these are incompatible with magnetic actuation due to distortions caused by both the external actuation field and the device's magnetism [202; 49]. This being so, alternative methods have been proposed such as the the incorporation of magnetic field sensors and inertial sensors in the robot to determine its pose [49]. An alternative approach sees the placement of a two-dimensional array of magnetic field sensors in the workspace, facilitating miniaturisation of the device [202].

Despite the promising results shown by tracking approaches these are limited to permanent magnet-based actuation systems. Tracking within magnetic fields generated by coil based systems is not possible due to the high number of singularities present.

2.4.4 Summary

Mechanical, fluidic and magnetic actuation methods for continuum robots have given rise to a variety of designs. Overall they are well suited for the medical community despite each having its own limitations.

Mechanical and fluidic methods, although abundant, suffer from trade-offs in terms of size, stiffness and controllable DOF. Many designs presented achieve high levels of dexterity, however, to realise the higher number of DOF, larger diameters are typically necessary. Considering mechanical actuation specifically, the relative rigidity and non-compliance can pose a significant safety risk during tissue interaction, necessitating miti-

gation through complex control strategies. In fact, steerable needles cannot achieve their small bending radii without causing some tissue damage.

Conversely, fluidic robots inherently address this issue given their structural softness and compliance. However, the risk of rupture in these devices during pressurisation still needs to be addressed in an effective and safe way. Furthermore, the relatively low forces they exert opposes progression against device-tissue friction in tortuous anatomy. Solutions that are able to achieve higher forces at lower operating pressures, and with improved patient-specific design may offer safer and more effective options.

Magnetic CRs share many of the inherent benefits with mechanical and fluidic devices, with the addition of being able to achieve much smaller diameters due to the dearth of internal design required, such as cable routes or fluidic channels. Furthermore, the controllable DOF are dependent on the external actuation system, which permits miniaturisation of the device without loss of controllability. This becomes extremely useful when considering endovascular or brain procedures where thin devices are needed. One major drawback when using magnetic composite polymers is biocompatibility. Although solutions are well established for fluidic devices [161], for magnetic CRs the issue persists. Solutions such as coating the devices with biocompatible materials have been reported [187], but further studies in this area are still needed.

A final but crucial consideration for these approaches is the off-board actuation system used. This has been thoroughly explored in the literature for mechanical and fluidic devices, as they rely primarily on well-established and effective robotic methodologies such as cable transmission and pneumatic pumps. Magnetic devices, however, represent a much more recent technology and exhibit less straightforward control strategies. This has hindered a quick and easy implementation of concepts. As such a wide diversity of magnetic actuation strategies have emerged dependent on the requirements of the specific application, however, significant exploration on this topic is still required.

2.5 Challenges associated with Continuum Manipulators

2.5.1 Fabrication

Medical continuum robotics is an emerging field with some examples of devices now breaking into the market. As the technology further matures, the development of effective manufacturing processes that enable greater function and decreased size scales will be essential to growth of the field. This has been shown in soft robots, where innovation in manufacturing processes has illustrated new modalities of actuators, design freedom, sensing and operation.

Fabrication of mechanically actuated robots is well established as they are commonly produced by standard subtractive manufacturing techniques (e.g. milling or electrical discharge machining). However, the use of alternative methods, such as 3D printing, to allow for patient- or procedure- specific customisation has been reported [203], as well as methods to facilitate fabrication of concentric tubes [204]. Given that fabrication for fluidic and magnetic robots is a considerably newer area of research and less explored in the literature, in this paper we first focus on fabrication of polymeric, flexible structures normally employed in soft robotic devices. The focus then shifts to magnetic continuum structures where new fabrication strategies and magnetisation techniques present significant opportunities for increased function within robotic surgical devices.

2.5.1.1 Soft Lithography

Soft lithography is a common technique for producing continuum structures due to its low barrier to entry. The process relies on the accurate replication of features from a master by casting a liquid polymer. Once cured, the polymer can be removed to reveal a negative of the mould. It has been shown that some examples of closed chambers can be produced by assembling components through plasma bonding or using uncured elastomer

as an adhesive [131].

This method is suitable for limited life materials often used for experimental continuum devices. Its resolution is also limited by the minimum achievable feature size of the master mould. In practice, this usually requires a compromise between mould expense, production time, material suitability and resolution. Photolithographic techniques can be used to produce high resolution patterns, but production time and cost can be prohibitive. The accessibility of additive techniques/3D printing techniques has increased the use of master moulds due to low lead times and costs. However, resolution restrictions are often higher and several of the mould materials induce a reaction that inhibits curing of silicone elastomers.

Multi-material structures are also a challenge for soft lithography, with each change in material significantly adding to production time. Over-moulding higher stiffness materials is often used to introduce spatially varying mechanical characteristics and induce a bending bias during operation [68]. Selective inclusion of functional elements, such as conductive nano-particles, can only practically be achieved via homogenous distribution throughout the body.

Furthermore, the process is fundamentally 2.5D since the final device needs to be removed from the mould without damage. Lost wax and dissolvable moulds have been used to enhance the complexity of the designs, but their single use increases manufacturing timescales and expense. Creative designs have been important in allowing more complex behaviour in multi-link continuum robots. However limited achievable complexity using these mould based methods has led to direct additive or even hybrid techniques being increasingly investigated.

2.5.1.2 Direct Addictive Manufacture

Direct additive manufacture (AM) has been increasingly used to investigate the fabrication of continuum robots, rather than use as a template for secondary casting pro-

cesses [205; 206]. This provides enhanced design freedom and geometric complexity, as well as opportunities for true multi-material structures.

Central to all AM processes is the development of materials that are suitable for both the end application and the manufacturing process. Fused deposition modelling (FDM) and selective laser sintering (SLS) greatly limit the material choice, given the need for thermoplastics. In SLS, this is compounded by challenges in multi-material processing. Stereolithography (SLA) faces similar issues being limited to photopolymers. However, materials with properties approaching those of silicone rubber have been demonstrated [207]. Additionally, SLA's optical patterning allows greater feature resolution than competing extrusion processes. Controlled forms of material extrusion and material deposition processes are becoming increasingly popular in continuum robotics due to their ability to deposit high viscosity materials. However, it can be challenging to develop an ink that can flow easily out of the nozzle and maintain its shape once deposited. Currently, this is achieved by inducing a phase change through liquid evaporation, gelation, or temperature change [208]. Recently, rapid material switching has been demonstrated for spatially varying material composition or particle loading [209].

2.5.1.3 Hybrid Approaches

Techniques that combine soft lithography for the production of bulk geometries with direct write for the functional elements have expanded the capabilities of continuum devices. In these types of processes, the bulk material is cast into a mould before a selective deposition technique deposits an ink into the base materials. The secondary deposition process can be completed before or after curing of the bulk structure. The most widely investigated hybrid approach uses DIW to deposit fugitive, strain limiting, and conductive sensing elements within an uncured elastomer matrix [210]. Other approaches have used direct write approaches such as inkjet or aerosol jet to deposit onto a cured elastomer [211].

2.5.1.4 Magnetic Composites

Fabrication of magnetic continuum robotics is achieved with specific processes. As discussed in Section 2.4.3, a number of commercial steerable needle products are available in the market that rely on embedding permanent magnets within a soft or flexible structures [16]. These can be manufactured through either mechanical assembly[212] or over-moulding a polymer body around permanent magnets [167; 213]. These approaches illustrated some good applications but also have some limitations of scale of potential devices and their function. These devices have raised questions of robustness in light of a recall of a number of magnetically tipped steerable guide-wires [214].

Alternatively, manufacture of magnetic continuum robots can be based on micro or nano-particles within a polymer matrix. Reducing the size of the particles allows them to be positioned more densely while minimising the impact on the device's mechanical properties. Hard magnetic particles, characterised by high remanence, are limited to the micro-scale [215]. Soft magnetic materials can be synthesised at the nano-scale, however their relatively low remanence leads to a lesser response during actuation. Additionally, the total loading fraction needs to be carefully considered in terms of both the magnetic response and mechanical properties as the higher the concentration the higher the mechanical impact on the polymer [216]. Furthermore, limitations in bio-compatibility of the materials, alignment of the magnetic field, and processes that allow selective and spatial patterning within polymer bodies challenge the realisation of the full potential of magnetic continuum robotics. Nonetheless, processes for both types of magnetic particles have been presented that have made progress against these challenges.

2.5.1.4.1 Template aided magnetisation

Template aided magnetisation consists of holding a pre-formed magnetic elastomer composite sheet in a template. This is then magnetised through exposure to a large external field [217]. By locally controlling the orientation of the polymer body relative to the magnetising field, it is possible to induce a spatially varying magnetisation profile [59].

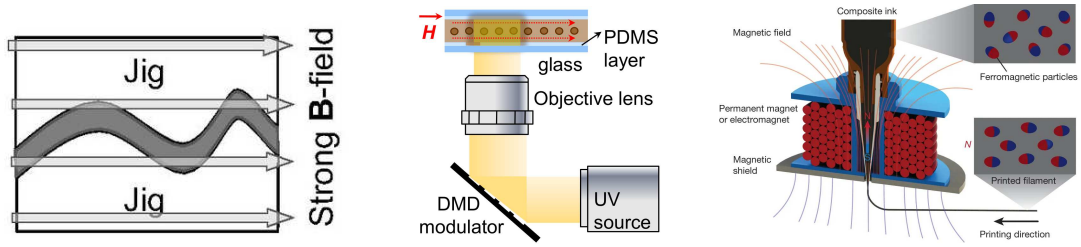

(a) (b) (c)

Figure 2.6: Examples of fabrication processes for magnetic composites. (a) Template aided magnetisation [218]; (b) Optical patterning process [219]; (c) Extrusion process of magnetic composites [220].

Over-moulding and other similar soft-lithographic techniques can be used to spatially vary the particle loading concentration and, therefore, the magnetic response. However, a substitute non-magnetic particle may need to be incorporated to maintain homogenous mechanical properties.

Despite the simple and easy process, this approach is limited to planar actuators and the use of templates prevents discrete changes in the magnetisation profile. More complex structures and magnetisation profiles require secondary assembly stages [218].

2.5.1.4.2 Optical patterning

Optical patterning utilises lithographic techniques to selectively cure a photopolymer resin loaded with magnetic particles [219]. The uncured resin is exposed to an external magnetic field which induces particle alignment. The resin is then selectively cured, locally fixing the position and orientation of the magnetic particles. The external field can then be adjusted to induce an alternate orientation in the uncured resin. Repetition of this process can pattern both the polymer matrix and the magnetisation profile in one single process.

A number of different techniques have been presented where their primary differences are in the types of particles used, the method of achieving selective light exposure (masked[220] or mask-less [171]), and the incorporation of additional process steps and components to induce further capabilities [220]. Early work used a permanent magnet to align magnetic particles before an ultraviolet light source selectively cured the polymer,

achieving 2D magnetisation profiles [219]. More recently, 3D magnetisation profiles were achieved by fixing the permanent magnet to a two DOF rotation axis mounted below the build volume [171]. Furthermore, improved magnetic response was also observed by using higher remanence magnetic materials.

Optical patterning is able to achieve 3D magnetisation profiles, providing greater freedom in magnetic response and device geometry when compared with the template based methods described previously. However, the mechanical properties of photocured polymers are often more restricted than those available to casting or extrusion processing. Additionally, particles in photopolymers can inhibit curing through UV absorbance. This may provide an upper bound to the maximum loading fraction produced by these methods.

2.5.1.4.3 Direct Inkjet Write

Direct Inkjet Write (DIW) of magnetically loaded materials has been demonstrated by incorporating high remanence microparticles within a polymer matrix [187]. The particles were magnetised to saturation within the suspension prior to extrusion. Additionally, fumed silica particles were added to drive the thixotropic behaviour required to prevent agglomeration during magnetisation and provide the required rheological conditions for DIW [221]. Microparticle alignment can be achieved by using a switchable magnet at the nozzle's exit or by bulk treating post print. Selective alignment during extrusion provides greater control and freedom over the magnetisation profile, however only 63-64% of the magnetic moment density can be achieved when compared to uniform magnetisation.

The addition of microparticles in DIW can often lead to increased instances of nozzle clogging. Robust DIW processes require a high nozzle-particle diameter ratio or a low loading fraction to achieve reliable deposition [208]. Since high remanence particles typically have a minimum diameter of 5μm, compromises between process resolution and magnetic response are currently required. The highest presented loading fraction is 20wt% significantly lower than the 50wt% demonstrated using casting techniques [221].

To summarise the state-of-the-art in CR fabrication, we can see that there are several areas of progress but that the processes that have been demonstrated to date typically

involve several elements of compromise across their functionality and/or their possible applications. In particular we currently see restrictions to the production of small scale CRs and their dexterity due to fabrication limitations in resolution and material composition. It should also be noted that many of the techniques described are also often not exceptionally scalable for high production rates or high manufacturing standards. There are also particularly significant hurdles for several of the methods with regards repeatability. Advancing beyond these issues is dependant of rationalising multi-step fabrication routes and employing digital-control and automation for their manufacture.

2.5.2 Modelling

In contrast with standard rigid-link manipulators, whose mechanical properties have been fully understood and discussed [222], continuum manipulators are still the subject of much debate within the robotics community in terms of modelling [117; 73] and control [223] (see the following Section 2.5.3).

The lack of generalised approaches makes understanding and usage of these manipulators less straightforward. In fact, continuum robots include a variety of concepts as discussed in previous sections. The non-negligible diversities of these robotic concepts hinder the development of possible unifying and more generalised modelling and control techniques. The differences between proposed actuation methods, as reported in Section 2.4, also make generalisations less trivial and induce extensive dispute. Furthermore, there is an increased difficulty due to the complex mechanical behaviour of these robots. Unlike rigid serial robots, one of the only common concepts among continuum robots is a lack of rigidity, this constitutes their main advantage in terms of application and their main drawback in terms of physical understanding and description. This lack of rigidity also leads to more complex relationships between actuators and End Effector (EE) dynamics. As such, modelling of continuum robots has received significant interest from the robotics community and several concepts have been emerging.

Kinematic modelling is, in general, not particularly effective in continuum robots owing

to the redundant design and general lack of rigid coupling between actuators and EE. With the possible exception of concentric tube robots [224] we could describe the physical behaviour of a continuum robot as the outcome of the equilibrium of internal forces (e.g. elasticity, damping, friction, etc.) and actuating external wrenches ($(f\ \tau)^T$ in Figure 2.7). As a result of this force balance, the continuum manipulator would shape itself to a minimal energy configuration. Therefore, models that consider static [225; 224; 226; 227] and dynamic [228; 229; 230; 117; 231; 231] approaches for controller design are particularly effective. Nevertheless, kinematics [73] and differential kinematics [232] approaches have also been investigated and may be of great interest for sensing (see Section 2.5.4).

Modelling techniques for continuum robots can be divided into: classical methods (such as Cosserat rod theory [71], constant curvature [73], rigid link models [232; 227]); combined methods [117; 194; 231; 231; 233; 228]; and emerging techniques [234; 226].

2.5.2.1 Classical methods

The classical methods applied to modelling of continuum robots can be subdivided in terms of strictness of their assumptions. In particular, Cosserat rod theory aims at solving the static equilibrium of the manipulator fully (Figure 2.7a) without simplifying assumptions; (piece-wise) constant curvature modelling assumes the robot shape fits the arc of one or more circles (Figure 2.7b); and rigid-link assumption would subdivide the robot into (infinitesimal) rigid links (Figure 2.7c). These techniques listed with increasing strictness of assumption and consequent ease in description lead to relative pros and cons, described in the following.

2.5.2.1.1 Cosserat Rod Theory

Cosserat Rod theory does not undergo specific assumptions and is, therefore, an exact solution to the statics of the continuum robot (see Figure 2.7a). This approach consists of solving a set of equilibrium equations between the position, orientation, internal force and internal torque of the robot [117].

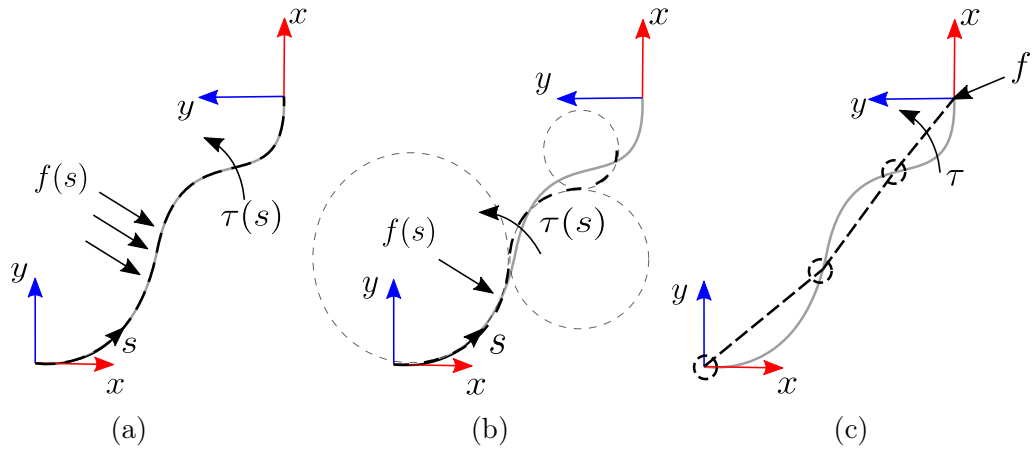

Figure 2.7: Schematic representation of the three classical modelling approaches of continuum robots (a) Cosserat rod model, (b) Piece-wise constant curvature, and (c) Rigid-link model. $f(s)$ and $\tau(s)$ represent the vector fields force and torque with respect to the robot's length (s), respectively.

Despite the exact solution given, it suffers from drawbacks that prohibit wide use. There are difficulties in extending to dynamics since it would involve the solution of a system of Partial Differential Equations [235]. Moreover, the solution of this approach is to be computed numerically, leading to high complexity and computational expense and a lack of a closed-form solution.

2.5.2.1.2 Constant Curvature

Constant curvature models are based on the assumption that the continuum robot deflects as arcs of a circle, as represented in Figure 2.7b. This constitutes a significant simplification when compared to Cosserat Rod and leads to possible analytical solutions for kinematics [233], statics [230] and dynamics [229]. In Figure 2.7b, we represent *piece-wise constant curvature* modelling, i.e. the robot is modelled as a series of links that can deflect with constant curvature. Assuming constant curvature only, even if widely used, is more restrictive.

Even if piece-wise constant curvature modelling may constitute a valuable trade-off between the complications of Cosserat rod theory and the assumptions of rigid-link models, most of the literature has focused on the single constant curvature [233; 229] without exploiting the larger generalization provided by combining constant curvature segments [230; 236]. This would be of great value, especially due to the possible extension

to dynamic modelling [229] and the reduction of numerical intensity with respect to rigid-link approaches.

As underlined in Figure 2.7b, one of the drawbacks may be constituted by the lack of compliance to the constant curvature assumption with possible consequent deviation from the real robot's behaviour. Extension to the polynomial curvature case has also been recently proposed [237]. However, further experimental analysis and discussion of its application is needed.

2.5.2.1.3 Rigid-link Model

Assuming a continuum robot can be divided into (small enough) segments [232; 227], behaving as rigid links (see Figure 2.7c), is a significant assumption when dealing with continuum structures. This would either lead to behaviours which are far from reality (few segments) or a very large number of variables (many segments). Employing the rigid-link assumption is a useful simplification since it permits the use of well-established approaches for control and sensing [222].

In the presence of sensing [232] (see Section 2.5.4), the simplifications related to the usage of this model may be mitigated and compensated by the measure of the robot's behaviour. Therefore, the designer may find a balance between model and sensing complexity to find an optimal approach.

2.5.2.2 Combined methods

Due to the continuously emerging design, fabrication and actuation methods for CMs, single model approaches are of limited use. In fact, depending on the type of actuation, models need to be a combination of the intrinsic robot's behaviour and actuation dynamics. In this case, the wrench we previously defined as extrinsic becomes an integrated module of the robot's model.

Large interest since the early days of continuum robotics has been paid to backbone continuum robots [228; 117; 238; 231; 232] (see Section 2.4.1). Due to the contact be-

tween cables and discs, several authors have combined friction models with discs dynamic model [231; 238]; and with the constant curvature model [228].

In the last few years, interest towards magnetically actuated catheters has soared [225; 194; 227]. Here an extrinsic wrench is generated as a consequence of the interaction between internal magnetised agents. In general, the considered models are a combination of the dipole model [50; 239] with rigid-link model [227] or with Cosserat rod model [225; 194]. As far as the authors are aware, combinations with piece-wise constant curvature models have not yet been investigated; although, they may be promising, owing to the possible existence of an analytical solution to the combination of dipole model and constant curvature model.

2.5.2.3 Emerging Techniques

The previously described modelling approaches, given the very novel nature of continuum robots, are not without drawbacks. Therefore, new paradigms for modelling continuum robots have recently been investigated.

In particular, in [234] the authors attempt to overcome the limitations of constant curvature modelling by substituting circular curves with *Euler curves* which proved to be a better fit for a pneumatic continuum robot. In [226], the authors employ a quasi-static approach based on optimal configurations taking inspiration from optimal non-linear control. Despite the promising results, the lack of analytical solution and the difficulties in generalising the dynamic modelling are the main drawbacks of this approach.

Even if, intuitively, research should be driven by the quest for more and more accurate modelling approaches, accuracy is generally paid for with computational burden. This expense, given the interest towards models for real-time control over simulation for design, is a fundamental parameter to consider in the choice and/or investigation of a modelling approach. Moreover, control is generally based on both model and sensors (see Section 2.5.4) and the aim of the designer is the balance between these two compo-

nents. Therefore, we expect research to evolve towards more affine-to-control modelling approaches [236; 237] with the mindset of complexity mitigation.

2.5.3 Control

Control is one of the fundamental aspects of any robotic platform since it gives significance to the mechanical properties of any autonomous system. Interestingly though, only 9% of researchers seem to be focused on this topic within soft continuum robots [223]. This could be interpreted both as a consequence of the large interest in other aspects of CRs, such as mechanical design, or equally related to the very limited knowledge in terms of modelling (see Section 2.5.2) and sensing (see Section 2.5.4). In fact, to achieve accurate control, both these aspects are fundamental, even though the presence of a human-in-the-loop - as found in medical robotics - may mitigate some shortcomings [90].

The lack of accurate or appropriate sensing mechanisms in certain situations has led researchers to differentiate between open loop, which is based on model inversion; closed loop based on feedback of the robot's actuator; and feed-forward and feedback combined control [223]. Despite the effectiveness of this partition, the last two classes can be grouped more generally within the closed loop control class [240] with their differences related to being model-based and model-free.

Control in continuum robots can be divided into: kinematic and differential kinematic control [241; 242; 243; 244]; adaptive and learning-based approaches [245; 246; 247; 248; 249; 250; 251; 252]; and wrench-based controllers [225; 253; 254; 255; 256; 257; 258].

2.5.3.1 Kinematic Approaches

Kinematic approaches include any controller that considers the inverse kinematics or inverse differential kinematics, under the clear assumption that any controller needs knowledge of the direct kinematics. The application of inverse kinematics is the most widely used approach to controlling robots and considered straightforward for standard

robots [259]. Due to the highly redundant design of continuum robots, inverse kinematics is not particularly effective [241]. In fact, kinematics is generally not bijective for redundant manipulators and infinite solutions exist for the inverse kinematics [222]. Nevertheless, a large amount of research has recently focused on learning inverse kinematics.

Differential kinematics [243], on the other hand, is particularly effective with redundant manipulators, since it allows multi-task control [223]. A good example of such cases is the dual-arm concentric tube coordinated control [242]. Assuming the differential kinematics to be known with sufficient accuracy can be a relatively strong assumption given the modelling approximations designers are forced into. Satisfactory accuracy might not therefore be assured. To overcome this limitation, adaptive approaches have been proved effective in some scenarios.

2.5.3.2 Adaptive and Learning Approaches

To deal with partial knowledge of the robots (differential) kinematics, some authors have started investigating adaptive and learning approaches, which are aimed at compensating for modelling approximations with data gathering. These approaches can be subdivided into mechanical adaptation methods and learning-based methods. The former are generally based on some approximated mathematical model for the manipulator and aim at real-time adaptation of the approximations; the latter are data-driven modelling approaches.

2.5.3.2.1 Adaptive Approach

This approach is generally applied to approximated models, whose inaccuracies can be mitigated by the presence of a feedback loop. The problem is tackled as the estimation of the mechanical parameters is done on-line. In particular, the approach in [251] describes the robot's pose as a Fourier series expansion and a recursive least square approach is applied to update the parameters. More satisfactory results were found by applying a locally weighted projection regression, by approximating the model with a collection

of linear models and adaptation performed by means of a stochastic gradient descent approach [252].

A different approach has been recently presented in [250], with the application of a model-free adaptive controller based on visual servoing. Another approach considers the adaptive observer of a Kalman filter [249], designed to estimate the Jacobian matrix of the manipulator. However, the model of state evolution is relatively simple and does not consider the mathematical properties of the Jacobian matrix.

2.5.3.2.2 Learning Approach

More recently, modelling and control based on machine learning methodologies has gained much interest amongst the robotics community. These methods, as with the previously mentioned adaptive counterpart, have the common aim of avoiding complex and approximated analytical models. In particular, contrived mechanical response models can be replaced with data-driven model-free simulations. Examples of such strategies appear in [245] which uses a multilayer perceptron with a single hidden layer, the multilayer network employed in [246; 188], and a modified Elman Neural Network and Gaussian Mixture Model in [248]. Despite some promising results and the recent surge in the application of learning techniques to robotics, a limitation of these methods is the blindness to real mechanical interactions. This lack of physical significance endorses a lack of underlying physical comprehension, this in turn can produce an un-auditable system and may lead to potentially hazardous undetected inaccuracies.

2.5.3.3 Wrench-based Approaches

Since the actuation of a continuum robot can be generally related to the interaction between their flexible structure and actuating (external) wrenches (see Section 2.5.2 for more details), some authors have tackled the control problem by directly controlling the actuating wrench. Some examples are the static approaches in [225; 254; 257] and dynamic approaches in [258].

As an outcome of this vision, due to the redundant nature of continuum robots, compliance/stiffness [253; 257] and task-space force [254] control have been investigated. This is of primary importance for some medical robotics tasks, such as smooth navigation in soft environments and palpation [256]. Nevertheless, the estimation of a robot's force is not trivial without the assistance of sensors. Therefore, [117] and [256] have independently worked on the estimation of the force by applying a probabilistic and deterministic approach, respectively.

Literature on control of CMs shows significant interest in model-based approaches. Given the complex mechanical behaviour of CMs and the need for several diverse and interconnected elements (see Section 2.5.1) in their design, mechanical characterization may lack accuracy and thus induce errors in control. We therefore envisage that other methods, such as adaptive methods or deep learning, will be implemented to compensate for this drawback.

2.5.4 Sensing

As stated previously, accurately modelling CMs remains a huge challenge, reinforcing the need to further develop techniques to improve controllability, actuation and safety. Real-time shape sensing of CMs allows for more precise and reliable motion control. To date there are three main types of shape sensing employed in CMs: optical sensing, electromagnetic tracking, and imaging techniques.

2.5.4.1 Optical based shape sensing

Optical sensing is based on the use of fibre Bragg grating (FBG) sensors written onto optical fibres. These are able to reflect a narrow range of the full spectrum of input light depending on the fibre's strain and temperature [260]. This way, by incorporating several FBG sensors along an optical fibre it is possible to estimate the shape given the strain measurements at each sensor. Consequently, embedding one or more optical fibres with FBGs in CMs enables shape sensing of the device.

The popularity of this method has been increasing in continuum structures, especially those which undergo small deflections. Needles are one of the most common structures where this sensing method has been employed. Needles are inherently stiff, supporting a nearly perfect strain transfer to the attached FBGs. Three optical fibres with two FBGs each have been reported to give very accurate results for single 2D deflections [261]. However, as the deflection complexity increases to double deflections [262], or 3D deflections [260], the inaccuracy increases significantly. The main sources of errors have been attributed to a low number of sensors and their inaccurate placement during fabrication. Additionally, the location of the FBGs has also been reported to have a fundamental role [261; 262].

This sensing technique has also been used on less stiff structures such as catheters [263; 264; 265] and endoscopes [266; 267]. These structures are more challenging due to the lower strain transfers onto the sensors. In fact, preliminary work on the field was not able to achieve accurate results [266] or had to be used in combination with other sensing techniques [264] such as those reviewed here. Recently 3D shape reconstruction of catheters was achieved using multi-core fibres [265].

Overall, using FBGs sensors for shape sensing of CMs is a viable solution, especially for structures that undergo small deflections. Furthermore, its usage on force and torsion sensing has also been demonstrated, allowing higher sensing capabilities without the need of extra equipment [268; 269; 270; 271]. Its insensitivity to magnetic fields allows its usage in a variety of medical situations such as MRI or coupled to magnetically actuated devices. Nevertheless, the technology still faces significant challenges that hinder its mainstream use, especially in high deflection structures. Not only will the sensors give less accurate results due to a lower strain transfer ratio but they will also damage easily when subjected to such strains. This imposes strict limitations to the devices that are suitable for this type of shape sensing. Additionally, the relatively high cost of such technology hinders its application in low cost devices. The number of sensors and their placement are also shown to have a major impact on results [272; 273].

2.5.4.2 Electromagnetic tracking based shape reconstruction

Electromagnetic (EM) tracking uses mutual induction between a magnetic field generator and a magnetic field sensor for shape reconstruction. Two variations of this method have been proposed based on the location of the magnetic field generator, either external or internal to the robot.

External methods are the most common and use commercially available EM tracking systems, such as the NDI Aurora [274], for shape reconstruction. These systems are able to determine the pose of small sensors on a generated external magnetic field. By placing these sensors along the robot, the system is able to determine the robot's pose. The usage of these systems for shape sensing has been widely demonstrated [275; 276], and methods to estimate contact force have also been reported [277; 278]. Despite its promising results, this method is constrained by the limitations of the localisation method itself, such as limited workspace and variable accuracy within it [276].

Internal methods are able to overcome these limitations by placing the source of the magnetic field inside the robot itself. Two small permanent magnets alternated with two Hall effect sensors along a CM were able to reconstruct 2D shape [279]. By measuring the magnetic field at the location of the Hall effect sensors, it is possible to estimate the relative position, and therefore, the deflection of the manipulator. Similar approaches have been reported [280; 281; 282] and a common limitation to them all is that with increasing deflections, the errors increase. This is due to cross talk between the sensors and the magnets, posing limitations to minimum bending radii.

Electromagnetic tracking shape sensing methods are able to provide freedom from line-of-sight restrictions and are relatively easy to incorporate into the robot. However, they are highly susceptible to magnetic disturbances from nearby equipment. External methods using commercially available systems cannot be used in conjunction with magnetically actuated robots or MRI applications [283]. Nonetheless, proprietary localisation methods could be developed for the specific application and robot, such as [49]. Internal methods

suffer from crosstalk between sensors and magnetic agents during high deformations, hindering the reliability of shape estimation results. Furthermore, the incorporation of an internal magnetic field generator can impose limitations on the robot's size. Nevertheless, assuming these challenges are addressed, this method could potentially achieve much smaller bending radii than FBG, facilitating its use in soft CRs.

2.5.4.3 Imaging based shape estimation

Imaging methods rely on current medical imaging techniques to track and estimate the shape of CMs. Unlike the previous methods, this approach does not required the integration of any additional sensors onto the surgical instrument which can be beneficial from a design and miniaturisation point of view.

Fluoroscopy [284; 285; 266] and ultrasound [285; 286] are the two main imaging techniques used in shape estimation of CMs and endoscopes. The usage of biplane fluoroscopy for shape estimation of continuum structures has been reported and is known to achieve accurate 3D reconstructions [287; 163]. However, these methods depend on biplane systems that are associated with large radiation dosages and costs. Given the nature of monoplane fluoroscopy, detecting out of plane deflection using imaging alone is not possible [288]. Several works have combined planar imaging techniques with tracking methods [289; 288; 290] or kinematic modelling [291; 292] however these systems tend to achieve less accurate results. Shape estimation of CMs using endoscopic cameras has also been reported and is generally performed on a marker-based or markerless approach [293; 294]. Marker-based approaches require additional integration of components into the device, while markerless require large manually labelled training sets [294]. Furthermore, these methods are normally limited by the field of view of the camera.

Imaging based methods can provide reliable results for shape sensing of CMs. There are no limitations to the minimum bending radii these methods can potentially achieve, unlike alternatives methods which, for larger deflections, can become erroneous. They are limited of course by image resolution, noise and processing techniques. Furthermore,

due to their dependency on, and need for integration with, hospital equipment, they may not be readily implemented.

In summary, recent developments in shape sensing for CMs has improved their efficacy. However, when introducing additional on-board hardware, as in FBG and EM tracking approaches, robot miniaturisation, stiffness, flexibility and durability can be adversely influenced. Off-board sensing methods remove such restrictions, and of these, imaging-based methods are most prevalent, offering potentially practicable solutions to the sensing problem if suitable clinical integration can be realised. A less explored but promising off-board approach employs load cell sensors located at the robot's proximal end for estimation of tip force and shape [295; 296]. Ultimately, the limited accuracy of flexible and soft robots, particularly when subject to interaction forces, hinders their reliability in clinical settings. Methods for shape sensing are therefore essential to realise the full potential of medical CRs, and future development may engender ever smaller bending radii measurement, while maintaining high accuracy and miniaturisation capabilities.

2.6 Conclusions and Future directions

Medical robotics has seen remarkable innovation over the last decades. Driven by the need for less invasive procedures while maintaining dexterity levels, continuum robots have established themselves as a viable alternative to traditional rigid-link manipulators. The recent commercial releases of continuum platforms for robot-assisted procedures further advocate their future place in advanced healthcare practices.

Despite the progress achieved, further advancements are highly dependent on current challenges across actuation, fabrication, control, and sensing. As with traditional surgical robotic systems, continuum robots are commonly intrinsically actuated using tendons or pressurised fluids, limiting the achievable DOF as their size reduces. External actuation via magnetic fields does not suffer from this scaling issue, providing a promising approach for controlling continuum robotic devices, especially at the small scales required for medical applications. Magnetic soft robots may provide an optimal solution as they

are able to combine the freedom in scale from magnetism with the safe interaction of soft robots.

Fabrication and control of such devices is currently still a challenge given the materials employed and the magnetisation patterns needed for actuation. However, allied to these challenges is also the possibility for major breakthroughs. Developments in digitally-driven and computer controlled manufacturing processes holds potential to allow an exciting next generation of continuum robots, with greater resolution and dexterity, enabling us to reach and treat areas of the human anatomy that may otherwise be inaccessible.

Bibliography

[1] G. D. Baura, *Medical Device Technologies*. Oxford: Academic Press, 2012.

[2] F. Doglietto, D. M. Prevedello, J. A. Jane, J. Han, and E. R. Laws, "A brief history of endoscopic transsphenoidal surgery—from Philipp Bozzini to the First World Congress of Endoscopic Skull Base Surgery," *Neurosurgical Focus FOC*, vol. 19, no. 6, pp. 1–6, 2005.

[3] A. R. Mundy, J. Fitzpatrick, D. E. Neal, and N. J. R. George, *The scientific basis of urology*. London: CRC Press, 2010.

[4] B. S. Peters, P. R. Armijo, C. Krause, S. A. Choudhury, and D. Oleynikov, "Review of emerging surgical robotic technology," *Surgical Endoscopy*, vol. 32, no. 4, pp. 1636–1655, 2018.

[5] S. S. Kim and T. R. Donahue, "Laparoscopic Cholecystectomy," *JAMA*, vol. 319, no. 17, p. 1834, 2018.

[6] E. Rozeboom, J. Ruiter, M. Franken, and I. Broeders, "Intuitive user interfaces increase efficiency in endoscope tip control," *Surgical endoscopy*, vol. 28, no. 9, pp. 2600–2605, 2014.

[7] N. Simaan, R. M. Yasin, and L. Wang, "Medical Technologies and Challenges of

Robot-Assisted Minimally Invasive Intervention and Diagnostics," *Annual Review of Control, Robotics, and Autonomous Systems*, vol. 1, no. 1, pp. 465–490, 2018.

[8] B. M. Wolfe, B. Gardiner, and C. F. Frey, "Laparoscopic Cholecystectomy: A Remarkable Development," *JAMA*, vol. 314, no. 13, p. 1406, 2015.

[9] R. H. Taylor, A. Menciassi, G. Fichtinger, P. Fiorini, and P. Dario, "Medical Robotics and Computer-Integrated Surgery," in *Springer Handbook of Robotics* (B. Siciliano and O. Khatib, eds.), pp. 1657–1684, Cham: Springer International Publishing, 2016.

[10] B. Davies, "A review of robotics in surgery," *Proceedings of the Institution of Mechanical Engineers, Part H: Journal of Engineering in Medicine*, vol. 214, no. 1, pp. 129–140, 2000.

[11] Intuitive Surgical, "Annual Report 2018," tech. rep., Intuitive Surgical, 2018.

[12] S. U. Bae, W. K. Jeong, and S. K. Baek, "Current status of robotic single-port colonic surgery," *The International Journal of Medical Robotics and Computer Assisted Surgery*, vol. 13, no. 1, p. e1735, 2017.

[13] P. K. Singh and C. M. Krishna, "Continuum arm robotic manipulator: A review," *Universal Journal of Mechanical Engineering*, vol. 2, no. 6, pp. 193–198, 2014.

[14] J. Faulkner and S. Dirven, "A generalised, modular, approach for the forward kinematics of continuum soft robots with sections of constant curvature," in *2017 24th International Conference on Mechatronics and Machine Vision in Practice (M2VIP)*, pp. 1–6, 2017.

[15] C. Heunis, J. Sikorski, and S. Misra, "Flexible Instruments for Endovascular Interventions: Improved Magnetic Steering, Actuation, and Image-Guided Surgical Instruments," *IEEE robotics & automation magazine*, vol. 25, no. 3, pp. 71–82, 2018.

[16] X. Hu, A. Chen, Y. Luo, C. Zhang, and E. Zhang, "Steerable catheters for mini-

mally invasive surgery: a review and future directions," *Computer Assisted Surgery*, vol. 23, no. 1, pp. 21–41, 2018.

[17] J. Burgner-Kahrs, D. C. Rucker, and H. Choset, "Continuum Robots for Medical Applications: A Survey," 2015.

[18] C. Shi, X. Luo, P. Qi, T. Li, S. Song, Z. Najdovski, T. Fukuda, and H. Ren, "Shape Sensing Techniques for Continuum Robots in Minimally Invasive Surgery: A Survey," *IEEE Transactions on Biomedical Engineering*, vol. 64, no. 8, pp. 1665–1678, 2017.

[19] A. Hong, Q. Boehler, R. Moser, A. Zemmar, L. Stieglitz, and B. J. Nelson, "3D path planning for flexible needle steering in neurosurgery," *The International Journal of Medical Robotics and Computer Assisted Surgery*, vol. 15, no. 4, p. e1998, 2019.

[20] E. Calabrese, "Diffusion Tractography in Deep Brain Stimulation Surgery: A Review," *Frontiers in neuroanatomy*, vol. 10, p. 45, 2016.

[21] A. Lindgren, M. D. I. Vergouwen, I. van der Schaaf, A. Algra, M. Wermer, M. J. Clarke, and G. J. E. Rinkel, "Endovascular coiling versus neurosurgical clipping for people with aneurysmal subarachnoid haemorrhage," *Cochrane Database of Systematic Reviews*, no. 8, 2018.

[22] C. Neudorfer, S. Hunsche, M. Hellmich, F. El Majdoub, and M. Maarouf, "Comparative Study of Robot-Assisted versus Conventional Frame-Based Deep Brain Stimulation Stereotactic Neurosurgery," *Stereotactic and Functional Neurosurgery*, vol. 96, no. 5, pp. 327–334, 2018.

[23] A. J. Petruska, F. Ruetz, A. Hong, L. Regli, O. Surucu, A. Zemmar, and B. J. Nelson, "Magnetic needle guidance for neurosurgery: Initial design and proof of concept," in *2016 IEEE International Conference on Robotics and Automation (ICRA)*, pp. 4392–4397, Institute of Electrical and Electronics Engineers Inc., 2016.

[24] R. L. Siegel, K. D. Miller, and A. Jemal, "Cancer statistics, 2019," *CA: A Cancer Journal for Clinicians*, vol. 69, no. 1, pp. 7–34, 2019.

[25] National Institute for Health and Care Excellence, "Lung cancer: diagnosis and management," *NICE Guideline 122*, 2019.

[26] P. J. Swaney, A. W. Mahoney, B. I. Hartley, A. A. Remirez, E. Lamers, R. H. Feins, R. Alterovitz, and R. J. Webster III, "Toward Transoral Peripheral Lung Access: Combining Continuum Robots and Steerable Needles," *Journal of medical robotics research*, vol. 2, p. 1750001, mar 2017.

[27] A. Hindman, "Robotic Bronchoscopy," *Oncology Issues*, vol. 34, no. 2, pp. 16–20, 2019.

[28] D. Fielding, F. Bashirzadeh, J. H. Son, M. Todman, H. Tan, A. Chin, K. Steinke, and M. Windsor, "First human use of a new robotic-assisted navigation system for small peripheral pulmonary nodules demonstrates good safety profile and high diagnostic yield," *Chest*, vol. 152, no. 4, p. A858, 2017.

[29] E. Folch, M. Pritchett, J. Reisenauer, D. Ost, A. Majid, S. Fernandez-Bussy, C. Keyes, M. Parikh, J. Diaz-Mendoza, R. Casal, *et al.*, "A prospective, multi-center evaluation of the clinical utility of the ion endoluminal system-experience using a robotic-assisted bronchoscope system with shape-sensing technology," in *A110. ADVANCES IN INTERVENTIONAL PULMONOLOGY*, pp. A2719–A2719, American Thoracic Society, 2020.

[30] J. Y. Chan, E. W. Wong, R. K. Tsang, F. C. Holsinger, M. C. Tong, P. W. Chiu, and S. S. Ng, "Early results of a safety and feasibility clinical trial of a novel single-port flexible robot for transoral robotic surgery," *European Archives of Oto-Rhino-Laryngology*, vol. 274, no. 11, pp. 3993–3996, 2017.

[31] L. Manfredi, E. Capoccia, G. Ciuti, and A. Cuschieri, "A Soft Pneumatic Inchworm Double balloon (SPID) for colonoscopy," *Scientific reports*, vol. 9, no. 1, pp. 1–9, 2019.

[32] S. Mattheis, P. Hasskamp, L. Holtmann, C. Schäfer, U. Geisthoff, N. Dominas, and

S. Lang, "Flex robotic system in transoral robotic surgery: the first 40 patients," *Head & neck*, vol. 39, no. 3, pp. 471–475, 2017.

[33] J. B. Gafford, S. Webster, N. Dillon, E. Blum, R. Hendrick, F. Maldonado, E. A. Gillaspie, O. B. Rickman, S. D. Herrell, and R. J. Webster, "A Concentric Tube Robot System for Rigid Bronchoscopy: A Feasibility Study on Central Airway Obstruction Removal," *Annals of biomedical engineering*, pp. 1–11, 2019.

[34] W. Gong, J. Cai, Z. Wang, A. Chen, X. Ye, H. Li, and Q. Zhao, "Robot-assisted coronary artery bypass grafting improves short-term outcomes compared with minimally invasive direct coronary artery bypass grafting," *Journal of thoracic disease*, vol. 8, no. 3, p. 459, 2016.

[35] L. W. Nifong, W. R. Chitwood, P. S. Pappas, C. R. Smith, M. Argenziano, V. A. Starnes, and P. M. Shah, "Robotic mitral valve surgery: A United States multicenter trial," *The Journal of Thoracic and Cardiovascular Surgery*, vol. 129, no. 6, pp. 1395–1404, 2005.

[36] C. V. Riga, C. D. Bicknell, A. Rolls, N. J. Cheshire, and M. S. Hamady, "Robot-assisted fenestrated endovascular aneurysm repair (fevar) using the magellan system," *Journal of Vascular and Interventional Radiology*, vol. 24, no. 2, pp. 191–196, 2013.

[37] W. Clements, M. Scicchitano, J. Koukounaras, T. Joseph, and G. S. Goh, "Use of the magellan robotic system for conventional transarterial chemoembolization (ctace): A 6-patient case series showing safety and technical success," *Journal of Clinical Interventional Radiology ISVIR*, vol. 3, no. 02, pp. 142–146, 2019.

[38] F. Thaveau, P. Nicolini, B. Lucereau, Y. Georg, A. Lejay, and N. Chakfe, "Associated da vinci and magellan robotic systems for successful treatment of nutcracker syndrome," *Journal of Laparoendoscopic & Advanced Surgical Techniques*, vol. 25, no. 1, pp. 60–63, 2015.

[39] V. M. Pereira, N. M. Cancelliere, P. Nicholson, I. Radovanovic, K. E. Drake, J.-M.

Sungur, T. Krings, and A. Turk, "First-in-human, robotic-assisted neuroendovascular intervention," *Journal of NeuroInterventional Surgery*, vol. 12, no. 4, pp. 338–340, 2020.

[40] N. Lo, J. A. Gutierrez, and R. V. Swaminathan, "Robotic-assisted percutaneous coronary intervention," *Current treatment options in cardiovascular medicine*, vol. 20, no. 2, p. 14, 2018.

[41] F. Carpi and C. Pappone, "Stereotaxis Niobe® magnetic navigation system for endocardial catheter ablation and gastrointestinal capsule endoscopy," *Expert review of medical devices*, vol. 6, no. 5, pp. 487–498, 2009.

[42] J. Bonatti, G. Vetrovec, C. Riga, O. Wazni, and P. Stadler, "Robotic technology in cardiovascular medicine," *Nature Reviews Cardiology*, vol. 11, no. 5, p. 266, 2014.

[43] G. Fagogenis, M. Mencattelli, Z. Machaidze, B. Rosa, K. Price, F. Wu, V. Weixler, M. Saeed, J. Mayer, and P. Dupont, "Autonomous robotic intracardiac catheter navigation using haptic vision," *Science robotics*, vol. 4, no. 29, p. eaaw1977, 2019.

[44] E. C. Smyth, M. Verheij, W. Allum, D. Cunningham, A. Cervantes, and D. Arnold, "Gastric cancer: ESMO Clinical Practice Guidelines for diagnosis, treatment and follow-up," *Annals of oncology*, vol. 27, no. 5, pp. v38–v49, 2016.

[45] N. J. Shaheen, G. W. Falk, P. G. Iyer, and L. B. Gerson, "ACG clinical guideline: diagnosis and management of Barrett's esophagus," *The American journal of gastroenterology*, vol. 111, no. 1, p. 30, 2016.

[46] P. Valdastri, M. Simi, and R. J. Webster III, "Advanced technologies for gastrointestinal endoscopy," *Annual review of biomedical engineering*, vol. 14, pp. 397–429, 2012.

[47] G. Iddan, G. Meron, A. Glukhovsky, and P. Swain, "Wireless capsule endoscopy," *Nature*, vol. 405, no. 6785, p. 417, 2000.

[48] S. A. Bynum, J. L. Davis, B. L. Green, and R. V. Katz, "Unwillingness to participate

in colorectal cancer screening: examining fears, attitudes, and medical mistrust in an ethnically diverse sample of adults 50 years and older," *American journal of health promotion : AJHP*, vol. 26, no. 5, pp. 295–300, 2012.

[49] A. Z. Taddese, P. R. Slawinski, M. Pirotta, E. De Momi, K. L. Obstein, and P. Valdastri, "Enhanced real-time pose estimation for closed-loop robotic manipulation of magnetically actuated capsule endoscopes," *The International journal of robotics research*, vol. 37, no. 8, pp. 890–911, 2018.

[50] G. Pittiglio, L. Barducci, J. W. Martin, J. C. Norton, C. A. Avizzano, K. L. Obstein, and P. Valdastri, "Magnetic Levitation for Soft-Tethered Capsule Colonoscopy Actuated With a Single Permanent Magnet: A Dynamic Control Approach," *IEEE Robotics and Automation Letters*, vol. 4, no. 2, pp. 1224–1231, 2019.

[51] D. Turiani Hourneaux de Moura, H. Aihara, P. Jirapinyo, G. Farias, K. E. Hathorn, A. Bazarbashi, A. Sachdev, and C. C. Thompson, "Robot-assisted endoscopic submucosal dissection versus conventional ESD for colorectal lesions: outcomes of a randomized pilot study in endoscopists without prior ESD experience (with video)," *Gastrointestinal Endoscopy*, vol. 90, no. 2, pp. 290–298, 2019.

[52] P. Valdastri, R. J. Webster III, C. Quaglia, M. Quirini, A. Menciassi, and P. Dario, "A New Mechanism for Mesoscale Legged Locomotion in Compliant Tubular Environments," *IEEE Transactions on Robotics*, vol. 25, no. 5, pp. 1047–1057, 2009.

[53] D. Son, M. D. Dogan, and M. Sitti, "Magnetically actuated soft capsule endoscope for fine-needle aspiration biopsy," in *2017 IEEE International Conference on Robotics and Automation (ICRA)*, pp. 1132–1139, 2017.

[54] A. Rosemurgy, S. Ross, T. Bourdeau, D. Craigg, J. Spence, J. Alvior, and I. Sucandy, "Robotic Pancreaticoduodenectomy Is the Future: Here and Now," *Journal of the American College of Surgeons*, vol. 228, no. 4, pp. 613–624, 2019.

[55] P. C. Giulianotti, F. M. Bianco, D. Daskalaki, L. F. Gonzalez-Ciccarelli, J. Kim, and

E. Benedetti, "Robotic liver surgery: technical aspects and review of the literature," *Hepatobiliary surgery and nutrition*, vol. 5, no. 4, pp. 311–321, 2016.

[56] F. Coccolini, F. Catena, M. Pisano, F. Gheza, S. Fagiuoli, S. Di Saverio, G. Leandro, G. Montori, M. Ceresoli, D. Corbella, M. Sartelli, M. Sugrue, and L. Ansaloni, "Open versus laparoscopic cholecystectomy in acute cholecystitis. Systematic review and meta-analysis," *International Journal of Surgery*, vol. 18, pp. 196–204, 2015.

[57] J. Ahmed, M. Nasir, K. Flashman, J. Khan, and A. Parvaiz, "Totally robotic rectal resection: an experience of the first 100 consecutive cases," *International journal of colorectal disease*, vol. 31, no. 4, pp. 869–876, 2016.

[58] A. D'Argentré, S. Perry, Y. Iwata, H. Iwasaki, E. Iwase, A. Fabozzo, I. Will, D. Rus, D. D. Damian, and S. Miyashita, "Programmable Medicine: Autonomous, Ingestible, Deployable Hydrogel Patch and Plug for Stomach Ulcer Therapy," in *2018 IEEE International Conference on Robotics and Automation (ICRA)*, pp. 1511–1518, 2018.

[59] W. Hu, G. Z. Lum, M. Mastrangeli, and M. Sitti, "Small-scale soft-bodied robot with multimodal locomotion," *Nature*, vol. 554, p. 81, jan 2018.

[60] S. Yim, K. Goyal, and M. Sitti, "Magnetically actuated soft capsule with the multimodal drug release function," *IEEE/ASME Transactions on Mechatronics*, vol. 18, no. 4, pp. 1413–1418, 2013.

[61] K. K. Badani, S. Kaul, and M. Menon, "Evolution of robotic radical prostatectomy: assessment after 2766 procedures," *Cancer*, vol. 110, no. 9, pp. 1951–1958, 2007.

[62] D. K. Nanigian, W. Smith, and L. M. Ellison, "Robot-assisted laparoscopic nephroureterectomy," *Journal of endourology*, vol. 20, no. 7, pp. 463–466, 2006.

[63] N. Sarli, T. Marien, C. R. Mitchell, G. Del Giudice, M. S. Dietrich, S. D. Herrell, and N. Simaan, "Kinematic and experimental investigation of manual resection tools for transurethral bladder tumor resection," *The International Journal of Medical Robotics and Computer Assisted Surgery*, vol. 13, no. 2, p. e1757, 2017.

[64] N. Sarli, G. Del Giudice, S. De, M. S. Dietrich, S. D. Herrell, and N. Simaan, "Preliminary porcine in vivo evaluation of a telerobotic system for transurethral bladder tumor resection and surveillance," *Journal of endourology*, vol. 32, no. 6, pp. 516–522, 2018.

[65] R. J. Hendrick, C. R. Mitchell, S. D. Herrell, and R. J. Webster III, "Hand-held transendoscopic robotic manipulators: A transurethral laser prostate surgery case study," *The International journal of robotics research*, vol. 34, no. 13, pp. 1559–1572, 2015.

[66] M. A. Ahmad, M. Ourak, C. Gruijthuijsen, J. Legrand, T. Vercauteren, J. Deprest, S. Ourselin, and E. Vander Poorten, "Design and shared control of a flexible endoscope with autonomous distal tip alignment," in *2019 19th International Conference on Advanced Robotics (ICAR)*, pp. 647–653, IEEE, 2019.

[67] M. A. Ahmad, M. Ourak, C. Gruijthuijsen, J. Deprest, T. Vercauteren, and E. Vander Poorten, "Deep learning-based monocular placental pose estimation: towards collaborative robotics in fetoscopy," *International Journal of Computer Assisted Radiology and Surgery*, pp. 1–11, 2020.

[68] D. Rus and M. T. Tolley, "Design, fabrication and control of soft robots," *Nature*, vol. 521, p. 467, 2015.

[69] D. Drotman, S. Jadhav, M. Karimi, P. DeZonia, and M. T. Tolley, "3D printed soft actuators for a legged robot capable of navigating unstructured terrain," in *2017 IEEE International Conference on Robotics and Automation (ICRA)*, pp. 5532–5538, 2017.

[70] A. D. Marchese and D. Rus, "Design, kinematics, and control of a soft spatial fluidic elastomer manipulator," *The International Journal of Robotics Research*, vol. 35, no. 7, pp. 840–869, 2016.

[71] D. Trivedi, C. D. Rahn, W. M. Kier, and I. D. Walker, "Soft robotics: Biological in-

spiration, state of the art, and future research," *Applied Bionics and Biomechanics*, vol. 5, no. 3, pp. 99–117, 2008.

[72] M. Cianchetti, T. Ranzani, G. Gerboni, T. Nanayakkara, K. Althoefer, P. Dasgupta, and A. Menciassi, "Soft Robotics Technologies to Address Shortcomings in Today's Minimally Invasive Surgery: The STIFF-FLOP Approach," *Soft Robotics*, vol. 1, no. 2, pp. 122–131, 2014.

[73] R. J. Webster III and B. A. Jones, "Design and kinematic modeling of constant curvature continuum robots: A review," *International Journal of Robotics Research*, vol. 29, no. 13, pp. 1661–1683, 2010.

[74] A. Orekhov, C. Abah, and N. Simaan, "Snake-like robots for minimally invasive, single-port, and intraluminal surgeries," *The Encyclopedia of Medical Robotics*, vol. 1, pp. 203–243, 2018.

[75] R. J. Webster, J. S. Kim, N. J. Cowan, G. S. Chirikjian, and A. M. Okamura, "Nonholonomic Modeling of Needle Steering," *The International Journal of Robotics Research*, vol. 25, no. 5-6, pp. 509–525, 2006.

[76] R. J. Webster, J. Memisevic, and A. M. Okamura, "Design considerations for robotic needle steering," in *Proceedings of the 2005 IEEE International Conference on Robotics and Automation*, pp. 3588–3594, 2005.

[77] K. B. Reed, A. Majewicz, V. Kallem, R. Alterovitz, K. Goldberg, N. J. Cowan, and A. M. Okamura, "Robot-assisted needle steering," *IEEE Robotics and Automation Magazine*, vol. 18, no. 4, pp. 35–46, 2011.

[78] R. J. Webster III, J. S. Kim, N. J. Cowan, G. S. Chirikjian, and A. M. Okamura, "Nonholonomic modeling of needle steering," *The International Journal of Robotics Research*, vol. 25, no. 5-6, pp. 509–525, 2006.

[79] M. Khadem, C. Rossa, N. Usmani, R. S. Sloboda, and M. Tavakoli, "Introducing notched flexible needles with increased deflection curvature in soft tissue," in

2016 IEEE International Conference on Advanced Intelligent Mechatronics (AIM), pp. 1186–1191, Institute of Electrical and Electronics Engineers Inc., 2016.

[80] M. Khadem, C. Rossa, N. Usmani, R. S. Sloboda, and M. Tavakoli, "Robotic-Assisted Needle Steering Around Anatomical Obstacles Using Notched Steerable Needles," *IEEE Journal of Biomedical and Health Informatics*, vol. 22, no. 6, pp. 1917–1928, 2018.

[81] H. Su, G. Li, D. C. Rucker, R. J. Webster III, and G. S. Fischer, "A Concentric Tube Continuum Robot with Piezoelectric Actuation for MRI-Guided Closed-Loop Targeting," *Annals of Biomedical Engineering*, vol. 44, no. 10, pp. 2863–2873, 2016.

[82] H. Su, D. C. Cardona, W. Shang, A. Camilo, G. A. Cole, D. C. Rucker, R. J. Webster, and G. S. Fischer, "A MRI-guided concentric tube continuum robot with piezoelectric actuation: a feasibility study," in *2012 IEEE International Conference on Robotics and Automation*, pp. 1939–1945, IEEE, 2012.

[83] C. F. Graetzel, A. Sheehy, and D. P. Noonan, "Robotic bronchoscopy drive mode of the auris monarch platform," in *2019 International Conference on Robotics and Automation (ICRA)*, pp. 3895–3901, IEEE, 2019.

[84] T. Kato, I. Okumura, H. Kose, K. Takagi, and N. Hata, "Tendon-driven continuum robot for neuroendoscopy: validation of extended kinematic mapping for hysteresis operation," *International Journal of Computer Assisted Radiology and Surgery*, vol. 11, no. 4, pp. 589–602, 2016.

[85] E. Amanov, T. D. Nguyen, S. Markmann, F. Imkamp, and J. Burgner-Kahrs, "Toward a Flexible Variable Stiffness Endoport for Single-Site Partial Nephrectomy," *Annals of Biomedical Engineering*, vol. 46, no. 10, pp. 1498–1510, 2018.

[86] W. Jong Yoon, C. A. Velasquez, L. W. White, B. Hannaford, Y. Sang Kim, and T. S. Lendvay, "Preliminary articulable probe designs with RAVEN and challenges: image-guided robotic surgery multitool system," *Journal of Medical Devices*, vol. 8, no. 1, 2014.

[87] Y. Zhang, H. Sun, Y. Jia, D. Huang, R. Li, Z. Mao, Y. Hu, J. Chen, S. Kuang, J. Tang, X. Xiao, and B. Su, "A Continuum Robot with Contractible and Extensible Length for Neurosurgery," in *2018 IEEE 14th International Conference on Control and Automation (ICCA)*, pp. 1150–1155, IEEE Computer Society, 2018.

[88] A. Degani, H. Choset, A. Wolf, and M. A. Zenati, "Highly articulated robotic probe for minimally invasive surgery," in *Proceedings - IEEE International Conference on Robotics and Automation*, vol. 2006, pp. 4167–4172, 2006.

[89] T. Ota, A. Degani, D. Schwartzman, B. Zubiate, J. McGarvey, H. Choset, and M. A. Zenati, "A highly articulated robotic surgical system for minimally invasive surgery," *The Annals of thoracic surgery*, vol. 87, no. 4, pp. 1253–1256, 2009.

[90] N. Simaan, K. Xu, W. Wei, A. Kapoor, P. Kazanzides, R. Taylor, and P. Flint, "Design and Integration of a Telerobotic System for Minimally Invasive Surgery of the Throat," *International Journal of Robotics Research*, vol. 28, no. 9, pp. 1134–1153, 2009.

[91] D. S. Minhas, J. A. Engh, M. M. Fenske, and C. N. Riviere, "Modeling of needle steering via duty-cycled spinning," in *2007 29th Annual International Conference of the IEEE Engineering in Medicine and Biology Society*, pp. 2756–2759, 2007.

[92] S. Okazawa, R. Ebrahimi, J. Chuang, S. E. Salcudean, and R. Rohling, "Hand-held steerable needle device," *IEEE/ASME Transactions on Mechatronics*, vol. 10, no. 3, pp. 285–296, 2005.

[93] P. J. Swaney, J. Burgner, H. B. Gilbert, and R. J. Webster III, "A flexure-based steerable needle: High curvature with reduced tissue damage," *IEEE Transactions on Biomedical Engineering*, vol. 60, no. 4, pp. 906–909, 2013.

[94] N. J. van de Berg, J. Dankelman, and J. J. van den Dobbelsteen, "Design of an actively controlled steerable needle with tendon actuation and FBG-based shape sensing," *Medical Engineering and Physics*, vol. 37, no. 6, pp. 617–622, 2015.

[95] R. J. Roesthuis, N. J. Van De Berg, J. J. Van Den Dobbelsteen, and S. Misra,

"Modeling and steering of a novel actuated-tip needle through a soft-tissue simulant using Fiber Bragg Grating sensors," in *2015 IEEE International Conference on Robotics and Automation (ICRA)*, pp. 2283–2289, Institute of Electrical and Electronics Engineers Inc., 2015.

[96] M. Babaiasl, F. Yang, and J. P. Swensen, "Towards Water-Jet Steerable Needles," in *2018 7th IEEE International Conference on Biomedical Robotics and Biomechatronics (Biorob)*, pp. 601–608, IEEE Computer Society, oct 2018.

[97] S. Y. Ko, L. Frasson, and F. Rodriguez Y Baena, "Closed-loop planar motion control of a steerable probe with a programmable bevel inspired by nature," *IEEE Transactions on Robotics*, vol. 27, no. 5, pp. 970–983, 2011.

[98] C. Burrows, R. Secoli, and F. Rodriguez Y Baena, "Experimental characterisation of a biologically inspired 3D steering needle," in *International Conference on Control, Automation and Systems*, pp. 1252–1257, 2013.

[99] F. Yang, M. Babaiasl, and J. P. Swensen, "Fracture-Directed Steerable Needles," *Journal of Medical Robotics Research*, vol. 04, no. 01, p. 1842002, 2019.

[100] R. J. Webster III, A. M. Okamura, and N. J. Cowan, "Toward active cannulas: Miniature snake-like surgical robots," in *2006 IEEE/RSJ International Conference on Intelligent Robots and Systems*, pp. 2857–2863, 2006.

[101] P. Sears and P. Dupont, "A Steerable Needle Technology Using Curved Concentric Tubes," in *2006 IEEE/RSJ International Conference on Intelligent Robots and Systems*, pp. 2850–2856, 2006.

[102] H. B. Gilbert, D. C. Rucker, and R. J. Webster III, "Concentric Tube Robots: The State of the Art and Future Directions," in *Robotics Research. Springer Tracts in Advanced Robotics, vol 114* (M. Inaba and P. Corke, eds.), pp. 253–269, Cham: Springer International Publishing, 2016.

[103] T. Anor, J. R. Madsen, and P. Dupont, "Algorithms for design of continuum robots

using the concentric tubes approach: A neurosurgical example," in *2011 IEEE International Conference on Robotics and Automation*, pp. 667–673, 2011.

[104] P. J. Swaney, H. B. Gilbert, R. J. Webster III, P. T. Russell 3rd, and K. D. Weaver, "Endonasal Skull Base Tumor Removal Using Concentric Tube Continuum Robots: A Phantom Study," *Journal of neurological surgery. Part B*, vol. 76, no. 2, pp. 145–149, 2015.

[105] R. Wirz, L. G. Torres, P. J. Swaney, H. Gilbert, R. Alterovitz, R. J. Webster III, K. D. Weaver, and P. T. Russell 3rd, "An experimental feasibility study on robotic endonasal telesurgery," *Neurosurgery*, vol. 76, no. 4, pp. 479–484, 2015.

[106] C. R. Mitchell, R. J. Hendrick, R. J. Webster III, and S. D. Herrell, "Toward Improving Transurethral Prostate Surgery: Development and Initial Experiments with a Prototype Concentric Tube Robotic Platform," *Journal of Endourology*, vol. 30, no. 6, pp. 692–696, 2016.

[107] P. J. Swaney, A. W. Mahoney, A. A. Remirez, E. Lamers, B. I. Hartley, R. H. Feins, R. Alterovitz, and R. J. Webster III, "Tendons, Concentric Tubes, and a Bevel Tip: Three Steerable Robots in One Transoral Lung Access System," in *2015 IEEE International Conference on Robotics and Automation (ICRA)*, pp. 5378–5383, may 2015.

[108] S. Amack, M. Rox, J. Mitchell, T. E. Ertop, M. Emerson, A. Kuntz, F. Maldonado, J. Akulian, J. Gafford, R. Alterovitz, and R. J. Webster III, "Design and control of a compact modular robot for transbronchial lung biopsy," in *Medical Imaging 2019: Image-Guided Procedures, Robotic Interventions, and Modeling*, vol. 10951, 2019.

[109] K. E. Riojas, R. J. Hendrick, and R. J. Webster, "Can Elastic Instability Be Beneficial in Concentric Tube Robots?," *IEEE Robotics and Automation Letters*, vol. 3, no. 3, pp. 1624–1630, 2018.

[110] E. Amanov, T.-D. Nguyen, and J. Burgner-Kahrs, "Tendon-driven continuum

robots with extensible sections—A model-based evaluation of path-following motions," *The International Journal of Robotics Research*, 2019.

[111] D. G. Choi, B. J. Yi, and W. K. Kim, "Design of a spring backbone micro endoscope," in *2007 IEEE/RSJ International Conference on Intelligent Robots and Systems*, pp. 1815–1821, 2007.

[112] Y. Kim, S. S. Cheng, and J. P. Desai, "Active Stiffness Tuning of a Spring-Based Continuum Robot for MRI-Guided Neurosurgery," *IEEE Transactions on Robotics*, vol. 34, no. 1, pp. 1–11, 2018.

[113] G. Lim, K. Minami, K. Yamamoto, M. Sugihara, M. Uchiyama, and M. Esashi, "Multi-link active catheter snake-like motion," *Robotica*, vol. 14, no. 5, pp. 499–506, 1996.

[114] M. C. Yip and D. B. Camarillo, "Model-Less Hybrid Position/Force Control: A Minimalist Approach for Continuum Manipulators in Unknown, Constrained Environments," *IEEE Robotics and Automation Letters*, vol. 1, no. 2, pp. 844–851, 2016.

[115] A. Ataollahi, R. Karim, A. S. Fallah, K. Rhode, R. Razavi, L. D. Seneviratne, T. Schaeffter, and K. Althoefer, "Three-degree-of-freedom MR-compatible multi-segment cardiac catheter steering mechanism," *IEEE Transactions on Biomedical Engineering*, vol. 63, no. 11, pp. 2425–2435, 2016.

[116] T. D. Nguyen and J. Burgner-Kahrs, "A tendon-driven continuum robot with extensible sections," in *2015 IEEE/RSJ International Conference on Intelligent Robots and Systems (IROS)*, pp. 2130–2135, Institute of Electrical and Electronics Engineers Inc., 2015.

[117] D. C. Rucker and R. J. Webster III, "Statics and Dynamics of Continuum Robots With General Tendon Routing and External Loading," *IEEE Transactions on Robotics*, vol. 27, no. 6, pp. 1033–1044, 2011.

[118] J. Starke, E. Amanov, M. T. Chikhaoui, and J. Burgner-Kahrs, "On the merits

of helical tendon routing in continuum robots," in *2017 IEEE/RSJ International Conference on Intelligent Robots and Systems (IROS)*, pp. 6470–6476, Institute of Electrical and Electronics Engineers Inc., 2017.

[119] K. Oliver-Butler, J. Till, and C. Rucker, "Continuum Robot Stiffness under External Loads and Prescribed Tendon Displacements," *IEEE Transactions on Robotics*, vol. 35, no. 2, pp. 403–419, 2019.

[120] M. Neumann and J. Burgner-Kahrs, "Considerations for follow-the-leader motion of extensible tendon-driven continuum robots," in *2016 IEEE International Conference on Robotics and Automation (ICRA)*, pp. 917–923, Institute of Electrical and Electronics Engineers Inc., 2016.

[121] B. Kang, R. Kojcev, and E. Sinibaldi, "The First Interlaced Continuum Robot, Devised to Intrinsically Follow the Leader," *PLoS ONE*, vol. 11, no. 2, p. e0150278, 2016.

[122] W. McMahan, B. A. Jones, and I. D. Walker, "Design and implementation of a multi-section continuum robot: Air-Octor," in *2005 IEEE/RSJ International Conference on Intelligent Robots and Systems*, pp. 2578–2585, 2005.

[123] F. Maghooa, A. Stilli, Y. Noh, K. Althoefer, and H. A. Wurdemann, "Tendon and pressure actuation for a bio-inspired manipulator based on an antagonistic principle," in *2015 IEEE International Conference on Robotics and Automation (ICRA)*, pp. 2556–2561, 2015.

[124] J. Lee, E. Go, W. Choi, W. Kim, and K. Cho, "Development of soft continuum manipulator with pneumatic and tendon driven actuations," in *2016 13th International Conference on Ubiquitous Robots and Ambient Intelligence (URAI)*, pp. 377–379, 2016.

[125] A. J. Loeve, D. H. Plettenburg, P. Breedveld, and J. Dankelman, "Endoscope Shaft-Rigidity Control Mechanism: "FORGUIDE"," *IEEE Transactions on Biomedical Engineering*, vol. 59, no. 2, pp. 542–551, 2012.

[126] Y. Kim, S. Cheng, S. Kim, and K. Iagnemma, "A Novel Layer Jamming Mechanism With Tunable Stiffness Capability for Minimally Invasive Surgery," *IEEE Transactions on Robotics*, vol. 29, no. 4, pp. 1031–1042, 2013.

[127] D. C. F. Li, Z. Wang, B. Ouyang, and Y. Liu, "A Reconfigurable Variable Stiffness Manipulator by a Sliding Layer Mechanism," in *2019 International Conference on Robotics and Automation (ICRA)*, pp. 3976–3982, 2019.

[128] Z. Li, J. Feiling, H. Ren, and H. Yu, "A Novel Tele-Operated Flexible Robot Targeted for Minimally Invasive Robotic Surgery," *Engineering*, vol. 1, no. 1, pp. 73–78, 2015.

[129] J. Fras, Y. Noh, M. Macias, H. Wurdemann, and K. Althoefer, "Bio-Inspired Octopus Robot Based on Novel Soft Fluidic Actuator," in *2018 IEEE International Conference on Robotics and Automation (ICRA)*, pp. 1583–1588, 2018.

[130] B. Mosadegh, P. Polygerinos, C. Keplinger, S. Wennstedt, R. F. Shepherd, U. Gupta, J. Shim, K. Bertoldi, C. J. Walsh, and G. M. Whitesides, "Pneumatic Networks for Soft Robotics that Actuate Rapidly," *Advanced Functional Materials*, vol. 24, no. 15, pp. 2163–2170, 2014.

[131] A. D. Marchese, R. K. Katzschmann, and D. Rus, "A Recipe for Soft Fluidic Elastomer Robots," *Soft Robotics*, vol. 2, no. 1, pp. 7–25, 2015.

[132] B. Tondu, V. Boitier, and P. Lopez, "Naturally compliant robot-arms actuated by McKibben artificial muscles," in *Proceedings of IEEE International Conference on Systems, Man and Cybernetics*, vol. 3, pp. 2635–2640 vol. 3, 1994.

[133] S. Obiajulu, E. T. Roche, F. A. Pigula, and C. J. Walsh, "Soft pneumatic artificial muscles with low threshold pressures for a cardiac compression device," in *Proceedings of the ASME 2013 International Design Engineering Technical Conferences & Computers and Information in Engineering Conference IDETC/CIE*, Massachusetts Institute of Technology, 2013.

[134] F. Daerden and D. Lefeber, "Pneumatic artificial muscles: actuators for robotics

and automation," *European journal of mechanical and environmental engineering*, vol. 47, no. 1, pp. 11–21, 2002.

[135] F. Connolly, P. Polygerinos, C. J. Walsh, and K. Bertoldi, "Mechanical Programming of Soft Actuators by Varying Fiber Angle," *Soft Robotics*, vol. 2, no. 1, pp. 26–32, 2015.

[136] J. Hughes, U. Culha, F. Giardina, F. Guenther, A. Rosendo, and F. Iida, "Soft manipulators and grippers: a review," *Frontiers in Robotics and AI*, vol. 3, p. 69, 2016.

[137] I. De Falco, M. Cianchetti, and A. Menciassi, "A soft multi-module manipulator with variable stiffness for minimally invasive surgery," *Bioinspiration & Biomimetics*, vol. 12, no. 5, p. 56008, 2017.

[138] R. Caprara, K. L. Obstein, G. Scozzarro, C. Di Natali, M. Beccani, D. R. Morgan, and P. Valdastri, "A platform for gastric cancer screening in low-and middle-income countries," *IEEE Transactions on Biomedical Engineering*, vol. 62, no. 5, pp. 1324–1332, 2014.

[139] F. Campisano, A. A. Remirez, S. Caló, J. H. Chandler, K. L. Obstein, R. J. Webster, and P. Valdastri, "Online disturbance estimation for improving kinematic accuracy in continuum manipulators," *IEEE Robotics and Automation Letters*, vol. 5, no. 2, pp. 2642–2649, 2020.

[140] S. Calò, J. Chandler, F. Campisano, K. L. Obstein, and P. Valdastri, "A compression valve for sanitary control of fluid driven actuators," *IEEE/ASME Transactions on Mechatronics*, 2019.

[141] F. Campisano, F. Gramuglia, I. R. Dawson, C. T. Lyne, M. L. Izmaylov, S. Misra, E. De Momi, D. R. Morgan, K. L. Obstein, and P. Valdastri, "Gastric cancer screening in low-income countries: System design, fabrication, and analysis for an ultralow-cost endoscopy procedure," *IEEE robotics & automation magazine*, vol. 24, no. 2, pp. 73–81, 2017.

[142] T. Ranzani, G. Gerboni, M. Cianchetti, and A. Menciassi, "A bioinspired soft manipulator for minimally invasive surgery," *Bioinspiration & biomimetics*, vol. 10, no. 3, p. 35008, 2015.

[143] N. Garbin, L. Wang, J. H. Chandler, K. L. Obstein, N. Simaan, and P. Valdastri, "A disposable continuum endoscope using piston-driven parallel bellow actuator," in *2018 International Symposium on Medical Robotics (ISMR)*, pp. 1–6, IEEE, 2018.

[144] N. Garbin, L. Wang, J. H. Chandler, K. L. Obstein, N. Simaan, and P. Valdastri, "Dual-continuum design approach for intuitive and low-cost upper gastrointestinal endoscopy," *IEEE Transactions on Biomedical Engineering*, vol. 66, no. 7, pp. 1963–1974, 2018.

[145] K. Ikuta, H. Ichikawa, K. Suzuki, and D. Yajima, "Multi-degree of freedom hydraulic pressure driven safety active catheter," in *Proceedings 2006 IEEE International Conference on Robotics and Automation (ICRA)*, pp. 4161–4166, 2006.

[146] Y. Inoue and K. Ikuta, "Hydraulic driven active catheters with optical bending sensor," in *2016 IEEE 29th international conference on micro electro mechanical systems (MEMS)*, pp. 383–386, IEEE, 2016.

[147] B. Gorissen, W. Vincentie, F. Al-Bender, D. Reynaerts, and M. De Volder, "Modeling and bonding-free fabrication of flexible fluidic microactuators with a bending motion," *Journal of Micromechanics and Microengineering*, vol. 23, no. 4, p. 45012, 2013.

[148] G. M. Whitesides, "Soft Robotics," *Angewandte Chemie International Edition*, vol. 57, no. 16, pp. 4258–4273, 2018.

[149] R. F. Shepherd, A. A. Stokes, R. M. D. Nunes, and G. M. Whitesides, "Soft Machines That are Resistant to Puncture and That Self Seal," *Advanced Materials*, vol. 25, no. 46, pp. 6709–6713, 2013.

[150] L. H. Blumenschein, N. S. Usevitch, B. H. Do, E. W. Hawkes, and A. M. Okamura,

"Helical actuation on a soft inflated robot body," in *2018 IEEE International Conference on Soft Robotics (RoboSoft)*, pp. 245–252, 2018.

[151] R. Yahiaoui, R. Zeggari, J. Malapert, and J.-F. Manceau, "A MEMS-based pneumatic micro-conveyor for planar micromanipulation," *Mechatronics*, vol. 22, no. 5, pp. 515–521, 2012.

[152] E. W. Hawkes, L. H. Blumenschein, J. D. Greer, and A. M. Okamura, "A soft robot that navigates its environment through growth," *Science Robotics*, vol. 2, no. 8, p. eaan3028, 2017.

[153] A. A. Calderón, J. C. Ugalde, J. C. Zagal, and N. O. Pérez-Arancibia, "Design, fabrication and control of a multi-material-multi-actuator soft robot inspired by burrowing worms," in *2016 IEEE International Conference on Robotics and Biomimetics (ROBIO)*, pp. 31–38, 2016.

[154] N. R. Sinatra, T. Ranzani, J. J. Vlassak, K. K. Parker, and R. J. Wood, "Nanofiber-reinforced soft fluidic micro-actuators," *Journal of Micromechanics and Microengineering*, vol. 28, no. 8, p. 84002, 2018.

[155] J. D. Greer, T. K. Morimoto, A. M. Okamura, and E. W. Hawkes, "Series Pneumatic Artificial Muscles (sPAMs) and Application to a Soft Continuum Robot," in *2017 IEEE International Conference on Robotics and Automation (ICRA)*, pp. 5503–5510, 2017.

[156] D. Yang, B. Mosadegh, A. Ainla, B. Lee, F. Khashai, Z. Suo, K. Bertoldi, and G. M. Whitesides, "Buckling of Elastomeric Beams Enables Actuation of Soft Machines," *Advanced Materials*, vol. 27, no. 41, pp. 6323–6327, 2015.

[157] Y. Haga, Y. Muyari, T. Mineta, T. Matsunaga, H. Akahori, and M. Esashi, "Small diameter hydraulic active bending catheter using laser processed super elastic alloy and silicone rubber tube," in *2005 3rd IEEE/EMBS Special Topic Conference on Microtechnology in Medicine and Biology*, pp. 245–248, 2005.

[158] A. Ali, D. H. Plettenburg, and P. Breedveld, "Steerable Catheters in Cardiology:

Classifying Steerability and Assessing Future Challenges," *IEEE Transactions on Biomedical Engineering*, vol. 63, no. 4, pp. 679–693, 2016.

[159] M. W. Gifari, H. Naghibi, S. Stramigioli, and M. Abayazid, "A review on recent advances in soft surgical robots for endoscopic applications," *The International Journal of Medical Robotics and Computer Assisted Surgery*, vol. 15, no. 5, pp. e2010–e2010, 2019.

[160] F. Ilievski, A. D. Mazzeo, R. F. Shepherd, X. Chen, and G. M. Whitesides, "Soft Robotics for Chemists," *Angewandte Chemie International Edition*, vol. 50, no. 8, pp. 1890–1895, 2011.

[161] K. Suzumori, S. Iikura, and H. Tanaka, "Applying a flexible microactuator to robotic mechanisms," *IEEE Control Systems Magazine*, vol. 12, no. 1, pp. 21–27, 1992.

[162] S. A. Huettel, A. W. Song, and G. McCarthy, *Functional magnetic resonance imaging*, vol. 1. Sinauer Associates Sunderland, MA, 2004.

[163] J. Sikorski, A. Denasi, G. Bucchi, S. Scheggi, and S. Misra, "Vision-Based 3-D Control of Magnetically Actuated Catheter Using BigMag—An Array of Mobile Electromagnetic Coils," *IEEE/ASME Transactions on Mechatronics*, vol. 24, no. 2, pp. 505–516, 2019.

[164] A. J. Petruska and B. J. Nelson, "Minimum bounds on the number of electromagnets required for remote magnetic manipulation," *IEEE Transactions on Robotics*, vol. 31, no. 3, pp. 714–722, 2015.

[165] C. Chautems, A. Tonazzini, Q. Boehler, S. H. Jeong, D. Floreano, and B. J. Nelson, "Magnetic Continuum Device with Variable Stiffness for Minimally Invasive Surgery," *Advanced Intelligent Systems*, p. 1900086, 2019.

[166] C. Chautems, A. Tonazzini, D. Floreano, and B. J. Nelson, "A variable stiffness catheter controlled with an external magnetic field," in *2017 IEEE/RSJ International Conference on Intelligent Robots and Systems (IROS)*, pp. 181–186, 2017.

[167] S. Jeon, A. K. Hoshiar, K. Kim, S. Lee, E. Kim, S. Lee, J.-y. Kim, B. J. Nelson, H.-J. Cha, B.-J. Yi, and H. Choi, "A Magnetically Controlled Soft Microrobot Steering a Guidewire in a Three-Dimensional Phantom Vascular Network," *Soft Robotics*, vol. 6, no. 1, pp. 54–68, 2018.

[168] C. Chautems and B. J. Nelson, "The tethered magnet: Force and 5-DOF pose control for cardiac ablation," in *2017 IEEE International Conference on Robotics and Automation (ICRA)*, pp. 4837–4842, IEEE, 2017.

[169] Boston Scientific, "Polaris X. Steerable Diagnostic Catheter," 2015.

[170] B. L. Gray, "A review of magnetic composite polymers applied to microfluidic devices," *Journal of the Electrochemical Society*, vol. 161, no. 2, pp. B3173–B3183, 2014.

[171] T. Xu, J. Zhang, M. Salehizadeh, O. Onaizah, and E. Diller, "Millimeter-scale flexible robots with programmable three-dimensional magnetization and motions," *Science Robotics*, vol. 4, no. 29, p. eaav4494, 2019.

[172] C. Liu, *Foundations of MEMS*. Upper Saddle River, NJ, USA: Prentice Hall Press, 2nd ed., 2011.

[173] B. J. Nelson, I. K. Kaliakatsos, and J. J. Abbott, "Microrobots for Minimally Invasive Medicine," *Annual Review of Biomedical Engineering*, vol. 12, no. 1, pp. 55–85, 2010.

[174] J. J. Abbott, K. E. Peyer, M. C. Lagomarsino, L. Zhang, L. Dong, I. K. Kaliakatsos, and B. J. Nelson, "How Should Microrobots Swim?," *The International Journal of Robotics Research*, vol. 28, no. 11-12, pp. 1434–1447, 2009.

[175] J. Kim, M. J. Kim, J. Yoo, and S. Kim, "Novel Motion Modes for 2-D Locomotion of a Microrobot," *IEEE Transactions on Magnetics*, vol. 50, no. 11, pp. 1–5, 2014.

[176] T. Xu, G. Hwang, N. Andreff, and S. Régnier, "Characterization of three-

dimensional steering for helical swimmers," in *2014 IEEE International Conference on Robotics and Automation (ICRA)*, pp. 4686–4691, 2014.

[177] K. B. Yesin, K. Vollmers, and B. J. Nelson, "Modeling and Control of Untethered Biomicrorobots in a Fluidic Environment Using Electromagnetic Fields," *The International Journal of Robotics Research*, vol. 25, no. 5-6, pp. 527–536, 2006.

[178] C. Hu, C. Tercero, S. Ikeda, T. Fukuda, F. Arai, and M. Negoro, "Modeling and design of magnetic sugar particles manipulation system for fabrication of vascular scaffold," in *2011 IEEE/RSJ International Conference on Intelligent Robots and Systems*, pp. 439–444, 2011.

[179] G. Go, H. Choi, S. Jeong, C. Lee, S. Y. Ko, J. Park, and S. Park, "Electromagnetic Navigation System Using Simple Coil Structure (4 Coils) for 3-D Locomotive Microrobot," *IEEE Transactions on Magnetics*, vol. 51, no. 4, pp. 1–7, 2015.

[180] E. Diller, J. Giltinan, G. Z. Lum, Z. Ye, and M. Sitti, "Six-degree-of-freedom magnetic actuation for wireless microrobotics," *The International Journal of Robotics Research*, vol. 35, no. 1-3, pp. 114–128, 2015.

[181] B. E. Kratochvil, M. P. Kummer, S. Erni, R. Borer, D. R. Frutiger, S. Schurle, and B. J. Nelson, "MiniMag: a hemispherical electromagnetic system for 5-DOF wireless micromanipulation," in *Experiemental Robotics. Springer Tracts in Advanced Robotics, vol 79* (O. Khatib, V. Kumar, and G. Sukjatme, eds.), pp. 317–329, Berlin: Springer, 2014.

[182] M. P. Kummer, J. J. Abbott, B. E. Kratochvil, R. Borer, A. Sengul, and B. J. Nelson, "OctoMag: An Electromagnetic System for 5-DOF Wireless Micromanipulation," *IEEE Transactions on Robotics*, vol. 26, no. 6, pp. 1006–1017, 2010.

[183] S. Salmanipour and E. Diller, "Eight-Degrees-of-Freedom Remote Actuation of Small Magnetic Mechanisms," in *2018 IEEE International Conference on Robotics and Automation (ICRA)*, pp. 3608–3613, 2018.

[184] J. Sikorski, I. Dawson, A. Denasi, E. E. G. Hekman, and S. Misra, "Introducing

BigMag — A novel system for 3D magnetic actuation of flexible surgical manipulators," in *2017 IEEE International Conference on Robotics and Automation (ICRA)*, pp. 3594–3599, 2017.

[185] O. Youssefi and E. Diller, "Contactless Robotic Micromanipulation in Air Using a Magneto-Acoustic System," *IEEE Robotics and Automation Letters*, vol. 4, no. 2, pp. 1580–1586, 2019.

[186] T. Thomas, V. Kalpathy Venkiteswaran, G. Ananthasuresh, and S. Misra, "A monolithic compliant continuum manipulator: a proof-of-concept study," *Journal of Mechanisms and Robotics*, pp. 1–11, 2020.

[187] Y. Kim, G. A. Parada, S. Liu, and X. Zhao, "Ferromagnetic soft continuum robots," *Science Robotics*, vol. 4, no. 33, p. eaax7329, 2019.

[188] P. Lloyd, A. K. Hoshiar, T. da Veiga, A. Attanasio, N. Marahrens, J. H. Chandler, and P. Valdastri, "A learnt approach for the design of magnetically actuated shape forming soft tentacle robots," *IEEE Robotics and Automation Letters*, vol. 5, no. 3, pp. 3937–3944, 2020.

[189] M. Kaya, U. Sakthivel, I. S. Khalil, and S. Misra, "Development of a coil driver for magnetic manipulation systems," *IEEE Magnetics Letters*, vol. 10, pp. 1–5, 2019.

[190] P. Ryan and E. Diller, "Magnetic actuation for full dexterity microrobotic control using rotating permanent magnets," *IEEE Transactions on Robotics*, vol. 33, no. 6, pp. 1398–1409, 2017.

[191] S. Yim and M. Sitti, "Design and Rolling Locomotion of a Magnetically Actuated Soft Capsule Endoscope," *IEEE Transactions on Robotics*, vol. 28, no. 1, pp. 183–194, 2012.

[192] P. Valdastri, C. Quaglia, E. Susilo, A. Menciassi, P. Dario, C. N. Ho, G. Anhoeck, and M. O. Schurr, "Wireless therapeutic endoscopic capsule: in vivo experiment," *Endoscopy*, vol. 40, no. 12, pp. 979–982, 2008.

[193] P. Valdastri, G. Ciuti, A. Verbeni, A. Menciassi, P. Dario, A. Arezzo, and M. Morino, "Magnetic air capsule robotic system: proof of concept of a novel approach for painless colonoscopy," *Surgical endoscopy*, vol. 26, no. 5, pp. 1238–1246, 2012.

[194] L. B. Kratchman, T. L. Bruns, J. J. Abbott, and R. J. Webster, "Guiding Elastic Rods With a Robot-Manipulated Magnet for Medical Applications," *IEEE Transactions on Robotics*, vol. 33, no. 1, pp. 227–233, 2017.

[195] D. Filgueiras-Rama, A. Estrada, J. Shachar, S. Castrejón, D. Doiny, M. Ortega, E. Gang, and J. L. Merino, "Remote magnetic navigation for accurate, real-time catheter positioning and ablation in cardiac electrophysiology procedures," *JoVE (Journal of Visualized Experiments)*, no. 74, p. e3658, 2013.

[196] M. Vonthron, V. Lalande, G. Bringout, C. Tremblay, and S. Martel, "A MRI-based integrated platform for the navigation of micro-devices and microrobots," in *2011 IEEE/RSJ International Conference on Intelligent Robots and Systems*, pp. 1285–1290, IEEE, 2011.

[197] J.-B. Mathieu, G. Beaudoin, and S. Martel, "Method of propulsion of a ferromagnetic core in the cardiovascular system through magnetic gradients generated by an MRI system," *IEEE Transactions on Biomedical Engineering*, vol. 53, no. 2, pp. 292–299, 2006.

[198] S. Tamaz, R. Gourdeau, A. Chanu, J.-B. Mathieu, and S. Martel, "Real-time MRI-based control of a ferromagnetic core for endovascular navigation," *IEEE Transactions on Biomedical Engineering*, vol. 55, no. 7, pp. 1854–1863, 2008.

[199] S. Martel, O. Felfoul, J.-B. Mathieu, A. Chanu, S. Tamaz, M. Mohammadi, M. Mankiewicz, and N. Tabatabaei, "MRI-based medical nanorobotic platform for the control of magnetic nanoparticles and flagellated bacteria for target interventions in human capillaries," *The International journal of robotics research*, vol. 28, no. 9, pp. 1169–1182, 2009.

[200] A. Azizi, C. C. Tremblay, K. Gagné, and S. Martel, "Using the fringe field of a clinical MRI scanner enables robotic navigation of tethered instruments in deeper vascular regions," *Science Robotics*, vol. 4, no. 36, p. eaax7342, 2019.

[201] J. C. Norton, P. R. Slawinski, H. S. Lay, J. W. Martin, B. F. Cox, G. Cummins, M. P. Y. Desmulliez, R. E. Clutton, K. L. Obstein, and S. Cochran, "Intelligent magnetic manipulation for gastrointestinal ultrasound," *Science Robotics*, 2019.

[202] D. Son, S. Yim, and M. Sitti, "A 5-D localization method for a magnetically manipulated untethered robot using a 2-D array of Hall-effect sensors," *IEEE/ASME Transactions on Mechatronics*, vol. 21, no. 2, pp. 708–716, 2015.

[203] T. K. Morimoto and A. M. Okamura, "Design of 3-d printed concentric tube robots," *IEEE Transactions on Robotics*, vol. 32, no. 6, pp. 1419–1430, 2016.

[204] H. B. Gilbert and R. J. Webster III, "Rapid, reliable shape setting of superelastic nitinol for prototyping robots," *IEEE robotics and automation letters*, vol. 1, no. 1, p. 98, 2016.

[205] T. J. Wallin, J. Pikul, and R. F. Shepherd, "3D printing of soft robotic systems," *Nature Reviews Materials*, vol. 3, no. 6, pp. 84–100, 2018.

[206] R. L. Truby and J. A. Lewis, "Printing soft matter in three dimensions," *Nature*, vol. 540, p. 371, 2016.

[207] B. N. Peele, T. J. Wallin, H. Zhao, and R. F. Shepherd, "3D printing antagonistic systems of artificial muscle using projection stereolithography," *Bioinspiration & biomimetics*, vol. 10, no. 5, p. 55003, 2015.

[208] J. A. Lewis, "Direct Ink Writing of 3D Functional Materials," *Advanced Functional Materials*, vol. 16, pp. 2193–2204, nov 2006.

[209] M. A. Skylar-Scott, J. Mueller, C. W. Visser, and J. A. Lewis, "Voxelated soft matter via multimaterial multinozzle 3D printing," *Nature*, vol. 575, no. 7782, pp. 330–335, 2019.

[210] R. L. Truby, M. Wehner, A. K. Grosskopf, D. M. Vogt, S. G. M. Uzel, R. J. Wood, and J. A. Lewis, "Soft somatosensitive actuators via embedded 3D printing," *Advanced Materials*, vol. 30, no. 15, p. 1706383, 2018.

[211] N. J. Wilkinson, M. Lukic-Mann, M. P. Shuttleworth, R. W. Kay, and R. A. Harris, "Aerosol Jet Printing for the Manufacture of Soft Robotic Devices," in *2019 2nd IEEE International Conference on Soft Robotics (RoboSoft)*, pp. 496–501, IEEE, 2019.

[212] C. Chautems, S. Lyttle, Q. Boehler, and B. J. Nelson, "Design and Evaluation of a Steerable Magnetic Sheath for Cardiac Ablations," *IEEE Robotics and Automation Letters*, vol. 3, no. 3, pp. 2123–2128, 2018.

[213] A. Kafash Hoshiar, S. Jeon, K. Kim, S. Lee, J.-Y. Kim, and H. Choi, "Steering Algorithm for a Flexible Microrobot to Enhance Guidewire Control in a Coronary Angioplasty Application," *Micromachines*, vol. 9, no. 12, p. 617, 2018.

[214] U.S. Food and Drug Administration (FDA), "Class 2 medical device recalls: Cronus endovascular guidewires," 2004.

[215] R. Zhao, Y. Kim, S. A. Chester, P. Sharma, and X. Zhao, "Mechanics of hard-magnetic soft materials," *Journal of the Mechanics and Physics of Solids*, vol. 124, pp. 244–263, 2019.

[216] G. Z. Lum, Z. Ye, X. Dong, H. Marvi, O. Erin, W. Hu, and M. Sitti, "Shape-programmable magnetic soft matter," *Proceedings of the National Academy of Sciences*, vol. 113, no. 41, pp. E6007–E6015, 2016.

[217] E. Diller, J. Zhuang, G. Zhan Lum, M. R. Edwards, and M. Sitti, "Continuously distributed magnetization profile for millimeter-scale elastomeric undulatory swimming," *Applied Physics Letters*, vol. 104, no. 17, p. 174101, 2014.

[218] Z. Ren, W. Hu, X. Dong, and M. Sitti, "Multi-functional soft-bodied jellyfish-like swimming," *Nature Communications*, vol. 10, no. 1, p. 2703, 2019.

[219] J. Kim, S. E. Chung, S.-E. Choi, H. Lee, J. Kim, and S. Kwon, "Programming magnetic anisotropy in polymeric microactuators," *Nature Materials*, vol. 10, no. 10, pp. 747–752, 2011.

[220] H.-W. Huang, M. S. Sakar, A. J. Petruska, S. Pané, and B. J. Nelson, "Soft micromachines with programmable motility and morphology," *Nature Communications*, vol. 7, no. 1, p. 12263, 2016.

[221] Y. Kim, H. Yuk, R. Zhao, S. A. Chester, and X. Zhao, "Printing ferromagnetic domains for untethered fast-transforming soft materials," *Nature*, vol. 558, no. 7709, pp. 274–279, 2018.

[222] B. Siciliano, L. Sciavicco, L. Villani, and G. Oriolo, *Robotics: Modelling, Planning and Control*. Springer Publishing Company, Incorporated, 2010.

[223] M. T. Chikhaoui and J. Burgner-Kahrs, "Control of Continuum Robots for Medical Applications : State of the Art," in *2018 16th International Conference on New Actuators*, 2018.

[224] D. C. Rucker, B. A. Jones, and R. J. Webster, "A geometrically exact model for externally loaded concentric-tube continuum robots," *IEEE Transactions on Robotics*, vol. 26, no. 5, pp. 769–780, 2010.

[225] J. Edelmann, A. J. Petruska, and B. J. Nelson, "Magnetic control of continuum devices," *International Journal of Robotics Research*, vol. 36, no. 1, pp. 68–85, 2017.

[226] T. Bretl and Z. McCarthy, "Quasi-static manipulation of a Kirchhoff elastic rod based on a geometric analysis of equilibrium configurations," *International Journal of Robotics Research*, vol. 33, no. 1, pp. 48–68, 2014.

[227] V. K. Venkiteswaran, J. Sikorski, and S. Misra, "Shape and contact force estimation of continuum manipulators using pseudo rigid body models," *Mechanism and Machine Theory*, vol. 139, pp. 34–45, 2019.

[228] J. Jung, R. S. Penning, N. J. Ferrier, and M. R. Zinn, "A modeling approach for continuum robotic manipulators: Effects of nonlinear internal device friction," *IEEE International Conference on Intelligent Robots and Systems*, pp. 5139–5146, 2011.

[229] S. Grazioso, G. Di Gironimo, and B. Siciliano, "A Geometrically Exact Model for Soft Continuum Robots: The Finite Element Deformation Space Formulation," *Soft Robotics*, vol. 6, no. 6, pp. 790–811, 2019.

[230] V. Falkenhahn, T. Mahl, A. Hildebrandt, R. Neumann, and O. Sawodny, "Dynamic Modeling of Bellows-Actuated Continuum Robots Using the Euler-Lagrange Formalism," *IEEE Transactions on Robotics*, vol. 31, no. 6, pp. 1483–1496, 2015.

[231] W. S. Rone and P. Ben-Tzvi, "Mechanics modeling of multisegment rod-driven continuum robots," *Journal of Mechanisms and Robotics*, vol. 6, no. 4, 2014.

[232] R. J. Roesthuis and S. Misra, "Steering of Multisegment Continuum Manipulators Using Rigid-Link Modeling and FBG-Based Shape Sensing," *IEEE Transactions on Robotics*, vol. 32, no. 2, pp. 372–382, 2016.

[233] G. Runge, M. Wiese, L. Gunther, and A. Raatz, "A framework for the kinematic modeling of soft material robots combining finite element analysis and piecewise constant curvature kinematics," in *2017 3rd International Conference on Control, Automation and Robotics (ICCAR)*, pp. 7–14, 2017.

[234] P. S. Gonthina, A. D. Kapadia, I. S. Godage, and I. D. Walker, "Modeling variable curvature parallel continuum robots using euler curves," in *2019 International Conference on Robotics and Automation (ICRA)*, pp. 1679–1685, IEEE, 2019.

[235] J. Till, V. Aloi, and C. Rucker, "Real-time dynamics of soft and continuum robots based on cosserat rod models," *The International Journal of Robotics Research*, vol. 38, no. 6, pp. 723–746, 2019.

[236] C. Della Santina, A. Bicchi, and D. Rus, "On an improved state parametrization for

soft robots with piecewise constant curvature and its use in model based control," *IEEE Robotics and Automation Letters*, vol. 5, no. 2, pp. 1001–1008, 2020.

[237] C. Della Santina and D. Rus, "Control oriented modeling of soft robots: the polynomial curvature case," *IEEE Robotics and Automation Letters*, vol. 5, no. 2, pp. 290–298, 2020.

[238] W. S. Rone and P. Ben-Tzvi, "Continuum robot dynamics utilizing the principle of virtual power," *IEEE Transactions on Robotics*, vol. 30, no. 1, pp. 275–287, 2014.

[239] L. Barducci, G. Pittiglio, J. C. Norton, K. L. Obstein, and P. Valdastri, "Adaptive Dynamic Control for Magnetically Actuated Medical Robots," *IEEE Robotics and Automation Letters*, vol. 4, no. 4, pp. 3633–3640, 2019.

[240] A. Isidori, *Nonlinear control systems*. Springer Science & Business Media, 2013.

[241] M. N. Boushaki, C. Liu, and P. Poignet, "Task-space position control of concentric-tube robot with inaccurate kinematics using approximate Jacobian," in *2014 IEEE International Conference on Robotics and Automation (ICRA)*, pp. 5877–5882, IEEE, 2014.

[242] M. T. Chikhaoui, J. Granna, J. Starke, and J. Burgner-Kahrs, "Toward motion coordination control and design optimization for dual-arm concentric tube continuum robots," *IEEE Robotics and Automation Letters*, vol. 3, no. 3, pp. 1793–1800, 2018.

[243] T. Mahl, A. Hildebrandt, and O. Sawodny, "A variable curvature continuum kinematics for kinematic control of the bionic handling assistant," *IEEE Transactions on Robotics*, vol. 30, no. 4, pp. 935–949, 2014.

[244] P. Sears and P. E. Dupont, "Inverse kinematics of concentric tube steerable needles," in *Proceedings 2007 IEEE International Conference on Robotics and Automation*, pp. 1887–1892, 2007.

[245] T. G. Thuruthel, E. Falotico, M. Manti, A. Pratesi, M. Cianchetti, and C. Laschi,

"Learning closed loop kinematic controllers for continuum manipulators in unstructured environments," *Soft Robotics*, vol. 4, no. 3, pp. 285–296, 2017.

[246] H. Jiang, Z. Wang, X. Liu, X. Chen, Y. Jin, X. You, and X. Chen, "A two-level approach for solving the inverse kinematics of an extensible soft arm considering viscoelastic behavior," in *2017 IEEE International Conference on Robotics and Automation (ICRA)*, pp. 6127–6133, IEEE, 2017.

[247] A. Melingui, O. Lakhal, B. Daachi, J. B. Mbede, and R. Merzouki, "Adaptive neural network control of a compact bionic handling arm," *IEEE/ASME Transactions on Mechatronics*, vol. 20, no. 6, pp. 2862–2875, 2015.

[248] W. Xu, J. Chen, H. Y. Lau, and H. Ren, "Data-driven methods towards learning the highly nonlinear inverse kinematics of tendon-driven surgical manipulators," *International Journal of Medical Robotics and Computer Assisted Surgery*, vol. 13, no. 3, pp. 1–11, 2017.

[249] M. Li, R. Kang, D. T. Branson, and J. S. Dai, "Model-free control for continuum robots based on an adaptive kalman filter," *IEEE/ASME Transactions on Mechatronics*, vol. 23, no. 1, pp. 286–297, 2018.

[250] H. Wang, B. Yang, Y. Liu, W. Chen, X. Liang, and R. Pfeifer, "Visual Servoing of Soft Robot Manipulator in Constrained Environments With an Adaptive Controller," *IEEE/ASME Transactions on Mechatronics*, vol. 22, no. 1, pp. 41–50, 2017.

[251] C. Kim, S. C. Ryu, and P. E. Dupont, "Real-time adaptive kinematic model estimation of concentric tube robots," in *2015 IEEE/RSJ International Conference on Intelligent Robots and Systems (IROS)*, pp. 3214–3219, IEEE, 2015.

[252] G. Fagogenis, C. Bergeles, and P. E. Dupont, "Adaptive nonparametric kinematic modeling of concentric tube robots," in *2016 IEEE/RSJ International Conference on Intelligent Robots and Systems (IROS)*, pp. 4324–4329, IEEE, 2016.

[253] M. Mahvash and P. E. Dupont, "Stiffness control of surgical continuum manipulators," *IEEE Transactions on Robotics*, vol. 27, no. 2, pp. 334–345, 2011.

[254] A. Bajo and N. Simaan, "Hybrid motion/force control of multi-backbone continuum robots," *International Journal of Robotics Research*, vol. 35, no. 4, pp. 422–434, 2016.

[255] D. C. Rucker and R. J. Webster, "Deflection-based force sensing for continuum robots: A probabilistic approach," *IEEE International Conference on Intelligent Robots and Systems*, pp. 3764–3769, 2011.

[256] K. Xu and N. Simaan, "Intrinsic wrench estimation and its performance index for multisegment continuum robots," *IEEE Transactions on Robotics*, vol. 26, no. 3, pp. 555–561, 2010.

[257] R. E. Goldman, A. Bajo, and N. Simaan, "Compliant motion control for multisegment continuum robots with actuation force sensing," *IEEE Transactions on Robotics*, vol. 30, no. 4, pp. 890–902, 2014.

[258] V. Falkenhahn, A. Hildebrandt, R. Neumann, and O. Sawodny, "Dynamic Control of the Bionic Handling Assistant," *IEEE/ASME Transactions on Mechatronics*, vol. 22, no. 1, pp. 6–17, 2017.

[259] T. George Thuruthel, Y. Ansari, E. Falotico, and C. Laschi, "Control Strategies for Soft Robotic Manipulators: A Survey," *Soft Robotics*, vol. 5, no. 2, pp. 149–163, 2018.

[260] R. J. Roesthuis, M. Kemp, J. J. van den Dobbelsteen, and S. Misra, "Three-Dimensional Needle Shape Reconstruction Using an Array of Fiber Bragg Grating Sensors," *IEEE/ASME Transactions on Mechatronics*, vol. 19, no. 4, pp. 1115–1126, 2014.

[261] Y.-L. Park, S. Elayaperumal, B. Daniel, S. C. Ryu, M. Shin, J. Savall, R. J. Black, B. Moslehi, and M. R. Cutkosky, "Real-Time Estimation of 3-D Needle Shape and Deflection for MRI-Guided Interventions," *IEEE/ASME transactions on mecha-*

tronics : a joint publication of the IEEE Industrial Electronics Society and the ASME Dynamic Systems and Control Division, vol. 15, no. 6, pp. 906–915, 2010.

[262] K. Henken, D. Van Gerwen, J. Dankelman, and J. Van Den Dobbelsteen, "Accuracy of needle position measurements using fiber Bragg gratings," *Minimally Invasive Therapy & Allied Technologies*, vol. 21, no. 6, pp. 408–414, 2012.

[263] K. Mandal, F. Parent, S. Martel, R. Kashyap, and S. Kadoury, "Vessel-based registration of an optical shape sensing catheter for MR navigation," *International Journal of Computer Assisted Radiology and Surgery*, vol. 11, no. 6, pp. 1025–1034, 2016.

[264] C. Shi, S. Giannarou, S. Lee, and G. Yang, "Simultaneous catheter and environment modeling for Trans-catheter Aortic Valve Implantation," in *2014 IEEE/RSJ International Conference on Intelligent Robots and Systems*, pp. 2024–2029, 2014.

[265] F. Khan, A. Denasi, D. Barrera, J. Madrigal, S. Sales, and S. Misra, "Multi-Core Optical Fibers With Bragg Gratings as Shape Sensor for Flexible Medical Instruments," *IEEE Sensors Journal*, vol. 19, no. 14, pp. 5878–5884, 2019.

[266] X. Yi, J. Qian, L. Shen, Y. Zhang, and Z. Zhang, "An Innovative 3D Colonoscope Shape Sensing Sensor Based on FBG Sensor Array," in *2007 International Conference on Information Acquisition*, pp. 227–232, 2007.

[267] X. Yi, J. Qian, Y. Zhang, Z. Zhang, and L. Shen, "3-D Shape Display of Intelligent Colonoscope Based on FBG Sensor Array and Binocular Vision," in *2007 IEEE/ICME International Conference on Complex Medical Engineering*, pp. 14–19, 2007.

[268] T. Li, C. Shi, and H. Ren, "Three-Dimensional Catheter Distal Force Sensing for Cardiac Ablation Based on Fiber Bragg Grating," *IEEE/ASME Transactions on Mechatronics*, vol. 23, no. 5, pp. 2316–2327, 2018.

[269] R. Xu, A. Yurkewich, and R. V. Patel, "Shape sensing for torsionally compliant

concentric-tube robots," in *Proc. SPIE 9702, Optical Fibers and Sensors for Medical Diagnostics and Treatment Applications XVI*, vol. 9702, 2016.

[270] R. Xu, A. Yurkewich, and R. V. Patel, "Curvature, Torsion, and Force Sensing in Continuum Robots Using Helically Wrapped FBG Sensors," *IEEE Robotics and Automation Letters*, vol. 1, no. 2, pp. 1052–1059, 2016.

[271] A. Gao, N. Liu, M. Shen, M. EMK Abdelaziz, B. Temelkuran, and G.-Z. Yang, "Laser-profiled continuum robot with integrated tension sensing for simultaneous shape and tip force estimation," *Soft Robotics*, 2020.

[272] A. W. Mahoney, T. L. Bruns, P. J. Swaney, and R. J. Webster, "On the inseparable nature of sensor selection, sensor placement, and state estimation for continuum robots or "where to put your sensors and how to use them"," in *2016 IEEE International Conference on Robotics and Automation (ICRA)*, pp. 4472–4478, 2016.

[273] B. Kim, J. Ha, F. C. Park, and P. E. Dupont, "Optimizing curvature sensor placement for fast, accurate shape sensing of continuum robots," in *2014 IEEE International Conference on Robotics and Automation (ICRA)*, pp. 5374–5379, 2014.

[274] Northern Digital Inc., "NDI Aurora."

[275] L. Wu, S. Song, K. Wu, C. M. Lim, and H. Ren, "Development of a compact continuum tubular robotic system for nasopharyngeal biopsy," *Medical & Biological Engineering & Computing*, vol. 55, no. 3, pp. 403–417, 2017.

[276] A. Dore, G. Smoljkic, E. V. Poorten, M. Sette, J. V. Sloten, and G. Yang, "Catheter navigation based on probabilistic fusion of electromagnetic tracking and physically-based simulation," in *2012 IEEE/RSJ International Conference on Intelligent Robots and Systems*, pp. 3806–3811, 2012.

[277] H.-T. Ryu, J. Woo, B.-R. So, and B.-J. Yi, "Shape and contact force estimation of inserted flexible medical device," *International Journal of Control, Automation and Systems*, vol. 18, no. 1, pp. 163–174, 2020.

[278] D. C. Rucker and R. J. Webster, "Deflection-based force sensing for continuum robots: A probabilistic approach," in *2011 IEEE/RSJ International Conference on Intelligent Robots and Systems*, pp. 3764–3769, IEEE, 2011.

[279] H. Guo, F. Ju, Y. Cao, F. Qi, D. Bai, Y. Wang, and B. Chen, "Continuum robot shape estimation using permanent magnets and magnetic sensors," *Sensors and Actuators A: Physical*, vol. 285, pp. 519–530, 2019.

[280] S. Ozel, N. A. Keskin, D. Khea, and C. D. Onal, "A precise embedded curvature sensor module for soft-bodied robots," *Sensors and Actuators A: Physical*, vol. 236, pp. 349–356, 2015.

[281] S. Ozel, E. H. Skorina, M. Luo, W. Tao, F. Chen, Y. Pan, and C. D. Onal, "A composite soft bending actuation module with integrated curvature sensing," in *2016 IEEE International Conference on Robotics and Automation (ICRA)*, pp. 4963–4968, 2016.

[282] M. Luo, E. H. Skorina, W. Tao, F. Chen, S. Ozel, Y. Sun, and C. D. Onal, "Toward Modular Soft Robotics: Proprioceptive Curvature Sensing and Sliding-Mode Control of Soft Bidirectional Bending Modules," *Soft Robotics*, vol. 4, no. 2, pp. 117–125, 2017.

[283] A. M. Franz, T. Haidegger, W. Birkfellner, K. Cleary, T. M. Peters, and L. Maier-Hein, "Electromagnetic Tracking in Medicine—A Review of Technology, Validation, and Applications," *IEEE Transactions on Medical Imaging*, vol. 33, no. 8, pp. 1702–1725, 2014.

[284] M. Wagner, S. Schafer, C. Strother, and C. Mistretta, "4D interventional device reconstruction from biplane fluoroscopy," *Medical Physics*, vol. 43, no. 3, pp. 1324–1334, 2016.

[285] X. Wu, J. Housden, Y. Ma, B. Razavi, K. Rhode, and D. Rueckert, "Fast Catheter Segmentation From Echocardiographic Sequences Based on Segmenta-

tion From Corresponding X-Ray Fluoroscopy for Cardiac Catheterization Interventions," *IEEE Transactions on Medical Imaging*, vol. 34, no. 4, pp. 861–876, 2015.

[286] G. J. Vrooijink, M. Abayazid, and S. Misra, "Real-time three-dimensional flexible needle tracking using two-dimensional ultrasound," in *2013 IEEE International Conference on Robotics and Automation*, pp. 1688–1693, 2013.

[287] J. Burgner, S. D. Herrell, and R. J. Webster, "Toward fluoroscopic shape reconstruction for control of steerable medical devices," in *ASME 2011 Dynamic Systems and Control Conference and Bath/ASME Symposium on Fluid Power and Motion Control*, pp. 791–794, American Society of Mechanical Engineers, 2011.

[288] A. Yang and J. Szewczyk, "Marker-Assisted Image-Based 3D Monitoring for Active Catheters," in *The Hamlyn Symposium on Medical Robotics*, 2019.

[289] J. Janjic, F. Mastik, M. Leistikow, J. G. Bosch, A. F. W. van der Steen, and G. van Soest, "Imaging with a single-element forward-looking steerable IVUS catheter using optical shape sensing (Conference Presentation)," in *Proc.SPIE Medical Imaging 2017: Image-Guided Procedures, Robotic Interventions, and Modeling*, vol. 10135, 2017.

[290] P. T. Tran, P.-L. Chang, H. De Praetere, J. Maes, D. Reynaerts, J. V. Sloten, D. Stoyanov, and E. V. Poorten, "3D Catheter Shape Reconstruction Using Electromagnetic and Image Sensors," *Journal of Medical Robotics Research*, vol. 02, no. 03, p. 1740009, 2017.

[291] A. Vandini, C. Bergeles, F.-Y. Lin, and G.-Z. Yang, "Vision-based intraoperative shape sensing of concentric tube robots," in *2015 IEEE/RSJ International Conference on Intelligent Robots and Systems (IROS)*, pp. 2603–2610, IEEE, 2015.

[292] E. J. Lobaton, J. Fu, L. G. Torres, and R. Alterovitz, "Continuous shape estimation of continuum robots using X-ray images," in *2013 IEEE International Conference on Robotics and Automation*, pp. 725–732, 2013.

[293] P. Cabras, F. Nageotte, P. Zanne, and C. Doignon, "An adaptive and fully auto-

matic method for estimating the 3D position of bendable instruments using endoscopic images," *The International Journal of Medical Robotics and Computer Assisted Surgery*, vol. 13, no. 4, p. e1812, 2017.

[294] B. Rosa, V. Bordoux, and F. Nageotte, "Combining Differential Kinematics and Optical Flow for Automatic Labeling of Continuum Robots in Minimally Invasive Surgery," *Frontiers in Robotics and AI*, vol. 6, p. 86, 2019.

[295] S. H. Sadati, A. Shiva, N. Herzig, C. D. Rucker, H. Hauser, I. D. Walker, C. Bergeles, K. Althoefer, and T. Nanayakkara, "Stiffness imaging with a continuum appendage: Real-time shape and tip force estimation from base load readings," *IEEE Robotics and Automation Letters*, vol. 5, no. 2, pp. 2824–2831, 2020.

[296] K. Xu and N. Simaan, "An investigation of the intrinsic force sensing capabilities of continuum robots," *IEEE Transactions on Robotics*, vol. 24, no. 3, pp. 576–587, 2008.

Chapter 3

Materials for Soft Continuum Magnetic Robots

Chapter source: T. da Veiga, J. H. Chandler, G. Pittiglio, P. Lloyd, M. Holdar, O. Onaizah, A. Alazmani, and P. Valdastri, "Material Characterization for Magnetic Soft Robots", IEEE 4th International Conference on Soft Robotics (RoboSoft), 2021, pp. 335-342

Abstract

Magnetic soft robots are increasingly popular as they provide many advantages such as miniaturization and tetherless control that are ideal for applications inside the human body or in previously inaccessible locations.

While non-magnetic elastomers have been extensively characterized and modelled for optimizing the fabrication of soft robots, a systematic material characterization of their magnetic counterparts is still missing. In this paper, commonly employed magnetic materials made out of Ecoflex™ 00-30 and Dragon Skin™ 10 with different concentrations of NdFeB microparticles were mechanically and magnetically characterized. The magnetic materials were evaluated under uniaxial tensile testing and their behavior analyzed

through linear and hyperelastic model comparison. To determine the corresponding magnetic properties, we present a method to determine the magnetization vector, and magnetic remanence, by means of a force and torque load cell and large reference permanent magnet; demonstrating a high level of accuracy. Furthermore, we study the influence of varied magnitude impulse magnetizing fields on the resultant magnetizations. In combination, by applying improved, material-specific mechanical and magnetic properties to a 2-segment discrete magnetic robot, we show the potential to reduce simulation errors from 8.5% to 5.4%.

3.1 Introduction

The field of soft robots has drawn considerable attention over the past years, due to the wide range of potential applications enabled through the controlled use of highly compliant materials; several examples have been reported from minimally invasive surgical procedures to common grippers [1; 2; 3]. Recently, the specific use of magnetic actuation in soft robots has allowed new possibilities given their advantages such as miniaturization and untethered control. From flexible soft catheters [4; 5; 6; 7] to micro-robots with a wide range of locomotion capabilities [8; 9; 10], soft magnetic robots have gained increased attention from the robotics research community [11].

Mainly two types of magnetic soft robots have been reported [12]: those with embedded magnets within the elastomeric matrix [4; 13; 14], and those which make use of magnetic responsive elastomers (MRE) [5; 8; 6; 9; 10]. MRE are commonly achieved by mixing magnetic nano- or micro-particles within the elastomeric matrix and, hence, combine the elastic properties of the elastomer matrix with the magnetic properties of the particles [15; 16]. Embedding a magnetic moment is achieved via applying a strong magnetizing field, either through an impulse magnetizer [5; 17; 18] or a permanent magnet (PM) set up [10]. Impulse magnetizers offer advantages to the robotics community such as readiness, off-the-shelf and instant magnetization, over PM set-ups which cannot be switched off. Nonetheless, the resulting magnetization from impulse magnetizers obey

the skin effect, in which its value decreases in depth from the objects surface inwards [19].

To achieve precise modeling, actuation and control, soft robots rely on accurate material characterizations. Considerable efforts have been made to mechanically characterize frequently employed non-magnetic elastomers [20; 21; 22]. However, characterization of MRE is often restricted to their microstructure and particle behaviour [23; 24; 25], or to their magnetorheological properties [26; 27]; which fails to provide macro-level properties of interest from a robotics point of view [16]. Furthermore, these tend to pertain to elastomers and magnetic particles that are not common within the soft robotics community due to either higher stiffness or softer magnetic properties.

Several methods for determining materials' magnetic properties have been proposed and can be broadly classified into torque and force measurements (such as Torquemeter [28] and Faraday balance [29]); magnetometric measurements (Hall probe [30; 31]); inductive measurements (vibrating sample magnetometer (VSM) [18]); and magneto-optical (e.g. MagView (Matesy GmbH, Germany)) [10; 32; 33]. These techniques can be used to determine different material aspects, and overall are able to provide an exhaustive and highly accurate analysis. However, they come with their own limitations. Torque measurements are often restricted to spherical shaped samples. Magnetometric and inductive measurements, despite allowing sample shape freedom, require small and short samples [32]. Furthermore, static inductive measurements are only capable of performing relative measurements requiring a well-defined reference. Magneto-optical measurements are limited to surface properties, being unable to provide a characterization for the whole sample directly [34]. The requirement of specific sample designs and sizes, as well as limited access to such equipment, often leads to robotic applications using properties based either on the manufacturer's data or models applied to raw materials [9; 5].

To address this, we provide a material characterization of MRE commonly employed in soft robots [5; 18], from mechanical and magnetic perspectives. Two different elastomeric matrices with increasing concentrations of magnetic filler are characterized. For mechanical characterization we consider a tensile analysis of these different MRE and the

suitability of linear elastic and commonly employed hyperelastic models to represent their behavior. For magnetic characterization we present an easily implemented, cost-effective method for determining the magnetic moment of MRE samples. The method uses a load cell for measurements, not needing expensive single purposed magnetic specific equipment, and was used to study the influence of particle concentration, impulse magnetizing fields, and MRE stiffness on the resulting MRE magnetic moment. The results were then applied on two types of soft magnetic continuum robots to demonstrate the influence of robot-specific mechanical and magnetic characterization on simulation results.

3.2 Fabrication of magnetic soft material

In the present study, we consider the elastomers Ecoflex™ 00-30 (Smooth-On, Inc., U.S.A.) and Dragon Skin™ 10 (Smooth-On, Inc., U.S.A.), with all samples fabricated via molding techniques. To fabricate samples, the two-part elastomer was mixed in equal weights, followed by addition of the corresponding weight of hard magnetic micro-particles (NdFeB with an average 5 μm diameter and intrinsic coercivity of H_{ci} = 9.65 kOe, MQFP-B+, Magnequench GmnH, Germany). The mixture was then placed in a high vacuum-mixer (ARV-310, THINKYMIXER, Japan) for 90 seconds at a speed of 1400 rpm and pressure of 20.0 kPa and injected into the desired molds. Samples for the mechanical characterization were molded into dumbbell shape (type 2 on ISO 37:2917 [35]), whereas samples for the magnetization test were molded into cuboid shape of dimensions $7.5 \times 7.5 \times 4.0$ mm. The MRE were left to fully cure at room temperature before demolding. The samples for magnetic characterization were magnetized after curing under a magnetizing field B_m of 2.7 T or 5.0 T using an impulse magnetizer (IM-10-30, ASC Scientific, U.S.A.).

NdFeB concentrations were increased in 50% by weight increments up to the maximum supported by the elastomer matrix as listed in Table 3.1. Concentrations above those listed prohibited curing as thus were not considered in the study.

Table 3.1: Samples fabricated for characterization.

Elastomer	**Con. (wt%)**
Ecoflex™ 00-30	0
	50
	100
	150
Dragon Skin™ 10	0
	50
	100

3.3 Mechanical characterization

Destructive uniaxial tensile testing was applied to the different MRE samples. Their stress-strain responses were evaluated using a linear model, as well as commonly employed hyperelastic models.

3.3.1 Methods

The tensile test conditions were in accordance with ISO 37:2017 [35], using an Instron 5943 machine associated with a video-extensometer to record the elongation of the specimen. The markers for the video-extensometer were placed at 8 mm from the centre line of the specimen, and the pressure on the grippers was 20 psi. The experiments were run with a velocity of 500 mm/min until rupture. Five specimens for each type of MRE were tested.

The response of each MRE was evaluated by fitting a linear elastic model at 100% strain for all samples and retrieving the corresponding Young's modulus. Additionally, to understand the best modeling practices for MRE, a linear elastic model, and the hyperelastic models Mooney-Rivlin [36], Neo-Hookean [37], Ogden with three coefficients [38], Polynomial with 5 coefficients [39], and Yeoh [40] were fitted to the whole strain range of the obtained stress-strain curves. This was performed using a nonlinear least-squares solver from MATLAB (*lsqnonlin* function, MathWorks® Inc., U.S.A.).

3.3.2 Results and Discussion

Fig. 3.1 shows the stress-strain curves obtained for the different MRE, as well as the linear fits up to 100% strain. Table 3.2 lists the values of Young's modulus at 100% strain, as well as the mean absolute percentage errors (MAPE) of the linear and hyperelastic models for the whole strain range. Fig. 3.2 shows the fittings for the linear and hyperelastic models for the whole strain range for a sample of Ecoflex™ 00-30 and a sample of Dragon Skin™ 10 at 0 wt% NdFeB.

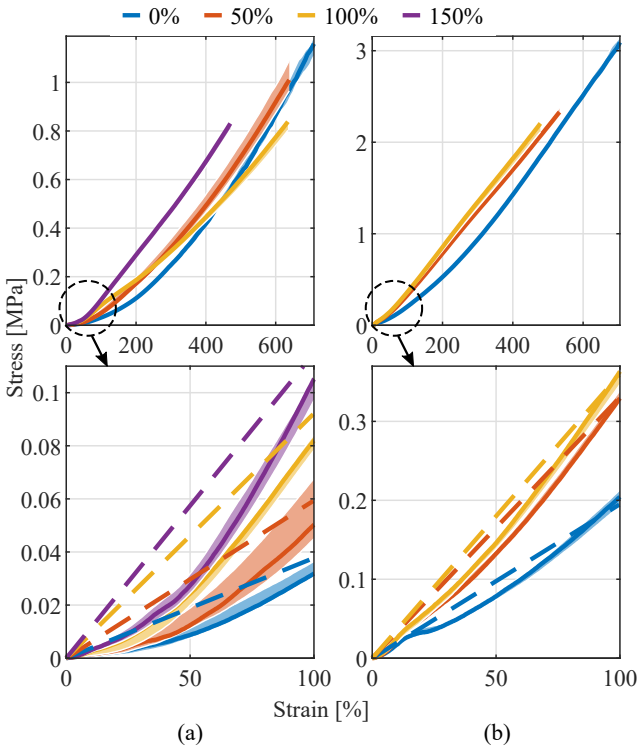

Figure 3.1: Stress-Strain curves under uniaxial tensile test for (a) Ecoflex™ 00-30 and (b) Dragon Skin™ 10 with increasing concentration of NdFeB microparticles. The shaded regions define the range of values obtained for each strain across five specimens, and the full lines the values for a single sample as an example. Additionally, the dashed lines represent the fitted linear model up to 100% strain.

For both MRE, an increase in concentration of NdFeB microparticles increases the measured stress for a given strain, representing a stiffening of the composites. In fact, a concentration of only 50 wt% NdFeB results in an increase of the Young's modulus by approximately 70% for both MRE. Ecoflex™ 00-30 allows high concentrations of NdFeB up to its maximum of 150 wt%. However, the rate of increase of the Young's modulus decreases as the concentration goes up. In fact, from 100 wt% to 150 wt%, an increase

Table 3.2: Results of model fitting to MRE tensile test data: showing the values of Young's modulus (E) for fitting up to 100% strain, and the mean absolute percentage error (MAPE) for all fitted models.

		Linear model			Hyperelastic models				
		100% strain		Full strain	Neo-Hookean	Mooney-Rivlin	Yeoh	Ogden	Polynomial
Elastomer	Con. (wt%)	E [kPa]	MAPE [%]	MAPE [%]	MAPE [%]	MAPE [%]	MAPE [%]	MAPE [%]	MAPE [%]
Ecoflex™ 00-30	0	42.7 ± 3.9	28.7	98.0	23.0	12.2	13.2	4.8	6.5
	50	73.2 ± 10.2	22.9	66.8	17.2	19.7	14.9	7.1	5.0
	100	102.1 ± 7.3	17.8	15.2	18.3	10.0	11.3	4.0	5.3
	150	128.2 ± 4.6	24.6	21.6	14.5	16.2	13.6	6.5	4.9
Dragon Skin™ 10	0	201.1 ± 12.0	13.6	33.0	11.3	18.9	16.0	3.6	2.1
	50	343.2 ± 9.1	10.0	9.7	20.6	13.2	9.4	3.4	1.6
	100	360.1 ± 10.9	9.9	9.2	19.4	9.2	8.5	3.3	1.3

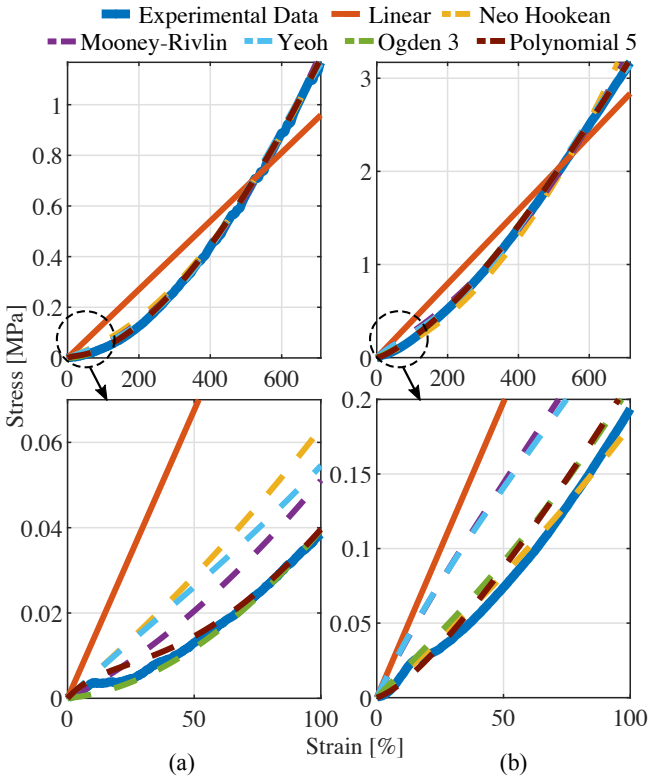

Figure 3.2: (a) Ecoflex™ 00-30 at 0 wt% NdFeB and (b) Dragon Skin ™ 10 at 0 wt% NdFeB fitted with a linear elastic model and different hyperelastic models for the whole strain range.

of only 26% is evident. Conversely, Dragon Skin™ 10 can only withstand a maximum concentration of 100 wt%. Nonetheless, only a small increase in stiffness exists when compared to a concentration of 50 wt%. This could have certain advantages as it would lead to higher magnetic volume while maintaining the mechanical properties of lower concentrations.

The addition of NdFeB microparticles also translates to a loss of hyperelasticity. This can be easily observed in the stress-strain curves in Fig. 3.1; as well as the lower fitting errors for the linear model as the concentration increases in Table 3.2. This loss of hy-

perelasticity is most significant for larger strains, where MRE with higher concentrations start to behave linearly. Despite this, fitting errors for linear models are still higher when compared to non-linear models. Generally, the Ogden model with 3 coefficients and the Polynomial with 5 coefficients exhibit the best results with the lowest fitting errors, while the Neo-Hookean and the Mooney-Rivlin models present the highest error values. Hyperelastic models show applicability to MRE, consistently providing more accurate predictions over corresponding linear models. Still, it is expected that at the maximum limit of magnetic content, the loss of accuracy using linear models will not be as significant as for lower concentrations.

3.4 Magnetic characterization

To magnetically characterize the different MRE, the samples were placed under an external magnetic field and field gradient, and the generated forces and torques measured. This is akin to magnetically actuated soft robotic applications, where actuation and control rely on the forces and torques exerted on the robot by the external magnetic field and field gradient. By measuring the forces and torques experienced by the samples, their magnetic properties can be determined. This method was first validated on small PMs, and then used to examine the influence of particle concentration, impulse magnetizing field intensity, and MRE stiffness on the resulting MRE's magnetization.

3.4.1 Methods

3.4.1.1 Theoretical Background

The magnetic force F and torque τ exerted on an object with magnetic moment m can be described by (3.1) and (3.2)

$$F = (m \cdot \nabla) B_e \tag{3.1}$$

$$\tau = m \times B_e \tag{3.2}$$

where B_e denotes the external magnetic field vector. In this work, B_e is generated by an axially magnetized cylindrical PM and is described by the following multipole expansion model in spherical coordinates [41]:

$$B_e(p) = \frac{\mu_0}{4\pi}\frac{\|m\|}{\mathrm{V}}\sum_{\mathrm{n\,odd}}\frac{\left(\frac{\mathrm{L}}{2}\right)^{\mathrm{n}+2}}{\|p\|^{\mathrm{n}+2}}\left((\mathrm{n}+1)D_{\mathrm{n}}\hat{r} - \frac{dD_{\mathrm{n}}}{d\theta}\hat{\theta}\right) \tag{3.3}$$

where μ_0 is the magnetic permeability of a vacuum, $\|m\|$ is the Euclidean norm of the PM's dipole moment, V the magnet's volume, L the magnet's length, p the vector from the centre of the PM to the point of interest in space, and D_n the following equation (3.4).

$$D_{\mathrm{n}}(\mathrm{n},\beta) = \begin{cases} 2\displaystyle\int_{\frac{1}{\sqrt{1+\beta^2}}}^{1}\int_{0}^{2\pi}\frac{\mathrm{P_n}(\hat{p}\cdot\hat{\rho}')}{\mathrm{x}^{\mathrm{n}+3}}\,\mathrm{d}\phi'\mathrm{d}x, & \text{if n is odd} \\ 0, & \text{if n is even} \end{cases} \tag{3.4}$$

where β represents the cylinder's diameter-to-length aspect ratio, and $\mathrm{P_n}(\cdot)$ the Legendre polynomial of order n [41]. Referring to Fig. 3.3, primed variables are defined relative to the PM for integration and all non-primed variables are defined relative to a global frame where the point of interest is defined [41].

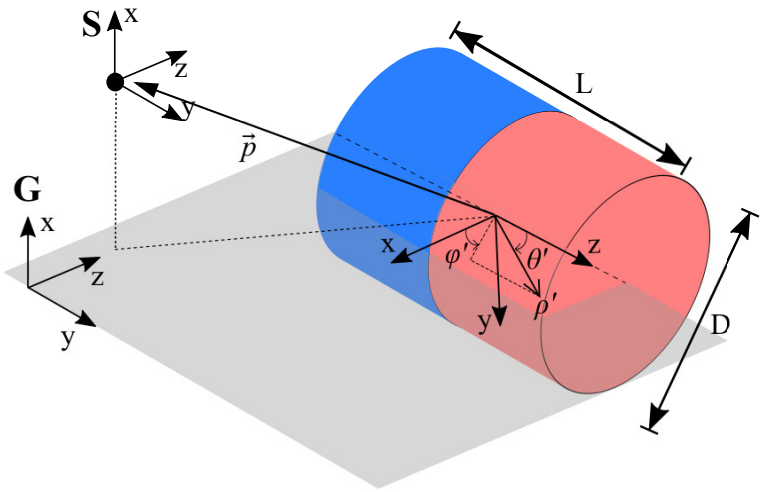

Figure 3.3: Geometrical definition of variables. G denotes the global reference frame, while S the sample's frame.

The dipole model, which consists of the first non-zero term (i.e. n = 1) of the previous multipole expansion model (3.3), is a simplifying assumption that generally yields good

results for small enough samples or large enough magnet-to-magnet distances [41]. This is normally the case for situations in magnetic control or localization algorithms [42; 43]. However, for the current application where maximum accuracy is desired, the multipole expansion model with a higher number of terms provides more accurate results. Therefore, the external field was computed using the first nine non-zero terms of the multipole expansion (i.e. n = 17); which have been reported to provide an error lower than 2% for distances greater than 1.5 minimum-bounding-sphere radii for axially magnetized cylindrical PMs with $\beta = 1$ [41].

Furthermore, B_e is a static magnetic field obeying Maxwell's equations (3.5) and (3.6).

$$\nabla \cdot \mathrm{B}_e = 0 \tag{3.5}$$

$$\nabla \times \mathrm{B}_e = \mu_0 \mathrm{J} \tag{3.6}$$

where J represents the current-density vector field, which is zero. Therefore, (3.1) and (3.2) can be rewritten as

$$\begin{bmatrix} F \\ \tau \end{bmatrix} = \begin{bmatrix} \nabla B_e \\ -B_{e\times} \end{bmatrix} m \tag{3.7}$$

where $(\cdot)_\times$ represents the skew operator.

Given its size, and keeping its distance from the PM large enough, the sample can be represented by a magnetic dipole. By measuring the forces and torques exerted on it, one can determine its magnetic moment using (3.7). Its magnetization $\mathrm{m_a}$, or magnetic remanence B_r, can then be determined via

$$\mathrm{m_a} = \frac{\|m\|}{V} \tag{3.8}$$

$$B_r = \frac{\|m\| \, \mu_0}{V} \tag{3.9}$$

3.4.1.2 Test rig

The test rig can be seen in Fig. 3.4. It is composed of a static cylindrical N52 PM (length and diameter of 101.6 mm, axially magnetized, B_r of 1.48 T) to generate the external magnetic field and gradient. The MRE sample is attached to a 6-axis load cell (Nano17 Titanium, ATI, U.S.A.), which is mounted on a motorized linear stage (NRT150/M, Thorlabs, Inc., U.S.A.). The presence of the linear motor allows the collection of data across different values of p. The PM and the motorized stage were placed orthogonally with their centres aligned, so that the magnetic sample moves to and from the centre of the PM along the Z axis in the global coordinate frame.

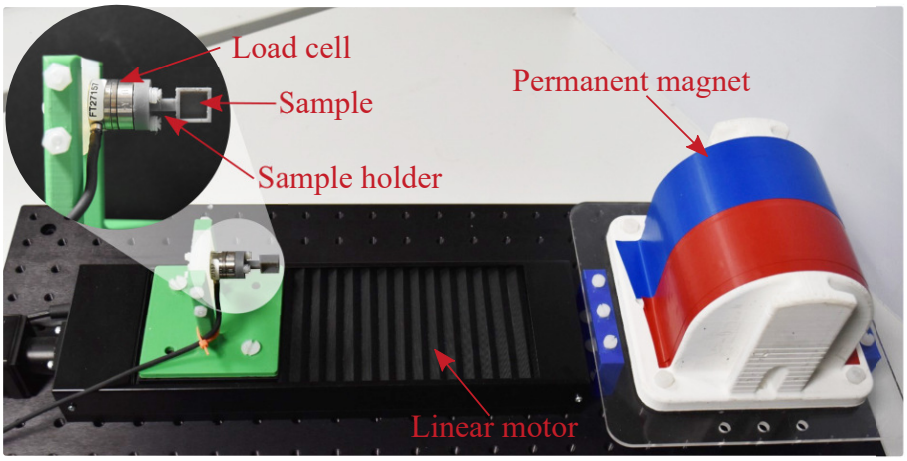

Figure 3.4: Setup for the magnetic characterization of MRE.

For each sample, the values of force and torque were measured across 16 discrete distances, from 16 to 31 cm, centre to centre, spaced 1 cm apart. To remove noisy measurements, the difference between each two positions was averaged for each axis of the measured F and τ. In case an axis' average was below a third of the maximum average recorded, the axis was zeroed. The test was repeated three times from each sample and the average and standard deviation across repetitions computed. Points with standard deviation over a third the average force or torque were excluded. The remaining averaged data was then fitted to (3.7) in order to determine the values of m, using a non-linear least squares method (*lsqnonlin* function, MATLAB, MathWorks® Inc., U.S.A.).

3.4.2 Validation

The characterization approach was validated using two small PMs as samples varying in shape and size, a cubic N52 NdFeB PM of 6.35 mm length (B444-N52, K&J Magnetics Inc, U.S.A.), and a cylindrical N52 NdFeB of 3.18 mm diameter and length (D22-N52, K&J Magnetics Inc, U.S.A.). Their magnetizations were aligned with the Z axis of the global coordinate frame. Fig. 3.5 depicts the measured values of force and torque, against the fitted results for the cubic sample. As it can be seen, only the expected components of force and torque were activated and the measurements have very low deviation across repetitions. The B_r obtained was of 1.44 T, falling within the range expected for N52 magnets (K&J Magnetics, Inc., U.S.A.).

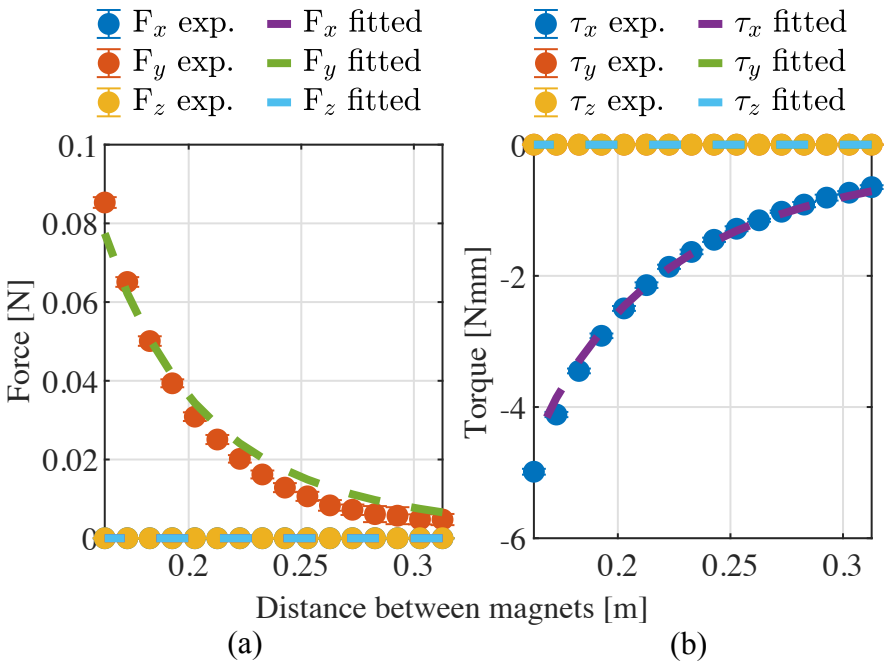

Figure 3.5: (a) Force and (b) Torque measurements for a 6.35 mm cubic N52 magnet as a sample, and modelled values from fitting. MAPE 2.6%.

The current configuration works well for high remanence/large samples, such as the tested cubic PM. However, for samples with lower values, the resolution of the load cell will restrict the accuracy of the measurement. Nevertheless, one of its advantages is its flexibility to conform to specific user or equipment requirements. By varying sample size; PM size and grade; distance and relative position between PM and sample; and load

cell's sensitivity, one can tailor the platform to the desired application and samples to measure.

For this specific case, force data is prone to have lower signal-to-noise ratio due to the load cell's lower force resolution when compared to torque. For that reason, only torque values can be considered in order to obtain an accurate measurement. Due to the current and fixed relative position and orientation between the PM and the sample, using only torque values hinders the possibility of obtaining the full magnetization vector. Therefore, two sample orientations were measured so that the full magnetization vector could be computed, according to (3.10),

$$ {}^{G}\tau = {}^{G}(-B_{\times})\ {}^{G}R_{S}\ {}^{S}m \tag{3.10} $$

where ${}^{G}(\cdot)$ denotes representation on the global reference frame, and ${}^{S}(\cdot)$ on the sample's reference frame, ${}^{G}R_{S}$ denotes the rotation matrix between the sample's and global reference frames. The second orientation used was 90° around the sample's y axis with respect to the first orientation. The corresponding results for the cubic and cylindrical validation PMs can be seen in Fig. 3.6, with remanence values of 1.46 T and 1.44 T respectively. As it can be seen, even though the torque values for the cylindrical PM are much lower, the method still gives an accurate reading of its magnetic remanence.

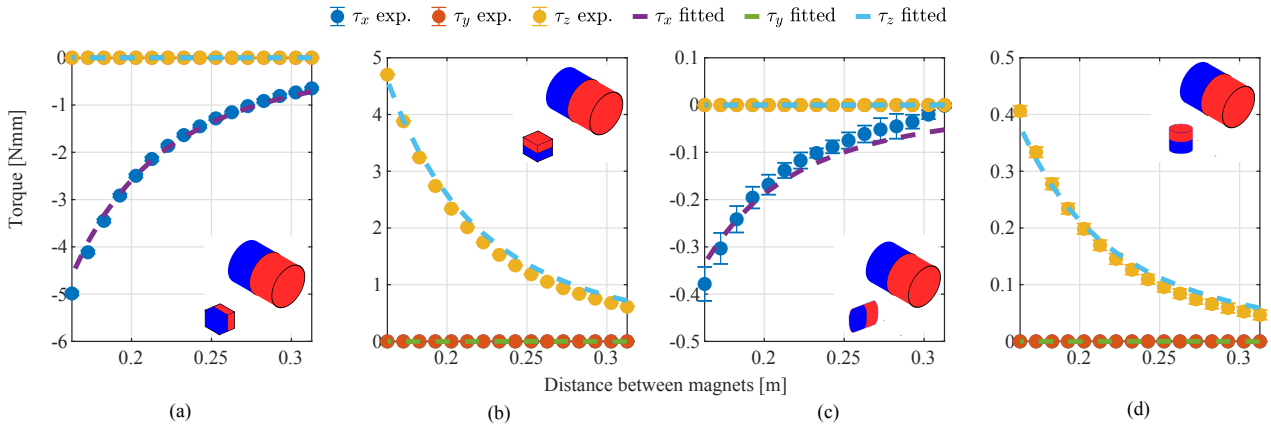

Figure 3.6: Torque measurements for the validation step using permanent magnet samples, showing: cubic 6.3 mm PM (MAPE 3.1%) in (a) rotation 1, (b) rotation 2; and cylindrical 3.2 mm PM (MAPE 6.2%) in (c) rotation 1, (d) rotation 2.

3.4.3 Results

3.4.3.1 Effect of particle concentration on MRE

Fig. 3.7 depicts the values of m_a obtained for the tested MRE samples. As expected, the higher the magnetic content, the higher the value of m_a obtained. This increase of m_a with concentration is not linear as it gradually slows down as the concentration increases. In fact, for samples magnetized under $B_m = 2.7$ T, the ratio of remanence-to-concentration between 50 wt% and 100 wt% is of 0.136 T/wt%, decreasing to 0.096 T/wt% between 100 wt% and 150 wt%.

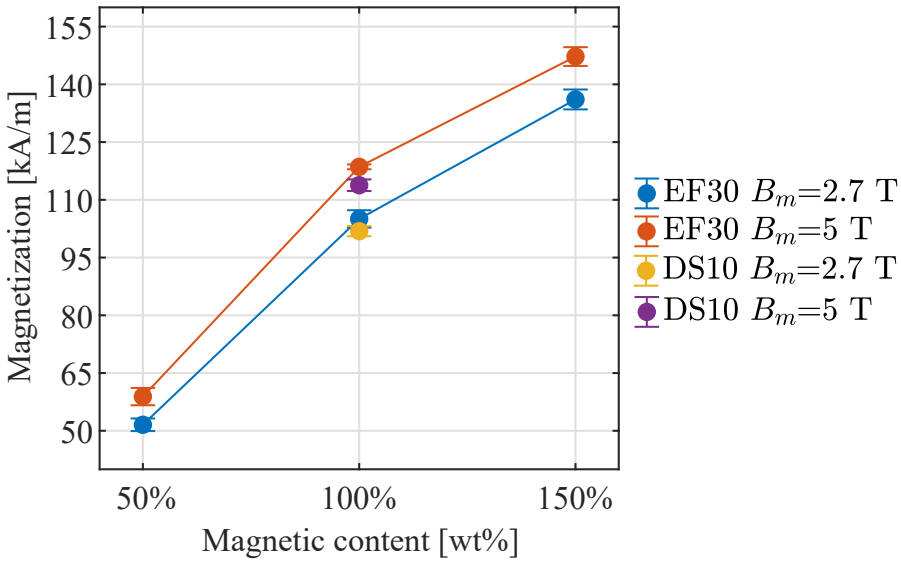

Figure 3.7: Effect of the magnetic particle content and magnetizing field on the values of magnetization of MREs.

3.4.3.2 Effect of impulse magnetizing field intensity on MRE

Different values of B_m gave rise to different values of m_a, even though both B_m were over the particles' intrinsic coercivity. This verifies the limitation that impulse magnetizing fields have in which the depth of penetration depends on the sample's shape and size, obeying the skin effect [19]. Therefore, even though the magnitude of B_m is more than double the intrinsic coercivity of the samples when equal to 2.7 T, it is not enough to

Table 3.3: Magnetization vector angle deviations after re-magnetization at a 90° angle.

Elastomer	**Con. (wt%)**	$\mathbf{B_m = 2.7\ T}$	$\mathbf{B_m = 5\ T}$
Ecoflex ™ 00-30	100	55 ±1°	90 ±1°
Dragon Skin™ 10	100	61 ±1°	90 ±2°

fully magnetize the sample.

3.4.3.3 Effect of stiffness on MRE

As seen in Fig. 3.7, no significant difference was found between Ecoflex™ 00-30 and Dragon Skin™ 10 samples. This indicates that these matrices do not affect the magnetic properties of the final MRE when submitted to a single magnetizing field. However, it has been shown that the first magnetization loop of MRE differs from the following one due to possible restructuring of the particles and elastomeric matrix, depending on the matrix's stiffness [25].

To further study this effect, samples of Ecoflex™ 00-30 and Dragon Skin™ 10 loaded at 100 wt% were submitted to two consecutive perpendicular magnetizing fields with the same previous intensities. Table 3.3 lists the average magnetization vector deviation angle with respect to the original direction. For lower impulse magnetizing fields, the resulting magnetization direction was not aligned with the magnetizing field, but at offset dependent on the MRE stiffness. The stiffer the MRE the higher the shift. When $B_m = 5$ T, the shift in magnetization is complete at an average of 90° for all elastomers, indicating that high impulse magnetizing fields are able to overcome any restructuring of softer matrices and particle movement and fully re-magnetize the composite.

3.5 Validation

To validate the characterization results, soft magnetic continuum robots were fabricated and actuated under a uniform external magnetic field. Two types of robots were studied, covering the designs showcased in the literature: fully soft magnetic robots [6] and

fully soft robots with magnetic and non-magnetic regions [5]. Their behavior was then compared to the corresponding 2D finite element models (FEM) either assuming the theoretical properties or our corrected values. Both the fabrication methods and FEM have been previously described in [5].

Fig. 3.8 shows the results obtained for the fully soft magnetic continuum robot. The robot, which is 37 mm long and 5 mm in diameter, consists of Ecoflex™ 00-30 loaded at 100 wt% NdFeB, axially magnetized under the both previous B_m values (2.7 T and 5 T). Fig. 3.8(b) shows the experimental deflections obtained for both magnetizing fields. As it can be seen, the robot magnetized under 5 T exhibits a slightly larger deflection. Given that both B_m values are over the particles' intrinsic coercivity value, the theoretical magnetic remanence does not distinguish the two; assuming a value of 107 mT for both cases. Furthermore, the material is modelled linearly with a Young's modulus of 69 kPa, as per its datasheet. On the contrary, our corrected values are able to distinguish between the two different B_m, as well as provide a more accurate value of Young's modulus. This difference is enough to achieve deflections closer to the real-life results, lowering MAPE errors from 9.9% to 7.5% for $B_m = 2.7$ T, and 11.5% to 5.6% when $B_m = 5$ T. The remaining error can be further reduced by studying how the mechanical properties of the MRE change when under actuation, as well as using application specific values.

The results achieved for the fully soft discrete magnetic continuum robot are presented in Fig. 3.9. The robot is 40 mm long, and 3 mm in diameter. It is made of Ecoflex™ 00-30, consisting of plain sections alternated with axially magnetized 150 wt% NdFeB sections. The robot was magnetized under 5 T to achieve maximum magnetization. In this case, theoretical values are blind to mechanical differences between sections, assuming a constant Young's modulus of 69 kPa for the whole length of the robot. The corrected model, on the other hand, is able to provide a responsive value of Young's modulus with increasing concentration of NdFeB, as well as a more accurate value of magnetic remanence, lowering the MAPE error from 8.5% to 5.4%.

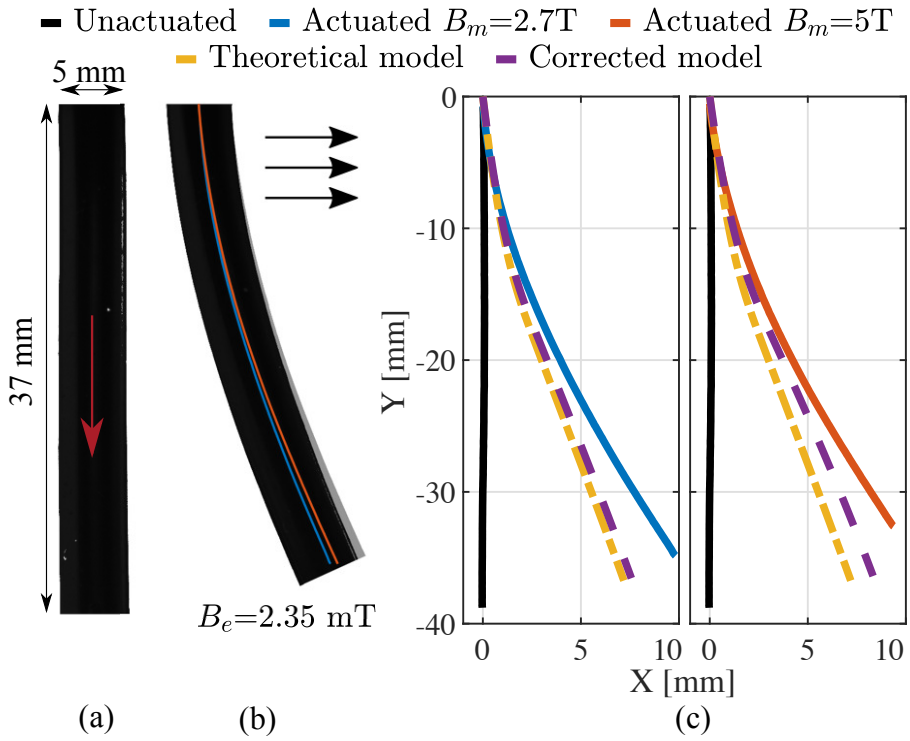

Figure 3.8: (a) Fully soft magnetic continuum robot. The red arrow represents its magnetization direction. (b) The robot under actuation in an uniform magnetic field with direction represented by the black arrows. (c) Simulation results considering our corrected model and the theoretical model.

3.6 Conclusions

In this paper, we presented a material characterization for magnetic elastomers commonly employed in soft robots that is able to reduce errors in their modeling and simulation.

Tensile testing and a hyperelasticity analysis of Ecoflex™ 00-30 and Dragon Skin™ 10 showed that an increase in concentration of NdFeB content, in addition to stiffening the MRE, translates into a loss of hyperelasticity. Even so, for the majority of the cases, hyperelastic models are still able to predict the materials' behavior more accurately than linear models, especially hyperelastic models Ogden and Polynomial.

To magnetically characterize the MRE, we propose a method based on a 6 degree of freedom load cell that measures the forces and torques exerted on the sample by an external PM. One can finely tune parameters (for example the PM specifications, its distance and relative orientation to the sample, load cell's accuracy, and samples' physical

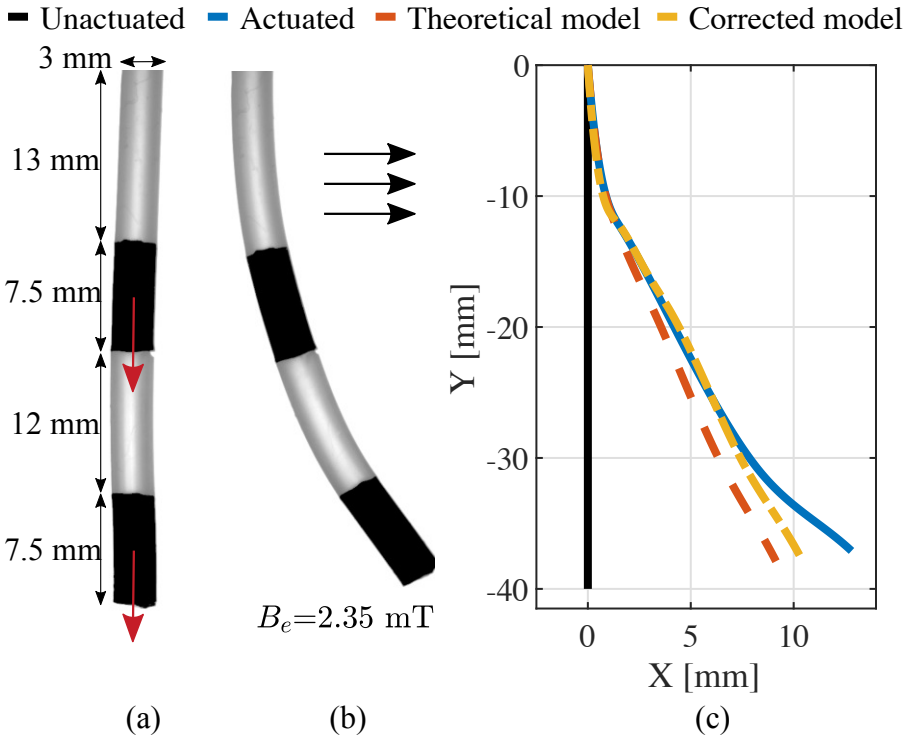

Figure 3.9: (a) Fully soft discrete magnetic continuum robot. The red arrows represent the direction of magnetization. (b) The robot under actuation in an uniform magnetic field with direction represented by the black arrows. (c) Simulation results considering our correct model and the theoretical model.

size and remanence) to achieve optimal results. For example, smaller distances require less sensitive load cells and allow smaller and weaker samples, however, errors associated with the dipole assumption will increase. Larger distances, on the other hand, decrease errors from the dipole model assumption but require larger and stronger samples, and highly sensitive load cells in order to guarantee an acceptable signal-to-noise ratio. Additionally, the load cell needs to be calibrated in an external-magnetic-field-free environment before each measurement, and have minimum magnetic interferences during measurements to maximize measurement quality. The method was validated using PMs of different sizes and shapes as samples, and shown to be able to determine their magnetization vector and remanence accurately. The method was used to characterize MRE and study the effect of particle concentration, intensity of impulse magnetizing field, and elastomer stiffness on the resultant MRE magnetic properties. Higher magnetic content leads to higher magnetization non-linearly, as it slows down with concentration. Furthermore, unlike impulse fields 5.2 times the MRE intrinsic coercivity value, impulse fields 2.8 times

were not able to fully magnetize the samples, reflecting the dependency on skin effect's. Matrix stiffness was shown to have an effect on the resulting magnetization direction when subjected to multiple magnetization cycles. Nevertheless, this effect is only present in lower magnetizing impulse fields.

As these factors (elasticity, magnetization value and history, and concentration of magnetic content) all influence the properties of the soft robot in interconnected and nonlinear ways, having a practical method to characterize properties provides a useful tool in improved design, modeling, and simulation of magnetic soft robots. As such, these findings were subsequently validated on two types of fully soft magnetic continuum robots and shown to reduce modeling errors on average by 37% when compared to using theoretical parameters normally provided by manufacturers or parameters from raw data. This reduction can be further increased by utilizing application strain specific mechanical properties and models, testing how the mechanical properties of the MRE change when under actuation, and more repeatable and accurate soft robot fabrication methods.

Acknowledgement

Research reported in this article was supported by the Royal Society, by the Engineering and Physical Sciences Research Council (EPSRC) under grant numbers EP/R045291/1 and EP/V009818/1, and by the European Research Council (ERC) under the European Union's Horizon 2020 research and innovation programme (grant agreement No 818045). Any opinions, findings and conclusions, or recommendations expressed in this article are those of the authors and do not necessarily reflect the views of the Royal Society, EPSRC, or the ERC.

Bibliography

[1] D. Rus and M. T. Tolley, "Design, fabrication and control of soft robots," *Nature*, vol. 521, no. 7553, pp. 467–475, 2015.

[2] M. Cianchetti, T. Ranzani, G. Gerboni, T. Nanayakkara, K. Althoefer, P. Dasgupta, and A. Menciassi, "Soft robotics technologies to address shortcomings in today's minimally invasive surgery: the stiff-flop approach," *Soft robotics*, vol. 1, no. 2, pp. 122–131, 2014.

[3] G. M. Whitesides, "Soft robotics," *Angewandte Chemie International Edition*, vol. 57, no. 16, pp. 4258–4273, 2018.

[4] S. Jeon, A. K. Hoshiar, K. Kim, S. Lee, E. Kim, S. Lee, J.-y. Kim, B. J. Nelson, H.-J. Cha, B.-J. Yi, *et al.*, "A magnetically controlled soft microrobot steering a guidewire in a three-dimensional phantom vascular network," *Soft robotics*, vol. 6, no. 1, pp. 54–68, 2019.

[5] P. R. Lloyd, T. Da Veiga, A. Attanasio, N. Marahrens, J. H. Chandler, P. Valdastri, *et al.*, "A learnt approach for the design of magnetically actuated shape forming soft tentacle robots," *IEEE Robotics and Automation Letters*, 2020.

[6] Y. Kim, G. A. Parada, S. Liu, and X. Zhao, "Ferromagnetic soft continuum robots," *Science Robotics*, vol. 4, no. 33, p. eaax7329, 2019.

[7] P. Lloyd, G. Pittiglio, J. H. Chandler, and P. Valdastri, "Optimal design of soft continuum magnetic robots under follow-the-leader shape forming actuation," *2020 International Symposium on Medical Robotics (ISMR)*, 2020. accepted.

[8] W. Hu, G. Z. Lum, M. Mastrangeli, and M. Sitti, "Small-scale soft-bodied robot with multimodal locomotion," *Nature*, vol. 554, no. 7690, pp. 81–85, 2018.

[9] V. K. Venkiteswaran, L. F. P. Samaniego, J. Sikorski, and S. Misra, "Bio-inspired terrestrial motion of magnetic soft millirobots," *IEEE Robotics and automation letters*, vol. 4, no. 2, pp. 1753–1759, 2019.

[10] T. Xu, J. Zhang, M. Salehizadeh, O. Onaizah, and E. Diller, "Millimeter-scale flexible robots with programmable three-dimensional magnetization and motions," *Science Robotics*, vol. 4, no. 29, p. eaav4494, 2019.

[11] T. da Veiga, J. H. Chandler, P. Lloyd, G. Pittiglio, N. J. Wilkinson, A. K. Hoshiar, R. A. Harris, and P. Valdastri, "Challenges of continuum robots in clinical context: a review," *Progress in Biomedical Engineering*, vol. 2, no. 3, p. 032003, 2020.

[12] J. J. Abbott, E. Diller, and A. J. Petruska, "Magnetic methods in robotics," *Annual Review of Control, Robotics, and Autonomous Systems*, vol. 3, 2020.

[13] C. Chautems, A. Tonazzini, D. Floreano, and B. J. Nelson, "A variable stiffness catheter controlled with an external magnetic field," in *2017 IEEE/RSJ International Conference on Intelligent Robots and Systems (IROS)*, pp. 181–186, IEEE, 2017.

[14] A. J. Petruska, "Open-loop orientation control using dynamic magnetic fields," *IEEE Robotics and Automation Letters*, vol. 5, no. 4, pp. 5472–5476, 2020.

[15] M. Schümann, D. Y. Borin, S. Huang, G. K. Auernhammer, R. Müller, and S. Odenbach, "A characterisation of the magnetically induced movement of ndfeb-particles in magnetorheological elastomers," *Smart Materials and Structures*, vol. 26, no. 9, p. 095018, 2017.

[16] N. Bira, P. Dhagat, and J. R. Davidson, "A review of magnetic elastomers and their role in soft robotics," *Frontiers in Robotics and AI*, vol. 7, p. 146, 2020.

[17] R. Zhao, Y. Kim, S. A. Chester, P. Sharma, and X. Zhao, "Mechanics of hard-magnetic soft materials," *Journal of the Mechanics and Physics of Solids*, vol. 124, pp. 244–263, 2019.

[18] Y. Kim, H. Yuk, R. Zhao, S. A. Chester, and X. Zhao, "Printing ferromagnetic domains for untethered fast-transforming soft materials," *Nature*, vol. 558, no. 7709, pp. 274–279, 2018.

[19] J. Stöhr and H. C. Siegmann, "Magnetism," *Solid-State Sciences. Springer, Berlin, Heidelberg*, vol. 5, 2006.

[20] C. Schumacher, E. Knoop, and M. Bacher, "Simulation-ready characterization of soft robotic materials," *IEEE Robotics and Automation Letters*, 2020.

[21] J. C. Case, E. L. White, and R. K. Kramer, "Soft material characterization for robotic applications," *Soft Robotics*, vol. 2, no. 2, pp. 80–87, 2015.

[22] D. Steck, J. Qu, S. B. Kordmahale, D. Tscharnuter, A. Muliana, and J. Kameoka, "Mechanical responses of ecoflex silicone rubber: Compressible and incompressible behaviors," *Journal of Applied Polymer Science*, vol. 136, no. 5, p. 47025, 2019.

[23] G. Stepanov, D. Y. Borin, A. Bakhtiiarov, and P. Storozhenko, "Negative coercivity of magnetic elastomers filled with magnetically hard particles," *Journal of Magnetism and Magnetic Materials*, vol. 498, p. 166125, 2020.

[24] K. Kalina, J. Brummund, P. Metsch, M. Kästner, D. Y. Borin, J. Linke, and S. Odenbach, "Modeling of magnetic hystereses in soft mres filled with ndfeb particles," *Smart Materials and Structures*, vol. 26, no. 10, p. 105019, 2017.

[25] J. M. Linke, D. Y. Borin, and S. Odenbach, "First-order reversal curve analysis of magnetoactive elastomers," *RSC advances*, vol. 6, no. 102, pp. 100407–100416, 2016.

[26] W. Li, Y. Zhou, and T. Tian, "Viscoelastic properties of mr elastomers under harmonic loading," *Rheologica acta*, vol. 49, no. 7, pp. 733–740, 2010.

[27] W. Li, X. Zhang, and H. Du, "Development and simulation evaluation of a magnetorheological elastomer isolator for seat vibration control," *Journal of Intelligent Material Systems and Structures*, vol. 23, no. 9, pp. 1041–1048, 2012.

[28] A. Aldenkamp, C. Marks, and H. Zijlstra, "Frictionless recording torque magnetometer," *Review of Scientific Instruments*, vol. 31, no. 5, pp. 544–546, 1960.

[29] B. L. Morris and A. Wold, "Faraday balance for measuring magnetic susceptibility," *Review of Scientific Instruments*, vol. 39, no. 12, pp. 1937–1941, 1968.

[30] X. Granados, S. Sena, E. Bartolomé, A. Palau, T. Puig, X. Obradors, M. Carrera, J. Amorós, and H. Claus, "Characterization of superconducting rings using an in-field hall probe magnetic mapping system," *IEEE Transactions on applied superconductivity*, vol. 13, no. 2, pp. 3667–3670, 2003.

[31] M. Kustov, P. Laczkowski, D. Hykel, K. Hasselbach, F. Dumas-Bouchiat, D. O'Brien, P. Kauffmann, R. Grechishkin, D. Givord, G. Reyne, *et al.*, "Magnetic characterization of micropatterned nd–fe–b hard magnetic films using scanning hall probe microscopy," *Journal of Applied Physics*, vol. 108, no. 6, p. 063914, 2010.

[32] F. Fiorillo, *Measurement and characterization of magnetic materials*. North-Holland, 2004.

[33] Y. Alapan, A. C. Karacakol, S. N. Guzelhan, I. Isik, and M. Sitti, "Reprogrammable shape morphing of magnetic soft machines," *Science Advances*, vol. 6, no. 38, p. eabc6414, 2020.

[34] A. Hubert and R. Schäfer, *Magnetic domains: the analysis of magnetic microstructures*. Springer Science & Business Media, 2008.

[35] ISO, "Rubber, vulcanized or thermoplastic — determination of tensile stress-strain properties," ISO 37, International Organization for Standardization, Geneva, Switzerland, 2017.

[36] M. Mooney, "A theory of large elastic deformation," *Journal of applied physics*, vol. 11, no. 9, pp. 582–592, 1940.

[37] B. Kim, S. B. Lee, J. Lee, S. Cho, H. Park, S. Yeom, and S. H. Park, "A comparison among neo-hookean model, mooney-rivlin model, and ogden model for chloroprene rubber," *International Journal of Precision Engineering and Manufacturing*, vol. 13, no. 5, pp. 759–764, 2012.

[38] R. W. Ogden, "Large deformation isotropic elasticity–on the correlation of theory and experiment for incompressible rubberlike solids," *Proceedings of the Royal Society of London. A. Mathematical and Physical Sciences*, vol. 326, no. 1567, pp. 565–584, 1972.

[39] R. S. Rivlin and D. Saunders, "Large elastic deformations of isotropic materials vii. experiments on the deformation of rubber," *Philosophical Transactions of the Royal*

Society of London. Series A, Mathematical and Physical Sciences, vol. 243, no. 865, pp. 251–288, 1951.

[40] O. H. Yeoh, "Some forms of the strain energy function for rubber," *Rubber Chemistry and technology*, vol. 66, no. 5, pp. 754–771, 1993.

[41] A. J. Petruska and J. J. Abbott, "Optimal permanent-magnet geometries for dipole field approximation," *IEEE transactions on magnetics*, vol. 49, no. 2, pp. 811–819, 2012.

[42] A. Z. Taddese, P. R. Slawinski, M. Pirotta, E. De Momi, K. L. Obstein, and P. Valdastri, "Enhanced real-time pose estimation for closed-loop robotic manipulation of magnetically actuated capsule endoscopes," *The International journal of robotics research*, vol. 37, no. 8, pp. 890–911, 2018.

[43] L. Barducci, G. Pittiglio, J. C. Norton, K. L. Obstein, and P. Valdastri, "Adaptive dynamic control for magnetically actuated medical robots," *IEEE robotics and automation letters*, vol. 4, no. 4, pp. 3633–3640, 2019.

Chapter 4

Static Localization for Magnetically Actuated Robots

Chapter source: T. da Veiga, G. Pittiglio, M. Brockdorff, J. H. Chandler, and P. Valdastri, "Six-degree-of-freedom Localization Under Multiple Permanent Magnets Actuation", IEEE Robotics and Automation Letter, vol. 8, no. 6, pp. 3422 - 3429.

Abstract

Localization of magnetically actuated medical robots is essential for accurate actuation, closed loop control and delivery of functionality. Despite extensive progress in the use of magnetic field and inertial measurements for pose estimation, these have been either under single external permanent magnet actuation or coil systems. With the advent of new magnetic actuation systems comprised of multiple external permanent magnets for increased control and manipulability, new localization techniques are necessary to account for and leverage the additional magnetic field sources. In this letter, we introduce a novel magnetic localization technique in the Special Euclidean Group SE(3) for multiple external permanent magnetic field actuation and control systems. The method relies on a milli-meter scale three-dimensional accelerometer and a three-dimensional magnetic field sensor and is able to estimate the full 6 degree-of-freedom pose without any prior

pose information. We demonstrated the localization system with two external permanent magnets and achieved localization errors of 8.5 ± 2.4 mm in position norm and 3.7 ± 3.6° in orientation, across a cubic workspace with 20 *cm* length.

4.1 Introduction

Magnetically actuated medical robots (MAMR) have seen significant focus and development in recent decades due to their potential for miniaturization [1], tether-less actuation [2] and high number of controllable degrees-of-freedom (DOFs) [3; 4]. In fact, magnetically guided catheters have been used to treat cardiac arrhythmias since 2003 [5; 6].

A key aspect in their actuation is pose estimation [7; 8], enabling closed loop control and delivery of functionality [9]. Imaging techniques have long been used for this purpose but are generally tied to limited resolution, harmful radiation exposure and need for additional hospital equipment [10; 11; 12]. As such, methods based on magnetic field measurements have received significant attention, with magnetic tracking systems being widely available on the market. These, however, are not compatible with magnetic actuation systems due to distortions on the localization magnetic fields.

To address this issue, significant research on magnetic localization coupled with magnetic actuation systems has been done [13; 2; 14; 15; 16]. Several works have been based on magnetic field sensing arrays external to MAMR [17; 14]. While advantageous from a miniaturization and internal power consumption point of view, these systems require calibration of large sensor arrays and have limited localization workspace dimensions. Internal sensing to the MAMR, on the other hand, does not suffer from workspace dimension restrictions. It requires, however, on-board power and heterogeneous localization magnetic fields, with 6-DOF localization having been shown for systems with a single external permanent magnet (EPM). Internal sensing methods have been shown for endoscopic capsules, as well as magnetically guided catheters [2; 18; 16; 19].

Over recent years the need for enhanced control and manipulability of MAMRs has led to the advent of actuation platforms based on multiple magnetic field sources (MMFS) such

as multiple electromagnetic coils and multiple permanent magnets [20; 21; 22; 4; 23; 24]. Some of these platforms have been cleared for human use such as Stereotaxis Genesis RMN® based on two permanent magnets, and Magnetecs and Aeon Scientific based on multiple electromagnetic coils.

Despite this progress, magnetic localization for such systems is lagging behind, with fluoroscopic imaging being currently used [5]. Unlike single magnetic field source systems where the singularity regions and localization limitations have been thoroughly investigated and solved for [16], magnetic localization for MMFS systems suffers from additional challenges due to the superposition of the magnetic fields leading to configuration-specific singularity regions. Only recently, a 3D position localization system with internal magnetic field sensing was demonstrated for a multi-coil system, for a 3 mm catheter [19].

Furthermore, a common conundrum in 6-DOF magnetic localization with internal sensing is finding the rotation around gravity, due to the absence of the Earth's magnetic field measurement [25]. This has been solved in the past by accurately initializing this missing rotation angle and tracking it with a gyroscope [26; 27]. However, this is prone to errors over time, especially for slow moving systems where gyroscope data is not as sensitive. Additionally, if communication to the MAMR is lost, a new accurate initialization is needed, proving impossible mid medical intervention. More recently, Taddese et al. [16] fitted an auxiliary coil around a single EPM providing a second set of magnetic field measurements. This solves the missing rotation angle and is also able to eliminate the localization singularity plane when it comes to localization with respect to a single EPM. However, when MMFS are present in the workspace, that singularity plane ceases to exist due to the superposition of magnetic fields, and instead singularity regions are present depending on the relative pose of each EPM.

This paper introduces, for the first time, a 6-DOF magnetic localization method for systems with multiple EPMs without the need for any prior pose information. The method relies on measurements from an accelerometer and a single 3D magnetic field Hall effect sensor (HE), both internal to the MAMR. We analyze the effect that the

number of EPMs in the workspace has on the full pose estimation; and demonstrate its performance in a two EPM magnetic actuation platform. Since adding an orthogonal coil is not able to solve for the singularity regions, in this work we do not consider it and instead solve for the missing rotation angle by using multiple magnetic field measurements at different EPM configurations. This works for static or quasi-static systems, with maximum MAMR velocity highly dependent on the actuation system and the magnetic field generated. This is the case for non-actuated parts of a larger system, such as the deployment point at the tip of an endoscope, or for MAMRs while the generated magnetic fields are sufficiently weak to induce actuation. Additionally, unlike common works in literature which parameterize the rotation matrix, in this work the full 6-DOF pose is estimated directly in the special euclidean group $SE(3)$. This avoids any singularities or non-unique representations of the orientation when using Euler angles or quaternions [28; 29; 16].

4.2 Localization Strategy

4.2.1 Problem Formulation

We consider finding the pose of a MAMR, with frame $\{\mathcal{A}\}$ within our workspace $\{\mathcal{W}\}$ (see Fig. 4.1). Its position is denoted as $\mathbf{p} \in \mathbb{R}^3$ in $\{\mathcal{W}\}$ and attitude as rotation matrix $R \in SO(3)$ of the MAMR frame $\{\mathcal{A}\}$ relative to $\{\mathcal{W}\}$. Additionally, the MAMR's linear velocity is denoted by $\mathbf{V} \in \mathbb{R}^3$ expressed in $\{\mathcal{W}\}$. The MAMR's angular velocity expressed in $\{\mathcal{W}\}$ relative to $\{\mathcal{A}\}$ is represented by $\mathbf{\Omega} \in \mathbb{R}^3$.

We describe our state in the special euclidean group $SE(3)$, i.e. the group of homogenous transformations with entries in $\mathbb{R}^3$ associated with the Lie algebra, $\mathfrak{se}(3)$ of dimension 6. The main goal is to estimate the homogenous transformation matrix from the MAMR reference frame $\{\mathcal{A}\}$ to the global frame $\{\mathcal{W}\}$ (see Fig. 4.1).

$$\mathrm{T} = {}^{\mathcal{W}}\mathrm{T}_{\mathcal{A}} : \{A\} \rightarrow \{W\}$$

Therefore, the dynamics model can be represented as

$$\dot{\mathrm{T}} = \mathrm{T} \begin{bmatrix} (\boldsymbol{\Omega} + \mathbf{b} + \boldsymbol{\delta})_\times & \mathbf{V} \\ 0 & 1 \end{bmatrix} \tag{4.1}$$

with $(\boldsymbol{\Omega} + \mathbf{b} + \boldsymbol{\delta})$ the measured angular velocity from the gyroscope including its bias $\mathbf{b}$ and noise $\boldsymbol{\delta}$. Additionally, $(\cdot)_\times$ denotes the skew-symmetric matrix associated with the cross product by itself.

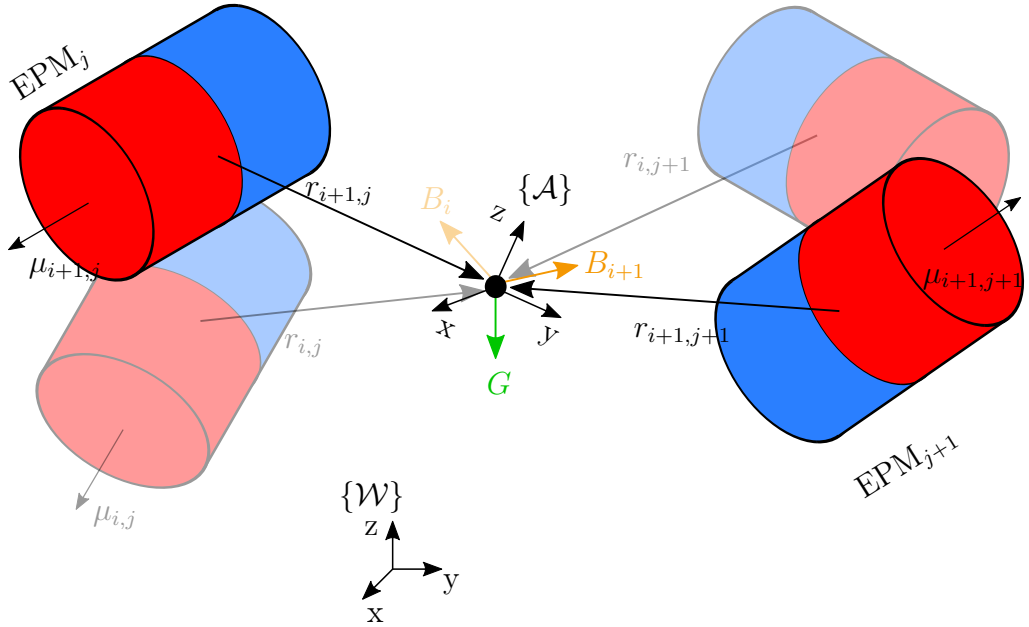

Figure 4.1: Representation of the world reference frame $\{\mathcal{W}\}$ and MAMR reference frame $\{\mathcal{A}\}$, together with gravity vector G in green, and magnetic field measurements B_i in orange for m EPMs. In purple is the state to estimate.

4.2.2 Measurement Model

We consider our MAMR to be under m EPMs actuation, and to be fitted with an accelerometer and a 3D HE sensor, providing two types of measurements: acceleration, and magnetic field vector.

Considering that gravitational acceleration ($\mathbf{g}$) dominates over linear accelerations as per common approach in literature [25; 26], the accelerometer measurement can be repre-

sented as (see Fig. 4.1 in green)

$$\mathbf{G} = R^T \mathbf{g} \tag{4.2}$$

where R^T denotes the transpose of the MAMR's rotation matrix.

The magnetic field vector generated by an EPM$_j$ (with $j = 1, ..., m$) can be modeled as a dipole

$$\mathbf{B}_j := \mathbf{B}(\mu_j, \mathbf{r}_j) = \frac{\mu_0 |\mu_j|}{4\pi |\mathbf{r}_j|^3} \left(3\hat{\mathbf{r}}_j \hat{\mathbf{r}}_j^T - I\right) \hat{\mu}_j \tag{4.3}$$

with $\mathbf{r}_j$ the distance between $\{\mathcal{A}\}$ and EPM$_j$, and μ_j the EPM's magnetic moment in $\{\mathcal{A}\}$. This assumption is valid for far-enough distances from the EPMs and is commonly employed in other magnetic localization works [30; 16]. Assuming that there are no metal objects in the workspace, the measured magnetic field $\mathbf{B}$ equals the sum of the magnetic fields generated by each EPM.

$$\mathbf{B} = \sum_{j=1}^{m} \mathbf{B}_j \tag{4.4}$$

Given the absence of the Earth's magnetic field measurement, a minimum of two magnetic field measurements for different configurations of the m EPMs are needed for observability (see Fig. 4.1 in orange, and Section 4.3.1). This is a valid assumption for systems where the magnetic field changes much quicker than the MAMR's pose, such as static or quasi-static systems. This being so, assuming null mean Gaussian measurement noises [25], the measurement model can be expressed as follows. In addition to n measurements of the magnetic field, their norm $\|\mathbf{B}_i\|$ was also included. Unlike the full magnetic field measurement vector, which contains information on both position and orientation, the magnetic field norm is dependent only on the MAMR's position. When multiple measurements are

present, the addition of the magnetic field norm increased convergence speed.

$$\mathbf{h} = \begin{bmatrix} \|\mathbf{B}_1\| \\ \vdots \\ \|\mathbf{B}_i\| \\ \mathbf{B}_1 \\ \vdots \\ \mathbf{B}_i \\ \mathbf{G} \end{bmatrix}, \qquad i = 2, \ldots, n \tag{4.5}$$

4.2.3 Extended Kalman Filter

Extended Kalman Filters (EKF) in $SO(3)$ and $SE(3)$ have been widely used and proved effective [26; 28]. For the sake of summary, only the EKF equations are explicitly described here. Further detail on the formulation of EKF can be found in [26] and [31].

The discrete dynamics of the estimated state can be described as

$$\hat{T}_{k+1} = \hat{T}_k \exp(\mathrm{K}_k \tilde{\mathbf{y}}_k t) \tag{4.6}$$

$$\tilde{\mathbf{y}}_k = \mathbf{y}_k - \mathbf{h}(\hat{T}_k) \tag{4.7}$$

with time-step $k = 0, t, 2t, ...$, K_k the gain defined by the standard EKF prediction and update steps below, $\exp(\cdot)$ the exponential map of $SE(3)$, $\mathbf{h}$ the measurement model defined in eq.(4.5), and $\mathbf{y}_k$ the sensors' outputs in the measurement model format, i.e. the norm of the magnetic field, followed by the magnetic field and gravity.

4.2.3.1 Prediction

This step sees the propagation of the state covariance matrix $P_k \in \mathbb{R}^{6\times6}$ as

$$P_k = F_k \overline{P}_{k-1} F_k^T + G_k Q_n G_k^T$$

with $P_k = \text{diag}(P_{k_p}, P_{k_R})$, where P_{k_p} and P_{k_R} denote the state covariance matrix of the position and orientation respectively. Additionally, input noise is considered as a null-mean Gaussian distribution with constant covariance $Q_n \in \mathbb{R}^{6\times6}$. Lastly, $F_k = \exp(A_k t)$ and $G_k = T_k \frac{\partial}{\partial A_k}\exp(A_k t)$, with A_k defined by the Lie algebra as matrix $A_k = [\Omega_\times \quad V; 0 \quad 0]$.

4.2.3.2 Update

The second step sees the computation of the gain K_k used in the update of the state as shown in eq. (4.6) through

$$\begin{aligned} S_k &= H_k P_k H_k^T + R_n \\ K_k &= P_k H_k^T S_k^{-1} \\ \overline{P}_k &= P_k - K_k S_k K_k^T \end{aligned}$$

where $H_k = \frac{\partial \mathbf{h}_k}{\partial T_k}$. Additionally, measurement noise is considered as a null-mean Gaussian distribution with constant covariance matrix $R_n \in \mathbb{R}^{m\times m}$ - $\mathbf{h} \in \mathbb{R}^m$.

4.2.4 Error metrics:

The observer's performance was assessed through two different error metrics: one for the estimation of the MAMR's position and one for the MAMR's attitude.

$$\begin{aligned} \text{e}_p &= \|\mathbf{p} - \hat{\mathbf{p}}\| \\ \text{e}_R &= \text{tr}(I - \hat{R}^T R) \end{aligned} \tag{4.8}$$

4.3 Simulation

To infer the stability and performance of the observer, first, an observability analysis on the system was done to assess the minimum number of magnetic field measurements for observability. Second, the impact the number of EPMs m and the maximum number of magnetic field measurements n in the measurement model (see eq. (4.4) and (4.5)) have on the stability of the observer was analyzed. Lastly, the observer was run within a simulated environment to infer the EKF's performance and expected convergence time. EKF covariance matrices P_0, Q_n and R_n were tuned in this step.

The number of EPMs was varied between one and six. Given that EPMs are used for actuation, localization should not rely on a specific EPM motion. Therefore, random motion paths were generated for each EPM. Additionally, each EPM was constrained to a plane 15 cm away from the workspace edge, as seen in Fig. 4.2.

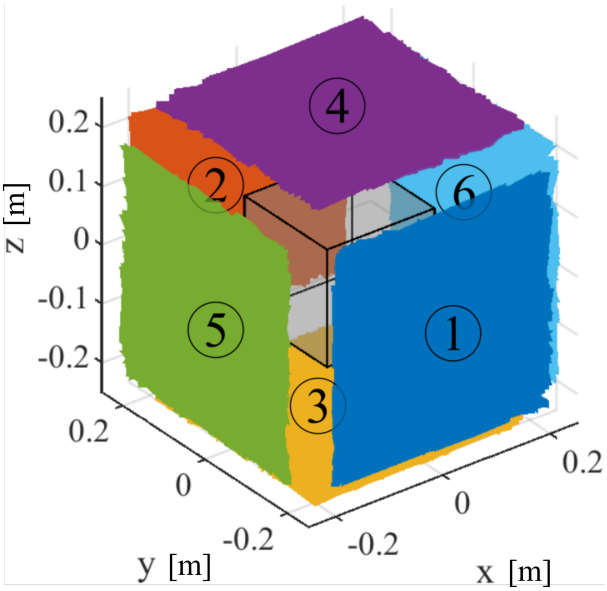

Figure 4.2: Planes covered by the generated EPM paths. Each EPM is constrained to a plane 15 cm from the workspace edge.

4.3.1 Observability Analysis

To predict the performance and stability of the observer, an observability analysis was performed for system in (4.1) with measurement model in (4.5). Additionally, the number

of EPMs m in the workspace and the number of magnetic field measurements n in the measurement model have on the observer was also analyzed.

Local weak observability of a non-linear system is defined by the following codistribution being full rank, i.e rank$(\nabla_T \mathcal{O}) = 6$.

$$\nabla_T \mathcal{O} = \text{span}(\{\nabla_T \mathcal{L}_T^i h, i \in \mathcal{N}^+ \cup 0\}) \tag{4.9}$$

where $\mathcal{L}_T^i h$ defines the ith-order Lie derivative of h with respect to the state T. In this work, we consider the first order derivative only, and so, this codistribution can be expanded as

$$\nabla_T \mathcal{O} = [\nabla_p \mathcal{O} \quad \nabla_R \mathcal{O}] = \begin{bmatrix} \nabla_p \mathcal{O}_{\|\mathbf{B}_1\|} & \nabla_R \mathcal{O}_{\|\mathbf{B}_1\|} \\ \vdots & \vdots \\ \nabla_p \mathcal{O}_{\|\mathbf{B}_n\|} & \nabla_R \mathcal{O}_{\|\mathbf{B}_n\|} \\ \nabla_p \mathcal{O}_{\mathbf{B}_1} & \nabla_R \mathcal{O}_{\mathbf{B}_1} \\ \vdots & \vdots \\ \nabla_p \mathcal{O}_{\mathbf{B}_n} & \nabla_R \mathcal{O}_{\mathbf{B}_n} \\ \nabla_p \mathcal{O}_{\mathbf{G}} & \nabla_R \mathcal{O}_{\mathbf{G}} \end{bmatrix} \tag{4.10}$$

making explicit the two components of the state, position and orientation, and the different types of measurement.

As shown in [26], $\nabla_R \mathcal{O}$ represents the Lie derivative with respect to the orientation. Since that the norm of the magnetic field has no orientation information, $\nabla_R \mathcal{O}_{\|\mathbf{B}_i\|}$ is equal to zero.

$$\nabla_R \mathcal{O}_{\|\mathbf{B}_i\|} = \begin{bmatrix} 0 & 0 & 0 \end{bmatrix} \tag{4.11}$$

$$\nabla_R \mathcal{O}_{\mathbf{B}_i} = \begin{bmatrix} 0 & -R_{:,3} \cdot \mathbf{B}_i & R_{:,2} \cdot \mathbf{B}_i \\ R_{:,3} \cdot \mathbf{B}_i & 0 & -R_{:,1} \cdot \mathbf{B}_i \\ -R_{:,2} \cdot \mathbf{B}_i & R_{:1} \cdot \mathbf{B}_i & 0 \end{bmatrix} \tag{4.12}$$

$$\nabla_R \mathcal{O}_G = \begin{bmatrix} 0 & R_{33} & -R_{32} \\ -R_{33} & 0 & R_{31} \\ R_{32} & -R_{31} & 0 \end{bmatrix} \tag{4.13}$$

$\nabla_p \mathcal{O}$ represents the Lie derivative with respect to the position, and can be expressed as follows. Given that IMU measurements only contain information regarding orientation, $\nabla_p \mathcal{O}_G$ is equal to zero.

$$\nabla_p \mathcal{O}_{\|\mathbf{B}_i\|} = \begin{bmatrix} \frac{\partial \|\mathbf{B}_i\|}{\partial x} & \frac{\partial \|\mathbf{B}_i\|}{\partial y} & \frac{\partial \|\mathbf{B}_i\|}{\partial z} \end{bmatrix} \tag{4.14}$$

$$\nabla_p \mathcal{O}_{\mathbf{B}_n} = \begin{bmatrix} \frac{\partial \mathbf{B}_{i_x}}{\partial x} & \frac{\partial \mathbf{B}_{i_x}}{\partial y} & \frac{\partial \mathbf{B}_{i_x}}{\partial z} \\ \frac{\partial \mathbf{B}_{i_y}}{\partial x} & \frac{\partial \mathbf{B}_{i_y}}{\partial y} & \frac{\partial \mathbf{B}_{i_y}}{\partial z} \\ \frac{\partial \mathbf{B}_{i_z}}{\partial x} & \frac{\partial \mathbf{B}_{i_z}}{\partial y} & \frac{\partial \mathbf{B}_{i_z}}{\partial z} \end{bmatrix} \tag{4.15}$$

$$\nabla_p \mathcal{O}_G = \begin{bmatrix} 0 & 0 & 0 \\ 0 & 0 & 0 \\ 0 & 0 & 0 \end{bmatrix} \tag{4.16}$$

Looking at the full observability matrix $\nabla_T \mathcal{O}$, we see that for when $n = 1$, $\text{rank}(\nabla_T \mathcal{O}) = 5$ making the system not observable. In fact, a single configuration of the EPMs and its respective magnetic field $\mathbf{B}_i$ together with its norm and G are not enough to solve the full 6-DOF pose. This can intuitively be inferred as the gravity vector measurement is able to provide 2-modes of the orientation, with the rotation around its own axis, i.e. rotation around gravity, missing [26]. Since the magnetic field vector and its norm are not linearly independent, only three of the remaining 4 modes of the pose dynamics can be solved for. Therefore, without any prior pose information, a minimum of 2 measurements of magnetic field are necessary in order to make the system observable and estimate the full 6-DOF pose. Additional measurements of the magnetic field can be taken for different EPM configurations.

To analyze the effect the number of EPMs in workspace ($1 \leqslant m \leqslant 6$) and the number of EPM configurations ($2 \leqslant n \leqslant 100$) in the measurement model, the condition number N_c was taken across multiple planes of the workspace. The condition number is defined as the

ratio between the maximum and minimum singluar values of $\nabla_T \mathcal{O}$, and, as such, lower values indicate a better conditioned system. Fig. 4.3(a) shows N_c across the XZ plane ($y = 0$) for $n = 100$ and for one, two, four, and six EPMs in the workspace, respectively. Fig. 4.3(b) plots how N_c changes when multiple EPM configurations n are added to the measurement model, for each number of EPMs. N_c was computed at three planes of the workspace XY ($z = 0$), XZ ($y = 0$, represented in (a)), and YZ ($x = 0$). As we can see, there is a significant difference between a single EPM $m = 1$ and multiple EPMs $m \geqslant 2$, with $m \geqslant 2$ having significantly lower N_c for any number of EPM configurations n. This is due to the fact that when multiple EPMs are present in the workspace, the resulting magnetic field becomes considerably less trivial, reducing the number of possible solutions for a specific measured magnetic field. However, there is no significant difference for when m increases beyond two. Additionally, N_c lowers as more EPM configurations n are added to the measurement model. However, a plateau is reached at around $n = 20$, as more EPM configurations do not lower N_c.

4.3.2 Simulated Observer

To further predict the performance of the EKF, the observer was ran with the MAMR fixed at 100 different randomly generated poses across the workspace. Convergence was deemed achieved once position error was below 5 mm in all axis, and the trace of the orientation error under 0.1, both for over 150 consecutive time-steps. Since the number of EPM configurations n in the measurement model affects the EKF's frequency due to robot movement and data acquisition time, rather than assessing speed through EKF iterations k, speed was assessed by the total number of different EPM configurations needed until convergence was reached, $n \cdot k$. The results were averaged across all 100 tested MAMR poses for each number of EPMs and EPM configurations.

Fig. 4.4 plots the results obtained. As expected from the previous condition number analysis, there is a clear distinction between a single EPM and multiple EPMs. Multiple EPMs lead to a much faster convergence needing a significantly lower total number of EPM configurations. However, the difference between two and six EPMs is marginal.

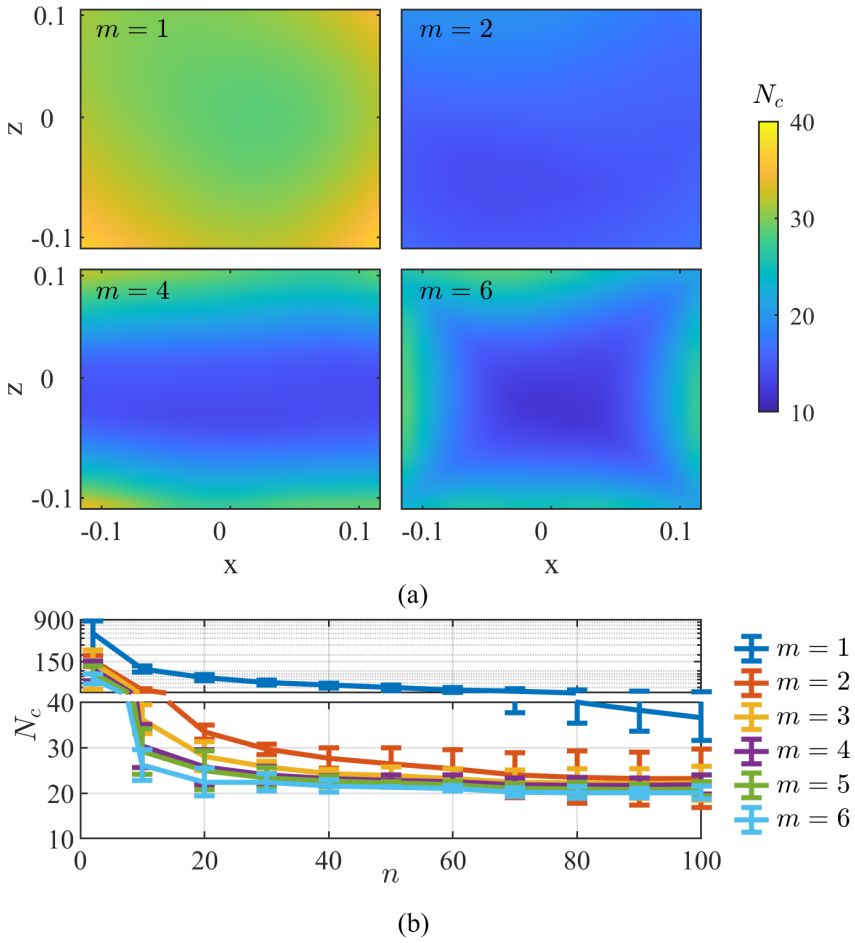

Figure 4.3: System's condition number N_c for different numbers of EPMs m and different number of EPM configurations n in the model. (a) Shows the condition number N_c across the XZ plane of the workspace for one, two, four and six EPMs, when $n = 100$. (b) Plot showing how the condition number N_c changes with higher number of EPM configurations in the measurement model for each number of EPMs.

Additionally, the higher the number of EPM configurations n in the measurement model the faster the convergence for a single EPM, as the associated N_c gets lower. However, with multiple EPMs this effect is not as noticeable, with n around 20 leading to a faster convergence.

Given these results, we consider from this point forward the case for which $m = 2$ and $n = 20$, i.e. there are two EPMs in the workspace, and the measurement model is comprised of 20 different EPM configurations. To further assess the localization performance for these conditions, a simulation was ran for 10,000 different random MAMR poses across the workspace. Fig. 4.5(a),(c) shows the error in position e_p and orientation e_R over time for all tested poses. As we can see, the observer converged for all tested poses, with 95.0%

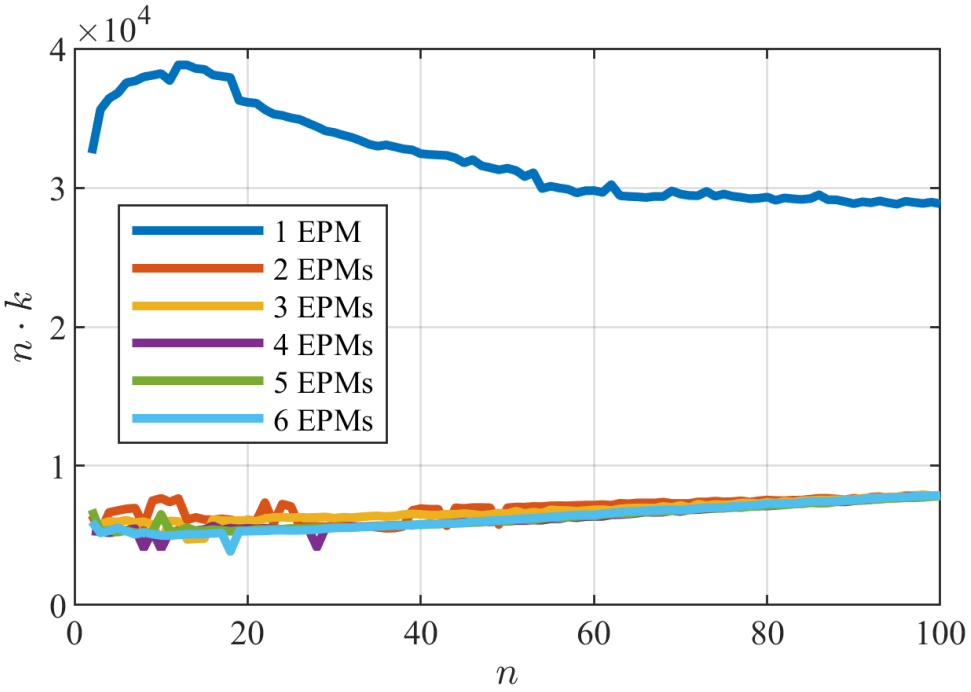

Figure 4.4: Effect that multiple EPMs and the number of EPM configurations in the measurement model n have on convergence speed $n \cdot k$. Convergence was achieved once errors in position were below 5 mm across all axis, and the trace of the orientation error e_R below 0.1, for over 150 consecutive time-steps.

of tested poses with norm position errors below 1 mm at finish. Additionally, as the histograms show, convergence in orientation is achieved faster than position, with 100% of the poses having converged fully in orientation before 1000 iterations (see Fig. 4.5(d)).

4.4 Experimental Setup

To evaluate the proposed localization system performance, a sensing platform was developed and tested with a 2-EPM system.

The sensor board was composed by a 3D IMU (LSM6DS3, STMicroelectronics, Switzerland. Accelerometer sensing range ±2g, Sensitivity 0.061mg/LSB_{16}, Footprint $2.5 \times 3 \times 0.83$ mm) and a 3D HE (MLX90395, Melexis, Belgium. Sensing range ±50 mT; Sensitivity 2.5 μT/LSB_{16}, Footprint $3 \times 3 \times 0.9$ mm). The sensors used were chosen due to their dimensions, sensitivity and sensing range, allowing their use in embedded devices of the millimeter scale under high magnetic fields. The sensors were interfaced with a

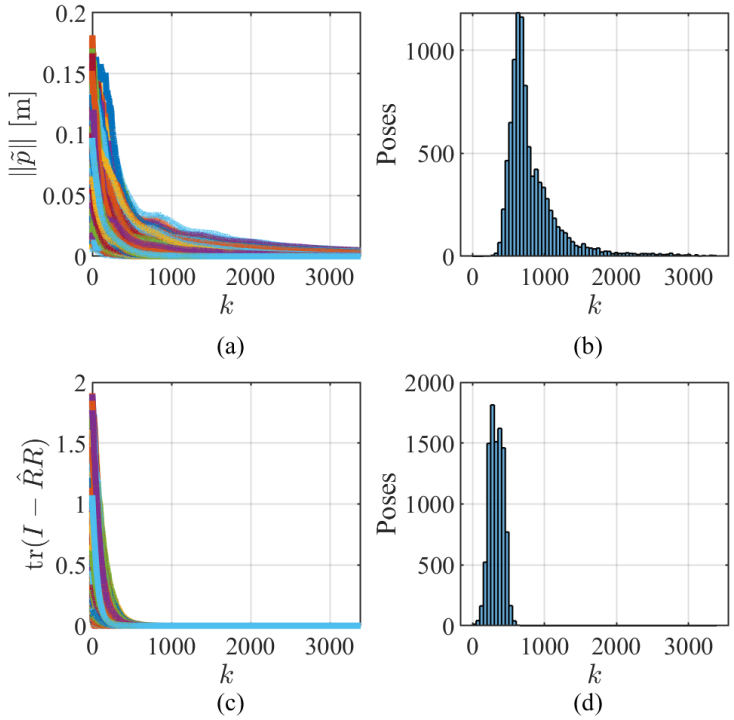

Figure 4.5: Simulation errors for 10,000 random poses across the workspace over EKF iterations, with 2 EPMs and 20 EPM configurations in the measurement model. (a) Norm of the position error, (b) Histogram showing the distribution of convergence in position, (c) Error in orientation, (d) Histogram showing the distribution of convergence in orientation.

Raspberry Pi 4B through I^2C protocol. The HE sensor was calibrated by placing it in the center of a 1D Helmholtz coil (DXHC10-200, Dexing Magnet Tech. Co., Ltd, Xiamen, China) under known magnetic field vectors.

The dual EPM platform (dEPM) was used [4; 32], consisting on two KUKA LBR iiwa14 robots (KUKA, Germany), each manipulating one EPM (cylindrical permanent magnet with diameter and lenght of 101.6 mm and axial magnetization of 970.1 Am^2 (Grade N52)) (see Fig. 4.6).

To fully assess the localization performance across the dEPM large workspace, a 3D printed plate (20-by-20 cm) was placed in between the two robots, delimiting the localization workspace in two dimensions. The sensor board was attached to 3D printed holders of various heights and orientations, which were in turn attached to the plate, allowing full variation of position and orientation.

Additionally, ground truth data was collected via a 4-camera optical tracking system

(OptiTrack, Prime 13, NaturalPoint, Inc., USA, with submilimeter accuracy). With optical markers attached to the end-effectors of both robots, to the workspace plate and to the sensor board, the relative pose of each robotic arm base and the sensor board with respect to $\{\mathcal{W}\}$ was found before each experiment (see Fig. 4.6). While the EPMs were in motion, their poses were determined by reading the robotic arms joints and computing the inverse kinematics. This ensures a more accurate tracking of the motion of the EPMs since the markers may be blocked from the field of view during the motion.

Finally, the Raspberry Pi, the robotic arms, and the optical tracking system were all connected using ROS. Data from the robotic arms encoders and sensors was collected at a rate of 50Hz. Given the inclusion of 20 EPM configurations in the measurement model, the EKF was ran at 50/20 = 2.5 Hz. The EKF parameters used are shown in Table 4.1. These were determined by the simulation step in Section 4.3.2 and the sensors used. Additionally, the state was initialized at the origin of the workspace, $T_0 = I$.

Table 4.1: EKF Covariance Matrices

	EKF
State	$P_0 = \text{diag}(10^{-4}, 10^{-4})$
Input	$Q_n = \text{diag}(10^{-5}, 10^{-3})$
Measurement $\|B\|$	$R_{n_{\|B\|}} = 10^{-8}$
Measurement B	$R_{n_B} = \text{diag}(10^{-8}, 10^{-8}, 20^{-8})$
Measurement G	$R_{n_G} = 10^{-6} I$

4.5 Results

The localization algorithm was tested for eight different poses across the workspace (see Fig. 4.7). Each pose was tested twice, with the EPMs doing a different random motion each time composed of 200 different poses.

Fig. 4.8 and 4.9 depict the error in position e_p and orientation e_R respectively, for each tested pose and repeat. The observer converged to the right solution for all tested poses with an average error of 8.5 ± 2.4 mm in position norm - with 4.14 ± 3.0 mm along the X axis, 4.13 ± 3.0 mm on the Y axis, and 3.44 ± 2.5 mm along the Z axis - and

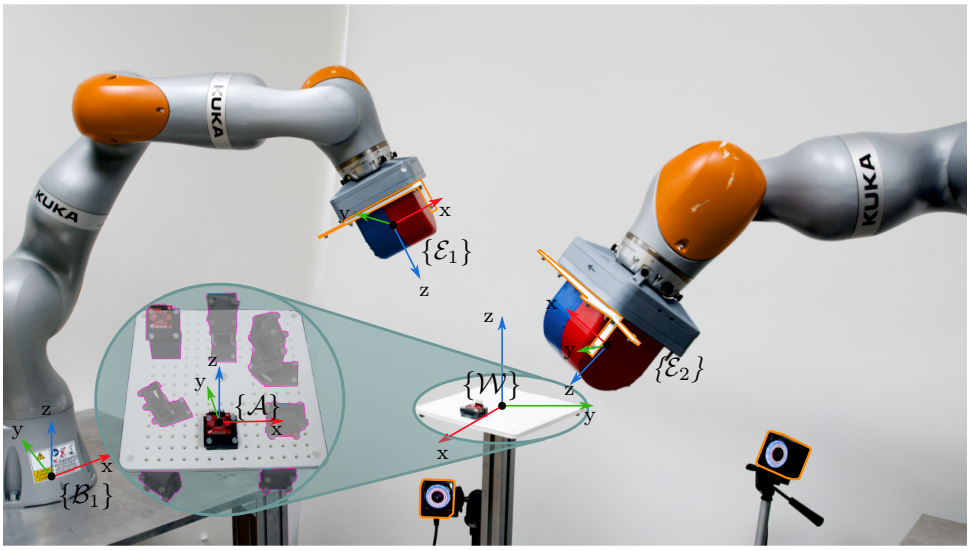

Figure 4.6: Experimental setup, comprised of two robotic arms with EPM at the end-effectors, Optical Tracking system, and sensor boards.

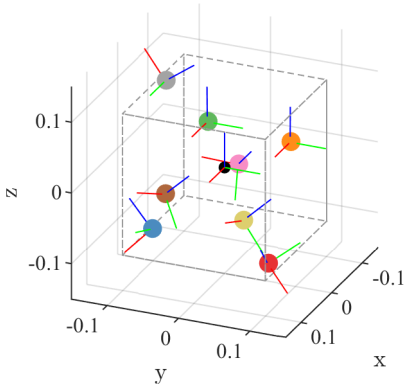

Figure 4.7: Tested poses across the workspace.

0.032 ± 0.027 in orientation trace error, i.e. $3.7 \pm 3.6°$.

However, as Fig. 4.8 and 4.9 show, there is significant variation in convergence speed and stability of the solution across repeats for the same pose. Given that the only difference between repeats is the EPMs motion, and therefore, the magnetic field measured by the sensors, the path each EPM takes and their combination have a big impact on the algorithm performance. This seems to be more significant for the estimation of the position than for the orientation, given that position estimation relies exclusively on magnetic field measurements. Fig. 4.8(c) illustrates this effect very clearly, where for repeat 1 the algorithm converged to the right solution only to start diverging towards the end, and repeat 2 took longer to converge than all other cases. Unlike localization with

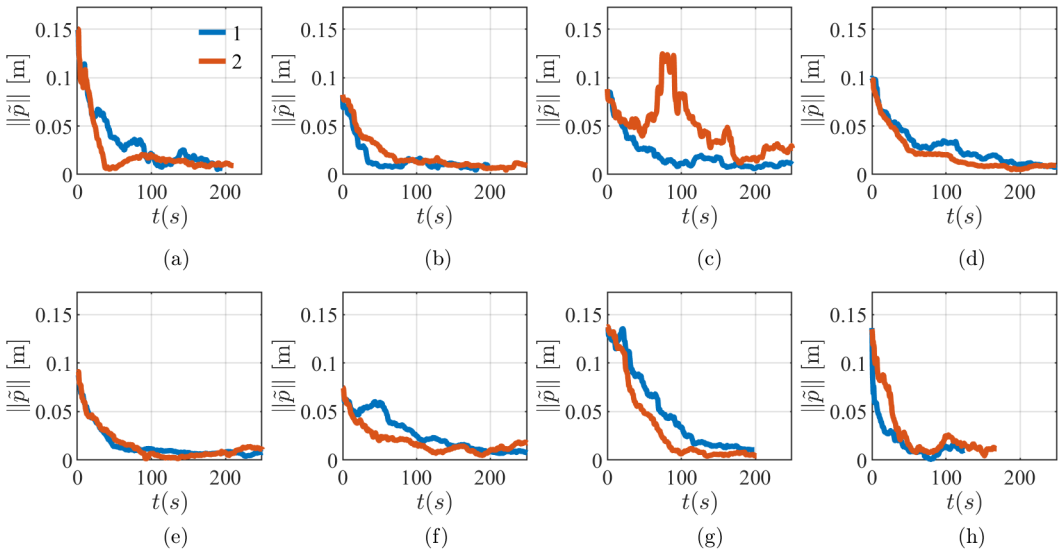

Figure 4.8: Error in position estimation for the eight tested poses across the workspace. Two repeats for each pose were performed.

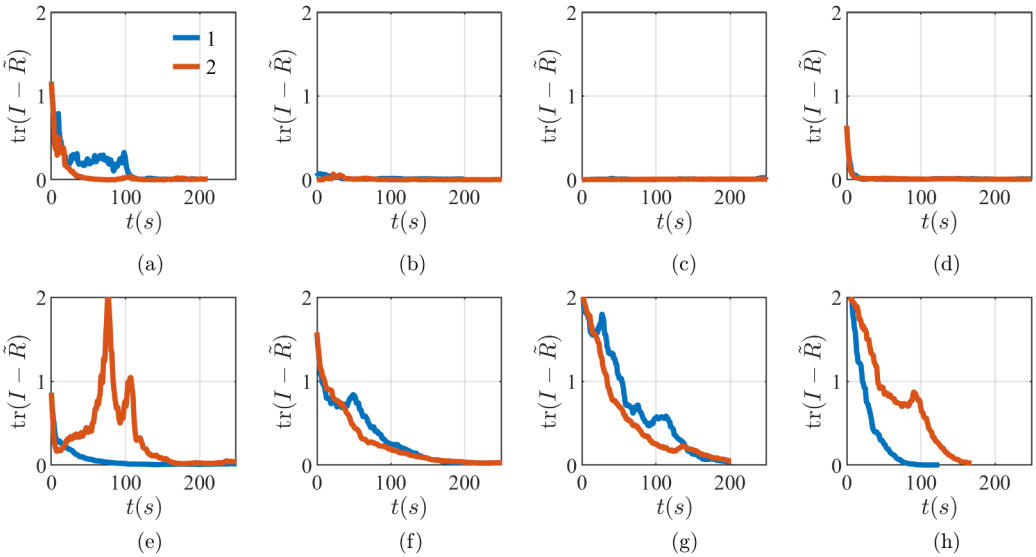

Figure 4.9: Error in orientation estimation for the eight tested poses across the workspace. Two repeats for each pose were performed.

a single EPM where the localization singularity plane is well defined and known, when multiple EPMs are present in the workspace, their relative pose dictates whether there are singularity regions and where they are. Since the EPMs are travelling random paths, it is possible that at times the sensors were located in a singularity region. Given the presence of multiple EPM configurations at each iteration of the observer, this does not seem to impact convergence but rather convergence speed. If the measurement model contained only a single configuration of EPMs, ideal for fast moving MAMR, these singularity

conditions would need to be well defined and avoided.

To test the observer's behavior in non-static conditions two different scenarios were tested. First, to address periodic motions such as breathing, linear and angular velocities were given to the world reference frame $\{\mathcal{W}\}$ in the previous set of experiments as to mimic MAMR motion. The obtained results are shown in Fig. 4.10. Linear velocities of up to 0.1 mm/s and angular velocities up to 2 °/s produced marginal differences when compared to the static cases. Velocities above these values had significant impact on the results. Second, the observer's robustness for occasional spike movements such as coughing was tested. Spikes of 5 cm of up to 4 seconds, and spikes of 10 cm of up to 2 seconds did not produce significant changes in results. Longer spike times made the results unreliable. These values, however, are highly dependent on the platform. In this case, the robotic arms were operating at 30% of their full speed for safety reasons. Increasing this speed, and/or including less EPM configuratios in the measurement model, would allow faster MAMR speeds and longer spike motions.

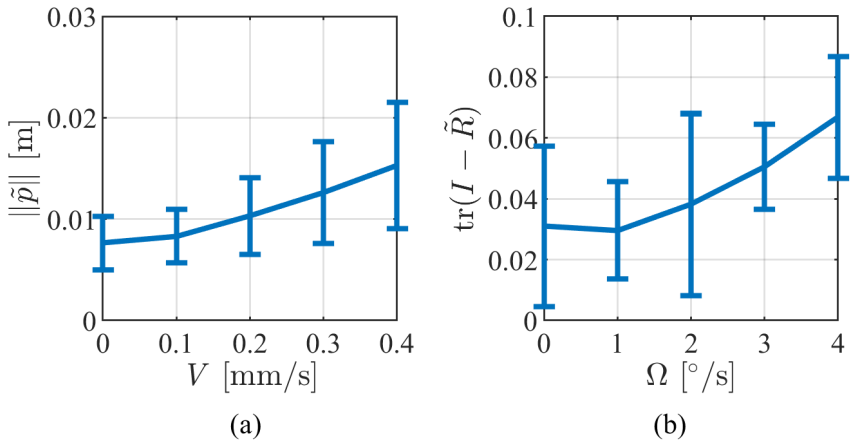

Figure 4.10: Error in (a) position and (b) orientation estimation for different linear and angular MAMR velocities.

4.6 Conclusions

In this letter, a 6-DOF localization strategy without any prior pose information for actuation systems under multiple EPMs was presented. The method relies on the measurements from a 3D accelerometer and a 3D HE sensor. These sensors are low-cost

and widely available. Additionally, their small footprint makes them easily embedded in small-scale medical robots. In fact, magnetic localization based on these sensors has long been in use in medical robots, ranging from catheters [19] to endoscopic capsules [16]. However, as new platforms based on multiple EPMs emerge for the control and actuation of magnetically actuated continuum robots for endoluminal procedures, localization techniques that take into account multiple magnetic field sources are needed. The internal placement of the sensors to the MAMR should be carefully designed to better offset any internal magnetic field measurements from the sensor. This will ensure accurate external magnetic field readings.

Unlike previous work that shows localization with respect to a single EPM, in this work we developed a localization technique under multiple EPM control. We showed that, when compared to a single EPM, multiple EPMs lead to faster convergence speeds. The method was tested across a 8000 cm^3 workspace, with average errors of 8.5 ± 2.4 mm in position norm and 0.032 ± 0.027 in orientation trace error. This localization technique can thus be applied to endoscopic capsules, or magnetically guided catheters, which are under MMFS control or in close proximity to additional magnetic field sources.

In this work, the EPMs were moved randomly around the workspace, as their movement should be mainly optimized for actuation. However, this was shown to lead to localization singularity regions and varying results when it comes to convergence speed and error. Optimizing the EPM paths for both actuation and localization for active sensing will allow for reliable simultaneous localization and actuation under multiple EPM control. This could be achieved by analysing each specific EPM configuration required for actuation, and finding an alternative whenever such a configuration leads to non-observability. Additionally, this would allow a reduction in the number of measurements needed per time step, increasing the state estimation update rate and convergence speed.

Lastly, the speed at which the EPMs are moving is crucial for the convergence speed of the observer, as well as, the MAMR's speed. Due to multiple instances of the EPM configurations present in the measurement model, a significant change in magnetic field

should be captured across different EPM configurations. With the robotic arms moving at 30% of their full speed and 20 EPM configurations per iteration, the observer was running at 2.5 Hz allowing MAMR's speeds of up to 0.2 mm/s. The robotic arms speed was constrained for safety reasons due to the random motion travelled. It is expected that in a realistic operative scenario, the robotic arms would be travelling well-defined trajectories allowing for faster safe speeds. This would allow faster update rates and MAMR's speeds.

Bibliography

[1] W. Hu, G. Z. Lum, M. Mastrangeli, and M. Sitti, "Small-scale soft-bodied robot with multimodal locomotion," *Nature*, vol. 554, no. 7690, pp. 81–85, 2018.

[2] K. M. Popek, T. Schmid, and J. J. Abbott, "Six-degree-of-freedom localization of an untethered magnetic capsule using a single rotating magnetic dipole," *IEEE Robotics and Automation Letters*, vol. 2, no. 1, pp. 305–312, 2016.

[3] S. Salmanipour and E. Diller, "Eight-degrees-of-freedom remote actuation of small magnetic mechanisms," in *2018 IEEE international conference on robotics and automation (ICRA)*, pp. 3608–3613, IEEE, 2018.

[4] G. Pittiglio, M. Brockdorff, T. da Veiga, J. Davy, J. H. Chandler, and P. Valdastri, "Collaborative magnetic manipulation via two robotically actuated permanent magnets," *IEEE Transactions on Robotics*, 2022.

[5] B. J. Nelson, S. Gervasoni, P. W. Chiu, L. Zhang, and A. Zemmar, "Magnetically actuated medical robots: An in vivo perspective," *Proceedings of the IEEE*, 2022.

[6] F. Carpi and C. Pappone, "Stereotaxis niobe® magnetic navigation system for endocardial catheter ablation and gastrointestinal capsule endoscopy," *Expert review of medical devices*, vol. 6, no. 5, pp. 487–498, 2009.

[7] F. Bianchi, A. Masaracchia, E. Shojaei Barjuei, A. Menciassi, A. Arezzo, A. Koulaouzidis, D. Stoyanov, P. Dario, and G. Ciuti, "Localization strategies for

robotic endoscopic capsules: a review," *Expert review of medical devices*, vol. 16, no. 5, pp. 381–403, 2019.

[8] L. Barducci, G. Pittiglio, J. C. Norton, K. L. Obstein, and P. Valdastri, "Adaptive dynamic control for magnetically actuated medical robots," *IEEE robotics and automation letters*, vol. 4, no. 4, pp. 3633–3640, 2019.

[9] J. C. Norton, P. R. Slawinski, H. S. Lay, J. W. Martin, B. F. Cox, G. Cummins, M. P. Desmulliez, R. E. Clutton, K. L. Obstein, S. Cochran, *et al.*, "Intelligent magnetic manipulation for gastrointestinal ultrasound," *Science robotics*, vol. 4, no. 31, p. eaav7725, 2019.

[10] A. Aziz, S. Pane, V. Iacovacci, N. Koukourakis, J. Czarske, A. Menciassi, M. Medina-Sánchez, and O. G. Schmidt, "Medical imaging of microrobots: Toward in vivo applications," *ACS nano*, vol. 14, no. 9, pp. 10865–10893, 2020.

[11] S. Pane, G. Faoro, E. Sinibaldi, V. Iacovacci, and A. Menciassi, "Ultrasound acoustic phase analysis enables robotic visual-servoing of magnetic microrobots," *IEEE Transactions on Robotics*, vol. 38, no. 3, pp. 1571–1582, 2022.

[12] H. Daguerre, S. O. Demir, U. Culha, F. Marionnet, M. Gauthier, M. Sitti, and A. Bolopion, "A localization method for untethered small-scale robots using electrical impedance tomography," *IEEE/ASME Transactions on Mechatronics*, 2022.

[13] I. S. Khalil, A. Adel, D. Mahdy, M. M. Micheal, M. Mansour, N. Hamdi, and S. Misra, "Magnetic localization and control of helical robots for clearing superficial blood clots," *APL bioengineering*, vol. 3, no. 2, p. 026104, 2019.

[14] D. Son, X. Dong, and M. Sitti, "A simultaneous calibration method for magnetic robot localization and actuation systems," *IEEE Transactions on Robotics*, vol. 35, no. 2, pp. 343–352, 2019.

[15] G. Shao, Y. Tang, L. Tang, Q. Dai, and Y.-X. Guo, "A novel passive magnetic localization wearable system for wireless capsule endoscopy," *IEEE Sensors Journal*, vol. 19, no. 9, pp. 3462–3472, 2019.

[16] A. Z. Taddese, P. R. Slawinski, M. Pirotta, E. De Momi, K. L. Obstein, and P. Valdastri, "Enhanced real-time pose estimation for closed-loop robotic manipulation of magnetically actuated capsule endoscopes," *The International journal of robotics research*, vol. 37, no. 8, pp. 890–911, 2018.

[17] M. M. Micheal, A. Adel, C.-S. Kim, J.-O. Park, S. Misra, and I. S. Khalil, "2d magnetic actuation and localization of a surface milli-roller in low reynolds numbers," *IEEE Robotics and automation letters*, vol. 7, no. 2, pp. 3874–3881, 2022.

[18] A. J. Sperry, J. J. Christensen, and J. J. Abbott, "Six-degree-of-freedom localization with a 3-axis accelerometer and a 2-axis magnetometer for magnetic capsule endoscopy," *IEEE Robotics and Automation Letters*, vol. 7, no. 2, pp. 2110–2115, 2022.

[19] C. Fischer, Q. Boehler, and B. J. Nelson, "Using magnetic fields to navigate and simultaneously localize catheters in endoluminal environments," *IEEE Robotics and Automation Letters*, 2022.

[20] M. P. Kummer, J. J. Abbott, B. E. Kratochvil, R. Borer, A. Sengul, and B. J. Nelson, "Octomag: An electromagnetic system for 5-dof wireless micromanipulation," *IEEE Transactions on Robotics*, vol. 26, no. 6, pp. 1006–1017, 2010.

[21] M. C. Hoang, K. T. Nguyen, V. H. Le, J. Kim, E. Choi, B. Kang, J.-O. Park, and C.-S. Kim, "Independent electromagnetic field control for practical approach to actively locomotive wireless capsule endoscope," *IEEE Transactions on Systems, Man, and Cybernetics: Systems*, vol. 51, no. 5, pp. 3040–3052, 2019.

[22] A. Hong, A. J. Petruska, A. Zemmar, and B. J. Nelson, "Magnetic control of a flexible needle in neurosurgery," *IEEE Transactions on Biomedical Engineering*, vol. 68, no. 2, pp. 616–627, 2020.

[23] P. Ryan and E. Diller, "Magnetic actuation for full dexterity microrobotic control using rotating permanent magnets," *IEEE Transactions on Robotics*, vol. 33, no. 6, pp. 1398–1409, 2017.

[24] I. Tunay, "Method and apparatus for dynamic magnetic field control using multiple magnets." US 7,772,950 B2, 2010.

[25] R. Mahony, T. Hamel, and J.-M. Pflimlin, "Nonlinear complementary filters on the special orthogonal group," *IEEE Transactions on automatic control*, vol. 53, no. 5, pp. 1203–1218, 2008.

[26] G. Pittiglio, S. Calo, and P. Valdastri, "On the observability and observer design on the special orthogonal group based on partial inertial sensing," *IEEE Transactions on Automatic Control*, 2020.

[27] C. Di Natali, M. Beccani, N. Simaan, and P. Valdastri, "Jacobian-based iterative method for magnetic localization in robotic capsule endoscopy," *IEEE Transactions on Robotics*, vol. 32, no. 2, pp. 327–338, 2016.

[28] S. Mathavaraj and E. A. Butcher, "Se (3)-constrained extended kalman filtering for rigid body pose estimation," *IEEE Transactions on Aerospace and Electronic Systems*, vol. 58, no. 3, pp. 2482–2492, 2021.

[29] C. G. Mayhew, R. G. Sanfelice, and A. R. Teel, "On quaternion-based attitude control and the unwinding phenomenon," in *Proceedings of the 2011 American Control Conference*, pp. 299–304, IEEE, 2011.

[30] A. J. Petruska and J. J. Abbott, "Optimal permanent-magnet geometries for dipole field approximation," *IEEE transactions on magnetics*, vol. 49, no. 2, pp. 811–819, 2012.

[31] T. D. Barfoot, *State estimation for robotics*. Cambridge University Press, 2017.

[32] G. Pittiglio, P. Lloyd, T. da Veiga, O. Onaizah, C. Pompili, J. H. Chandler, and P. Valdastri, "Patient-specific magnetic catheters for atraumatic autonomous endoscopy," *Soft Robotics*, 2022.

Chapter 5

Dynamic Localization for Magnetically Actuated Robots

Chapter source: T. da Veiga, M. Brockdorff, G. Pittiglio, J. H. Chandler, and P. Valdastri, "Magnetic Localization in Case of Manipulation by Two Robotized Permanent Magnets", The International Journal of Robotics Research, Under Review - submitted June 2023

Abstract

Localization methods for magnetically actuated medical robots have long been a topic of research, as they are fundamental to closed loop control and delivery of functionalities. However, magnetic localization has mainly been linked to robots under a single permanent magnet control. With the release of multi-magnet actuation systems for increased control and manipulability, new locazation methods are needed to account for the added magnetic field sources. This paper presents a six degree of freedom localization method for magnetically actuated robots under two external permanent magnets control. The approach relies on the measurements of an accelerometer and gyroscope for the estimation of orientation in the Special Orthogonal Group SO(3), and the measurements of the actuating magnetic fields for the estimation of position. The observability analysis of

the system is presented, and the relationship between the external permanent poses and conditioning of the system is explored. Additionally, a calibration procedure to determine the relative poses between the two external permanent magnets is presented where the path that the magnets travel is optimized for the best results. Lastly, the localization method was implemented in a magnetic soft continuum robot and achieved positional average errors of 3.5 mm in norm, and orientation errors of 2.5 °, 1.5 ° and 2.8 ° around x, y, and z, respectively.

5.1 Introduction

Medical and surgical robots have seen significant development over recent decades as they are able to reduce procedural times and learning curves for clinicians, and increase patient comfort through less bleeding and scarring. Specifically, magnetically actuated medical robots (MAMR) have sparked increased interest as they allow for remote actuation and miniaturization without loss of controllable degrees of freedom (DOF) [1; 2; 3; 4; 5]. Additionally, the development of soft magnetic continuum robots (SCR) capable of reaching deeper inside the human body in a safe and autonomous manner, have further advanced the state of minimally invasive robotic surgery [6; 7; 8].

Given the high non-linearity of magnetic fields, localization of such robots is fundamental to ensure accurate actuation and manipulation, in addition to enabling closed loop control [9; 10; 11], autonomous navigation [12], and delivery of functionality [13]. However, the majority of commercially available localization systems are either not compatible with magnetic actuation (e.g. electro-magnetic tracking) or rely on imaging methods, such as fluoroscopy [14] or ultrasound [15]. As such, the topic of localization of magnetic robots has been heavily researched and developed [16; 17], with significant work on achieving both actuation and localization using the same magnetic fields [18; 19; 20; 21; 22].

Magnetic actuation can be achieved by either coil-based or permanent magnet (PM)-based platforms, with localization strategies for both having been reported [14; 23]. While coil-based systems have the advantage of readily generating linear field changes, they re-

quire high power and generally suffer from restricted workspace dimensions. PM based platforms however, offer large scale actuation while maintaining low running costs. Localization strategies for PM-based platforms have been largely developed for single external permanent magnet (EPM) systems [19]. With the advent of magnetic navigation platforms based on multiple PMs [24], such as the FDA approved Steoreotaxis Genesis RMN® [25], the dual External Permanent Magnet (dEPM) platform [4], or multiple rotating PMs [26], fluoroscopy is still the standard practice as localization for such platforms has been lacking [27]. New localization methods that are able to consider additional PMs and the resulting non-linear magnetic fields are needed. It was not until recently, a 3D position magnetic localization system was demonstrated under optimized magnetic field gradients [21], and an additional feasibility study on using an array of magnetic field sensors for the full six DOF localization [28]. Alternative methods that are miniaturizable rely on minimal sensing and are compatible with multiple magnetic field sources are needed.

The use of an inertial measurement unit (IMU) containing an accelerometer and gyroscope, together with an array of magnetic field sensors has been shown effective in the 6-DOF pose estimation of a capsule controlled by a single EPM via magnetic coupling [19; 29]. Taddese *et al.* managed to correct the gyroscope bias and to eliminate the EPM singularity region by fitting an electromagnetic coil generating a low-intensity time-varying orthogonal magnetic field. While this approach is notable for magnetic coupling actuation single EPM systems, it is not applicable to multi-EPM systems for generic magnetic field actuation. These systems suffer from not well defined and variable singularity regions depending on the relative pose between the EPMs. Therefore, a minimum of two coils generating two different low-intensity time-varying magnetic fields would be needed to eliminate the EPMs singularity regions. This would make the measuring of magnetic fields from the EPMs redundant, and no longer require the actuation fields for localization, but rather generating additional localization magnetic fields on top the actuation fields. From a practical perspective, several considerations would need to be made to ensure that such low intensity fields would not actuate the MAMR while

still being easily and accurately measured by the embedded magnetic field sensors. As such, alternative methods should be considered when designing localization methods for multi-EPM systems, while still relying on the actuation magnetic fields for measurement.

In our previous work, we investigated the feasibility of magnetic localization with respect to multiple EPMs for quasi-static systems [22]. In this work, we introduce a real-time 6-DOF pose estimation algorithm for MAMR under dual EPM control, based on a 3D accelerometer, 3D gyroscope, and a single 3D magnetic field sensor. We define the singularity regions based on the relative motion of two EPMs which should be avoided during actuation and localization. The localization algorithm was tested on a soft continuum robot (SCR) under actuation in the dEPM platform, where alternative EPM configurations were provided as not to lose controllability.

5.2 Observability Analysis

We consider finding the pose of a MAMR, with frame $\{\mathcal{A}\}$ within the workspace of a dual EPM platform with reference frame $\{\mathcal{W}\}$ (see Fig. 5.1). We consider the EPMs to be cylindrical and axially magnetized, and that the MAMR is fitted with a 3D accelerometer, 3D gyroscope, and a 3D Hall effect (HE) magnetic field sensor.

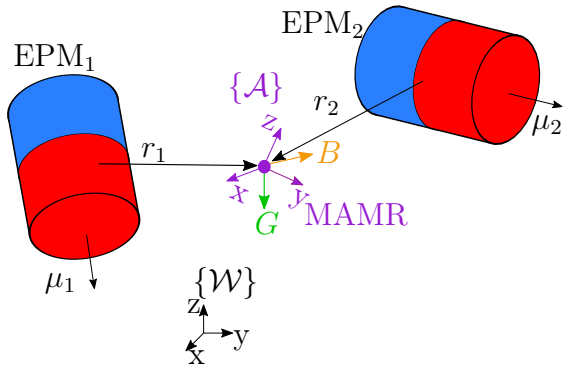

Figure 5.1: Representation of the world reference frame $\{\mathcal{W}\}$ and MAMR reference frame $\{\mathcal{A}\}$, together with gravity vector G in green, and magnetic field measurement B in orange.

The angular velocity measured by the gyroscope $\mathbf{\Omega}$ can be modelled as

$$\mathbf{\Omega} = \boldsymbol{\omega} + \mathbf{b} + \boldsymbol{\delta} \tag{5.1}$$

where $\boldsymbol{\omega}$ represents the MAMR's angular velocity expressed in $\{\mathcal{W}\}$ relative to $\{\mathcal{A}\}$, $\mathbf{b}$ the gyroscope bias, and $\boldsymbol{\delta}$ the measurement noise.

The accelerometer measures the MAMR's linear acceleration and its output can be expressed as

$$\mathbf{A} = R^T(\mathbf{g} + \mathbf{a} + \boldsymbol{\sigma}) \tag{5.2}$$

where R denotes the rotation matrix mapping the MAMR's orientation in $\{\mathcal{W}\}$, $\mathbf{g}$ denotes the gravity vector in $\{\mathcal{W}\}$, $\mathbf{a}$ other components of the linear acceleration, and $\boldsymbol{\sigma}$ the measurement noise.

Lastly, assuming that there are no metal objects in the workplace, the magnetic field measurement $\mathbf{B}$ is the sum of the magnetic fields generated by each individual EPM as

$$\mathbf{B} = \mathbf{B}_1 + \mathbf{B}_2 + \boldsymbol{\eta} \tag{5.3}$$

with $\boldsymbol{\eta}$ denoting measurement noise. Additionally, the magnetic field generated by each EPM i can be modelled by the following equation as per other works in the field [19].

$$\mathbf{B}_i = \frac{\mu_0|\boldsymbol{\mu}_i|}{4\pi|\mathbf{r}_i|^3}(3\hat{\mathbf{r}}_i\hat{\mathbf{r}}_i^T - I)\hat{\boldsymbol{\mu}}_i \tag{5.4}$$

with $\mathbf{r}_i$ the distance between $\{\mathcal{A}\}$ and EPM$_i$, μ_i the EPM's magnetic moment in $\{\mathcal{A}\}$, and μ_0 vacuum's magnetic permeability. This model has been shown to have errors lower than 2% for distances larger than 1.5 the EPM diameter [30].

In this work, we consider $\boldsymbol{\delta}$, $\boldsymbol{\sigma}$, and $\boldsymbol{\eta}$ as null mean Gaussian noises, and gravity ($\mathbf{g}$) dominates over other linear acceleration components, as per common approach in the

literature [31]. Therefore, our measurement models can be modelled as

$$\mathbf{\Omega} = \boldsymbol{\omega} + \mathbf{b} \tag{5.5}$$

$$\mathbf{G} = R^T \mathbf{g} \tag{5.6}$$

$$\mathbf{B} = \mathbf{B}_1 + \mathbf{B}_2 \tag{5.7}$$

These considerations will be taken into account in the design of the observer in Section 5.3.4.

5.2.1 Problem Formulation in *SE(3)*

The main goal is to estimate the homogenous transformation matrix of the MAMR reference frame $\{\mathcal{A}\}$ to the global frame $\{\mathcal{W}\}$. We describe our state in the special Euclidean group $SE(3)$, i.e. the group of rigid transformations on $\mathbb{R}^3$ associated with the Lie algebra $\mathfrak{se}(3)$ of dimension 6.

$$T = {}^{\mathcal{W}}T_{\mathcal{A}} : \{\mathcal{A}\} \rightarrow \{\mathcal{W}\} \tag{5.8}$$

$$T = \begin{bmatrix} R & \mathbf{p} \\ 0_{1\times 3} & 1 \end{bmatrix} \tag{5.9}$$

where $\mathbf{p} \in \mathbb{R}^3$ denotes the MAMR's position in $\{\mathcal{W}\}$.

The overall system can thus be described as

$$\dot{T} = T \begin{bmatrix} \mathbf{\Omega}_{\times} & \mathbf{v} \\ 0_{1\times 3} & 1 \end{bmatrix} \tag{5.10a}$$

$$\mathbf{h} = \begin{bmatrix} \mathbf{B} \\ \mathbf{G} \end{bmatrix} \tag{5.10b}$$

with $\mathbf{v}$ the MAMR's linear velocity expressed in $\{\mathcal{W}\}$.

5.2.1.1 Observability Analysis

To predict the stability and performance of the observer, the observability of the system in eq. (5.10) was analysed.

Local weak observability of a non-linear system is defined by its observability co-distribution being full rank, i.e $\text{rank}(\nabla_T O) = 6$ for this case.

The system's observability co-distribution can be defined as [32]

$$\nabla_T \mathcal{O} = \text{span}(\{\nabla_T \mathcal{L}_{\dot{T}}^i \mathbf{h}, i \in \mathcal{N}^+ \cup 0\}) \tag{5.11}$$

where $\mathcal{L}_{\dot{T}}^i \mathbf{h}$ defines the ith-order Lie derivative of $\mathbf{h}$ with respect to the state T. In this work, we only consider the first order derivative, and so the system's co-distribution can be represented as

$$\nabla_T O = \begin{bmatrix} \nabla_{\mathbf{p}} O & \nabla_R O \end{bmatrix} \tag{5.12}$$

where $\nabla_{\mathbf{p}} O$ refers to the co-distribution with respect to the position, and $\nabla_R O$ the co-distribution with respect to the orientation.

The position co-distribution can be expanded into

$$\nabla_{\mathbf{p}} O = \begin{bmatrix} \frac{\partial \mathbf{B}_x}{\partial x} & \frac{\partial \mathbf{B}_x}{\partial y} & \frac{\partial \mathbf{B}_x}{\partial z} \\ \frac{\partial \mathbf{B}_y}{\partial x} & \frac{\partial \mathbf{B}_y}{\partial y} & \frac{\partial \mathbf{B}_y}{\partial z} \\ \frac{\partial \mathbf{B}_z}{\partial x} & \frac{\partial \mathbf{B}_z}{\partial y} & \frac{\partial \mathbf{B}_z}{\partial z} \\ 0 & 0 & 0 \\ 0 & 0 & 0 \\ 0 & 0 & 0 \end{bmatrix} \tag{5.13}$$

as only the magnetic field measurements are able to provide information regarding the MAMR's position.

On the other hand, both gravity and magnetic field measurements provide information

regarding the MAMR's orientation.

$$\nabla_R O = \begin{bmatrix} 0 & -R_{:,3} \cdot \mathbf{B} & R_{:,2} \cdot \mathbf{B} \\ R_{:,3} \cdot \mathbf{B} & 0 & -R_{:,1} \cdot \mathbf{B} \\ -R_{:,2} \cdot \mathbf{B} & R_{:,1} \cdot \mathbf{B} & 0 \\ 0 & R_{33} & -R_{32} \\ -R_{33} & 0 & R_{31} \\ R_{32} & -R_{31} & 0 \end{bmatrix} \tag{5.14}$$

where $R_{:,i}$ denotes the i^{th} column of matrix R. Looking at the full observability co-distribution, it can be seen that $\text{rank}(\nabla_T O) = 5$, and hence the system is not observable. This can be intuitively inferred, as the gravity vector only provides information on 2 modes of orientation, missing the rotation around gravity. This leaves a single measurement of the magnetic field to solve for the missing four state modes, i.e position and rotation around gravity.

This is a known and common conundrum in orientation estimation in environments where the Earth's magnetic field is not available. In previous our previous work, multiple measurements of the magnetic field were added [22]. However, this method is not compatible with real-time localization. Consequently, it is helpful to split the problem into two sub-problems: the estimation of the rotation matrix in $SO(3)$ and the estimation of the position in $\mathbb{R}^3$.

5.2.2 Problem Formulation in SO(3)

The goal here is to estimate the full rotation matrix of the MAMR R in $\{\mathcal{W}\}$. This state is described in the special orthogonal group SO(3), where

$$SO(3) = \{R \in \mathbb{R}^{3\times3} | R^T R = I, \det(R) = 1\} \tag{5.15}$$

where $I \in \mathbb{R}^{3\times3}$ is the identity matrix.

Since magnetic field measurements depend on both the MAMR's position and orientation, orientation will be estimated solely based on the accelerometer and gyroscope measurements. An observer previously described in [32] is applied and can be described as follows.

$$\dot{R} = R(\boldsymbol{\omega} + \mathbf{b})_{\times} \tag{5.16a}$$

$$\mathbf{h}_R = \begin{bmatrix} R^T\mathbf{g} \\ -\boldsymbol{\omega}_{\times} R^T\mathbf{g} \end{bmatrix} \tag{5.16b}$$

The state evolves over time according to the angular velocity measured from the gyroscope. The measurement model is composed by the direction of gravity measured by the accelerometer and its first derivative. This observer is able to accurately track and estimate the full orientation of a rigid body as long as some angular velocity is present in the system, independently of magnetic field measurements [32]. However, since a single inertial measurement is present, the system requires accurate initialization of the rotation around gravity. Furthermore, due to the gyroscope bias $\mathbf{b}$, the estimate is expected to drift over time. In this work, we consider $\mathbf{b}$ to be constant and offset from the measurements.

5.2.3 Problem Formulation in $\mathbb{R}^3$

Assuming the rotation matrix within the workspace is known, the main goal is now to find the MAMR's position $\mathbf{p} \in \mathbb{R}^3$ in $\{\mathcal{W}\}$. For the estimation of position, only magnetic field measurements are used as IMU measurements do not depend on the position within the workspace. This system is described in equation (5.17). The observability co-distribution for the system is full-rank making the system observable.

$$\dot{\mathbf{p}} = \mathbf{p} \cdot \mathbf{v} \tag{5.17a}$$

$$\mathbf{h}_{\mathbf{p}} = \Big[\mathbf{B}_1(\mathbf{p}) + \mathbf{B}_2(\mathbf{p})\Big] \tag{5.17b}$$

As shown previously [22], the relative pose of the EPMs highly affects the system's observability and the observer's performance. As such, Fig. 5.2 depicts the system's condition number across the workspace for the most common EPM configurations of the platform [4]. The condition number is defined as the ratio between the maximum and minimum singular values of the systems observability co-distribution matrix, and therefore, lower values indicate a better conditioned system. We can see that singularity planes and regions exist for certain configurations as shown by a high condition number. These singularity planes are characterized by unidirectional magnetic fields. Fig. 5.3 plots the magnitude of the magnetic field on these planes. For summary's sake, the singularity planes for the EPM configurations when the EPMs are magnetized along Z (Fig. 5.2(c) and (g)) were omitted as they are identical to magnetizations along X (Fig. 5.2(a) and (e)) albeit rotated by 90 degrees around the y axis.

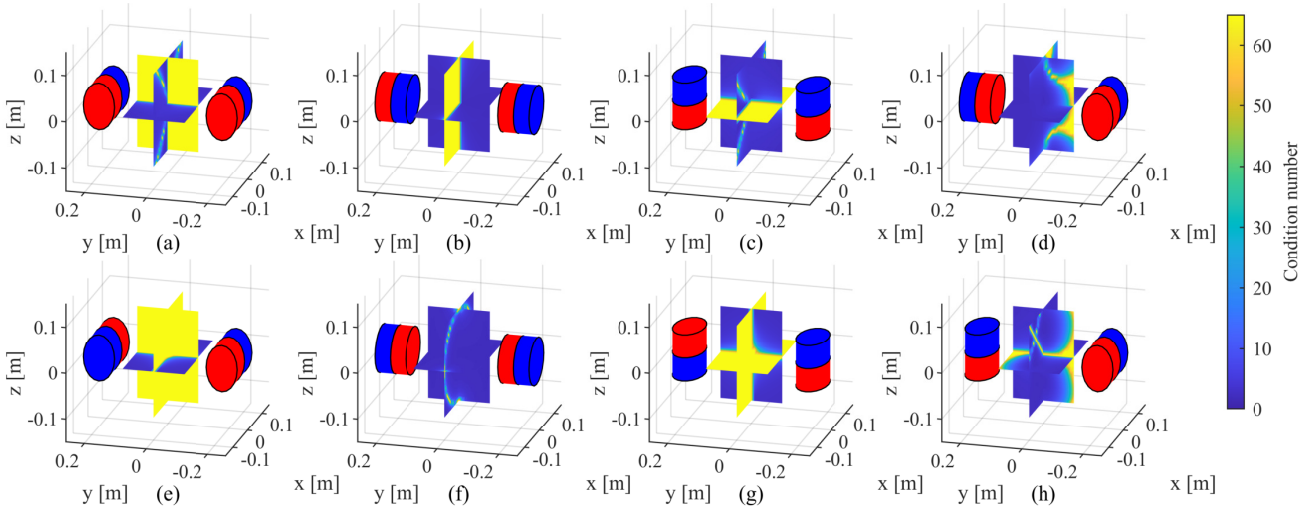

Figure 5.2: Position estimation in $\mathbb{R}^3$ condition number across the workspace for different relative poses between the EPMs. The configurations depicted in (a), (b), and (c) generate a homogenous field along the X, Y, and Z axis respectively in the workspace center. Scenarios (e), (f), and (g) generate magnetic field gradients $\partial B_x/\partial y$, $\partial B_y/\partial y$, and $\partial B_z/\partial x$ respectively in the workspace center. Configurations (d) and (h) represent orthogonal configurations of the EPMs magnetic moments.

It is known that for a single cylindrical axially-magnetized EPM, the plane orthogonal to its magnetization passing through its center is singular [19]. This plane is characterized by magnetic fields which are perfectly aligned with the magnetization of the PM. These are symmetric concentrically around the PM, and thus an infinite number of points have

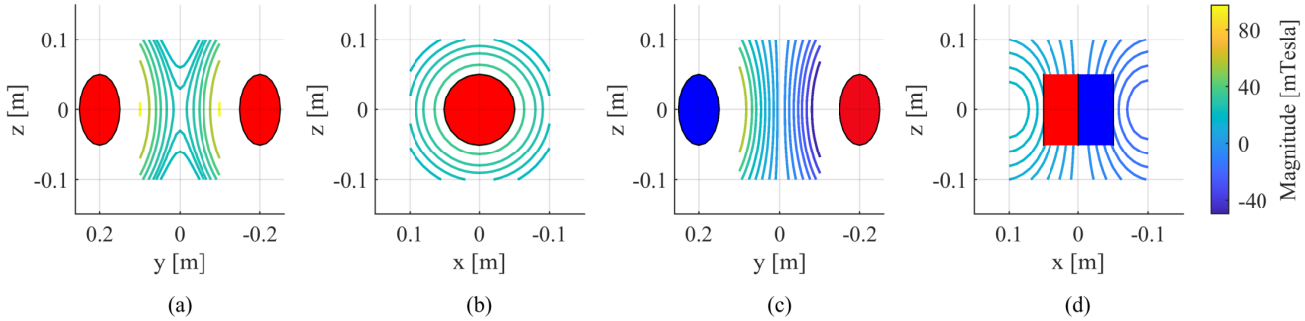

Figure 5.3: Field magnitude on singularity planes for different EPM configurations. The magnetic field on these planes is unidirectional and orthogonal to the plane, each line denoting a magnitude. (a) Homogenous field along the X axis, (b) homogenous field along the Y axis, (c) and (d) magnetic field gradient $\partial B_x/\partial y$.

the exact same magnetic field vector. This effect is replicated on the plane equidistant from two EPMs when these are perfectly aligned along their magnetisations (Fig. 5.2(b), Fig. 5.3(b)).

When two EPMs are parallel to each other (Fig. 5.2(a) and (c), and Fig. 5.3(a)), the single EPM singularity plane is still singular as the magnetic field on that plane is uniaxial and concentrically symmetric, although around two centers rather than one. Additionally, when the EPMs are parallel with their magnetizations opposed (Fig. 5.2(e) and (g)), a second singularity plane is present (Fig. 5.3(c) and (d)), as the magnetic field is also unidirectional and symmetric on the equidistant plane between the two EPMs.

These singularity planes can be mitigated by having the EPMs misaligned (Figure 5.2(d) and (h)), where only small singularity regions are present closer to each EPM singularity plane.

5.3 Experimental Setup

The proposed localization technique was evaluated on a magnetically actuated soft continuum robot (SCR), under dEPM actuation.

5.3.1 Soft Continuum Robot

The SCR featured a sensorized tip containing a 3D HE and an IMU. Figure 5.4 depicts a schematic representation of the fabrication process. Silicone rubber (Ecoflex®00-30, Smooth-On, Inc., U.S.A.) was mixed with hard magnetic micro-particles (NdFeB with an average 5 μm diameter and intrinsic coercivity of H_{ci} = 9.65 kOe, MQFP-B+, Magnequench GmnH, Germany) in a 1:1 weight ratio. The mixture was mixed and degassed in a high-vacuum mixer (ARV-310, THINKYMIXER, Japan) for 90 seconds at 1400 rpm and 20.0 kPa [33]. The elastomer was subsequently injected into a 3D printed mold and left to cure at room temperature (Fig. 5.4(a)). Once cured, the SCR was magnetized under a magnetizing field of 5.0 T using an impulse magnetizer (IM-10-30, ASC Scientific, U.S.A.).

Separately, the sensors were soldered onto 5 mm diameter circular printed circuit boards (PCBs), and then fitted into a 3D printed holder (with an outer diameter of 5.5 mm). The sensors used were chosen due to their dimensions, sensitivity and sensing range, allowing their use in small embedded devices under high magnetic fields (IMU: LSM6DS3, STMicroelectronics, Switzerland. Accelerometer sensing range ±16g, Sensitivity 0.488mg/LSB_{16}; Gyroscope sensing range ±2000mdps, sensitivity 70mdps/LSB_{16}; Hall Effect: MLX90395, Melexis, Belgium. Sensing range ±50 mT; Sensitivity 2.5 μT/LSB_{16}). This was then placed at the distal end of a second 3D printed mold together with the SCR, and then non-magnetic silicone elastomer was injected (Fig. 5.4(b)). The final SCR was 6 mm in diameter, and 80 mm in length, with an axial magnetization.

5.3.2 Sensor Calibration

Once the SCR was fabricated, the sensors were calibrated. This calibration has the main goal of finding the orientation of the ICs inside the SCR. The accelerometer was calibrated by measuring gravity along the SCR inertial axes. The gyroscope was offset by measuring its output for 10 min while stationary. The HE sensor was calibrated by placing the SCR tip in the center of a Helmholtz coil (DXHC10-200, Dexing Magnet Tech. Co., Ltd,

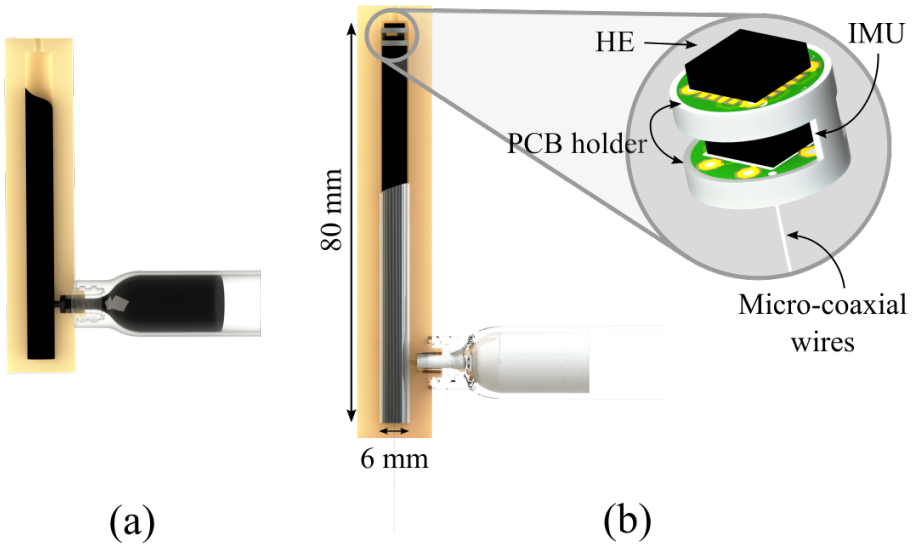

Figure 5.4: Schematic representation of the continuum robot fabrication with a sensorized tip containing an IMU and HE sensor. (a) Silicone rubber with magnetic particles is injected into a mould, (b) Sensors are held in place through a PCB holder which is embedded in the overall SCR.

Xiamen, China) under known homogeneous magnetic fields. The sensors were interfaced to a Raspberry Pi 4B through i^2c protocol.

Given that the SCR is magnetic, its effect on the measurement of the external magnetic field has to be considered. To this effect, the magnetic field measurements were offset by measuring the internal magnetic field when the SCR is under no external actuation, which was equal to 3.2 mT (see Figure 5.5(a)). The SCR was then actuated under a known external magnetic field of 9 mT in a Helmholtz coil (DXHC10-200, Dexing Magnet Tech. Co., Ltd, Xiamen, China) (see Figure 5.5(b)) where the internal magnetic field measured was of 3.1 mT. Given these results, in this work, the internal magnetic field to the SCR is considered constant.

5.3.3 Dual External Permanent Magnet Platform

The dEPM platform was used to test the localization technique [4]. This platform is comprised of two KUKUA LBR iiwa14 robots (KUKA, Germany), each manipulating one EPM (cylindrical permanent magnet with diameter and length of 101.6 mm and axial magnetization of 970.1 Am^2 (Grade N52)) (see Figure 5.6). The platform is able to

Figure 5.5: Fabricated Soft Continuum Robot (a) unactuated, (b) under a 9 mT homogeneous magnetic field.

generate magnetic fields up to 50 mT and magnetic field gradients of up to 300 mT/m at the center of the workspace. The SCR was placed in the center of the workspace with its base fixed in place at the origin, and its tip free to move.

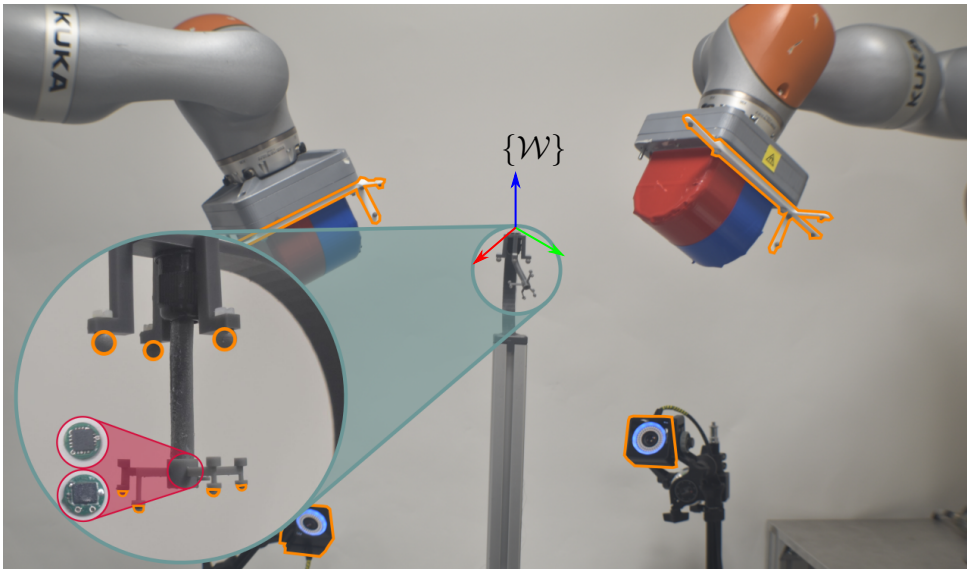

Figure 5.6: Experimental setup for the localization experiments. In orange is the optical tracker used as benchmark. In red the PCBs with the embedded sensors.

Additionally, a 4-camera optical tracking system (OptiTrack, Prime 13, NaturalPoint, Inc., USA, with submilimeter accuracy) was used for ground truth measurements. Markers were attached to the end-effectors of both robots, the workspace center and the SCR tip. Robot Operating System (ROS) was used to operate the robotic arms and to read data from sensors at 300 Hz.

5.3.4 Extended Kalman Filter

Extended Kalman Filter (EKF) has been proved effective in localization techniques [32]. Here we describe the discrete-time dynamics of the position, followed by the prediction and update steps of the EKF. For the sake of summary, we present the general form of the EKF, which was applied to estimate the orientation and the position separately.

5.3.4.1 Orientation Discrete Dynamics

The discrete dynamics of the estimated orientation $\hat{R}$ can be described as

$$\hat{R}_{k+1} = \hat{R}_k \exp(\boldsymbol{\omega}_{k_\times}) \exp((K_k \tilde{\mathbf{z}}_k)_\times) \tag{5.18a}$$

$$\tilde{\mathbf{z}}_k = \mathbf{z}_k - \mathbf{h}_R(\hat{R}_k, \boldsymbol{\omega}_k) \tag{5.18b}$$

with $k = 0,\ T,\ 2T,\ \ldots$ and K_k the Kalman gain defined below, $\exp(\cdot)$ denotes the exponential map of SO(3), $\mathbf{z}_k$ the output from the IMU, and $\mathbf{h}_R(\cdot)$ the measurement model proposed in eq. (5.16b).

5.3.4.2 Position Discrete Dynamics

The estimated position $\hat{\mathbf{p}}$ discrete dynamics are described as follows

$$\hat{\mathbf{p}}_{k+1} = \hat{\mathbf{p}}_k + K_k \tilde{\mathbf{z}}_k \tag{5.19a}$$

$$\tilde{\mathbf{z}}_k = \mathbf{z}_k - \mathbf{h}_\mathbf{p}(\hat{\mathbf{p}}_k) \tag{5.19b}$$

with $\mathbf{z}_k$ the output from the HE sensor, and $\mathbf{h}_\mathbf{p}(\cdot)$ the measurement model proposed in equation (5.17).

5.3.4.3 EKF Prediction Step

The prediction step of the EKF consists of propagating the state covariance P_k as

$$P_k = F_k \bar{P}_{k-1} F_k^T + Q_n \tag{5.20}$$

where F_k denotes the state derivative of the system dynamics, G_k the state derivative of the measurement model, and Q_n the input noise covariance matrix.

5.3.4.4 EKF Update Step

The update step computes the Kalman gain according to the following equations.

$$S_k = H_k P_k H_k^T + N_n$$

$$K_k = P_k H_k^T S_k^{-1}$$

$$\bar{P}_k = P_k - K_k S_k K_k^T$$

with N_n the measurement noise covariance matrix.

5.3.5 Error Metrics

Each observer's performance was assessed through the norm of the error. For the position observer, the norm was computed as shown in eq. (5.21).

$$\|\tilde{\mathbf{p}}\| = \|\mathbf{p} - \hat{\mathbf{p}}\| \tag{5.21}$$

For the orientation observer, the error of the whole rotation matrix was computed through eq. (5.22).

$$e_R = \text{tr}(I - \hat{R}^T R) \tag{5.22}$$

Unlike position, orientation is a bounded entity with a maximum error, $e_R \in [0, 4]$. Therefore, the orientation errors are expressed as a percentage.

5.4 Platform Calibration

In order to estimate the SCR's pose within the workspace, the dEPM platform first needs to be calibrated. Unlike single EPM platforms in which the localization algorithm

finds the relative pose between the agent and the EPM, when two or more EPMs are present, the localization is done with respect to a previously defined global reference frame. Therefore, this calibration procedure aims at defining a global reference frame and finding the relative transformation matrices of both robotic arms (${}^{\mathcal{W}}T_{\mathcal{B}_1}$ and ${}^{\mathcal{W}}T_{\mathcal{B}_2}$). This was previously done through an optical tracking system [4; 6; 22]. However, the requirement of additional equipment and free line of sight between the cameras and markers are not ideal in a clinical environment, and can severely limit the accuracy of results.

In this work, we propose a viable alternative through magnetic localization. By fixing a magnetic field sensor with reference frame $\mathcal{S}$ in the workspace, and taking its pose as the new workspace origin $\mathcal{S} = \mathcal{W}$, this sensor can be localized with respect to each robotic arm one at a time ${}^{\mathcal{B}_1}T_W$ and ${}^{\mathcal{B}_2}T_W$. This sensor can be embedded in a device which is not responsive to magnetic fields, or be embedded in a magnetically actuated device and ensuring these calibration fields are low in intensity. From here on we describe the methodology for a generic robotic arm, repeating the process for every robotic arm present in the system.

5.4.1 Observer

For the calibration of the dEPM we consider only magnetic field measurements and no IMU. This limits the required hardware for the calibration procedure. The goal is to find the relative pose between the sensor and the base of the robotic arm ${}^{\mathcal{B}}T_W$. The homogenous transformation between the robotic arm base and the EPM is assumed to be known and read from the robotic arm encoders. Since only magnetic field measurements are available, the calibration process focuses first on finding the position of the sensor, followed by its orientation.

The position is first estimated by using the measurement model described in eq. (5.23). It is composed of three separate measurements of the magnetic field norm for three different

EPM positions.

$$\mathbf{y_p} = \begin{bmatrix} \|\mathbf{B}_1(\mathbf{p})\| \\ \|\mathbf{B}_2(\mathbf{p})\| \\ \|\mathbf{B}_3(\mathbf{p})\| \end{bmatrix} \tag{5.23}$$

Once the position is estimated, the orientation is subsequently estimated offline, using the same set of measurements but using the magnetic field vector, since its position $\mathbf{p}$ is now known.

$$\mathbf{y}_R = \begin{bmatrix} \mathbf{B}_1(\mathbf{p}, R) \\ \mathbf{B}_2(\mathbf{p}, R) \\ \mathbf{B}_3(\mathbf{p}, R) \end{bmatrix} \tag{5.24}$$

This allows the estimation of the full 6-DOF pose of a static magnetic field sensor where the EPM movements are not used for actuation and purely for localization.

5.4.2 EPM Path

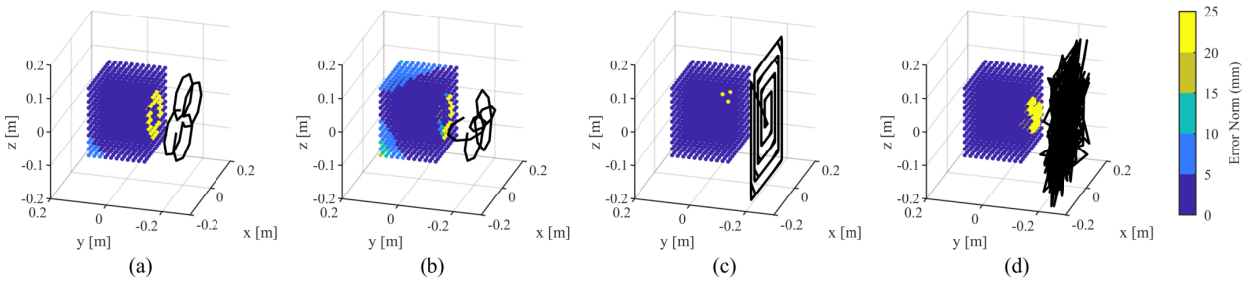

Figure 5.7: Simulated EPM paths (in black) and corresponding error norm for estimation of the position across the workspace, for the calibration of the system. (a) Four circles on plane $y = -0.2$; (b) Four circles across planes $y = -0.2$, $x = 0$ and $z = 0$; (c) Spiral on plane $y = -0.2$; (d) Random path with boundaries $-0.2 < x, z < 0.2$ and $-0.25 < y < -0.2$.

The path the EPM travels has a significant impact on the estimation error across the workspace. Ideally, for the calibration of the system the path should cover as much of the workspace as possible and generate significantly different measurements in order to provide as much information as possible. However, such a path is difficult to achieve in a short amount of time and space. For this reason, four different EPM paths were simulated and the position across the workspace estimated. For all simulated paths, the

EPM was constrained to stay in a single side of the workspace, and all paths had the same number of points, taking between 200 and 300 seconds to complete, assuming a safe EPM speed (30% of maximum speed of the robotic arm, 4 cm/s).

Fig. 5.7 shows the results obtained for the position estimation across the workspace for each path tested. The paths tested were: four planar circles (Fig. 5.7(a)), four circles in different planes (Fig. 5.7(b)), spiral planar motion (Fig. 5.7(c)), and a random planar path (Fig. 5.7(d)). As we can see for all cases, the majority of the workspace is estimated with errors lower than 5 mm. The random movement (Fig. 5.7(d)), despite having the highest level of variety of movement, leads to several points of high error, especially closer to the EPM. The spiral movement (Fig. 5.7(c)), overall, was the movement with the lowest number of points with higher error, and these were concentrated on one of the corners of the workspace. For this reason, this was the path chosen for testing.

5.4.3 Experimental Setup

For the calibration procedure a 3D printed plate with the HE sensor in multiple configurations was placed in the center of the workspace (Fig. 5.8). Optical tracker markers were attached to both the plate and the sensor for ground truth measurements.

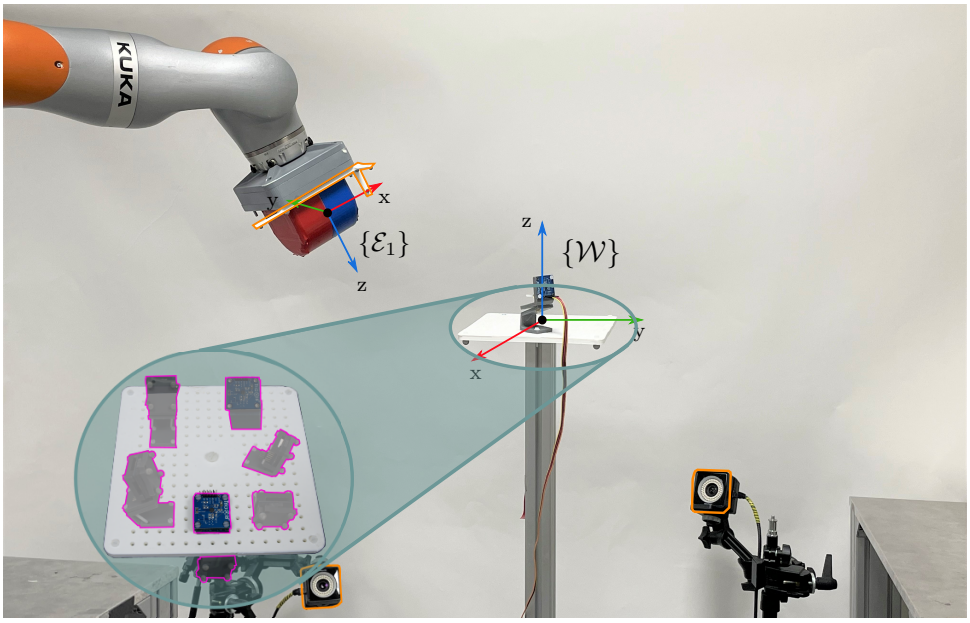

Figure 5.8: Experimental setup for the calibration of the platform. The optical tracker used as benchmark is outlined in orange, and the HE sensor in pink.

5.4.4 Results

The EKF parameters for the position estimation were $P_{P0} = \text{diag}(10I)$, $Q_{Pk} = \text{diag}(0.1I)$ and $R_P = \text{diag}(0.1I)$, with $I \in \mathbb{R}^{3\times3}$ the identity matrix. The EKF parameters for the orientation were $P_{R0} = \text{diag}(1I)$, $Q_{Rk} = \text{diag}(10I)$ and $R_R = \text{diag}(0.001I)$. The position estimate was initialized at the workspace center, and the orientation as the identity matrix. The EPM was moved along a spiral path covering a wide area of the workspace taking 250 seconds. Seven different poses within the workspace were tested (Fig. 5.9(a)). The results for the calibration step are shown in Fig. 5.9(b).

The average error in position norm was 5.3 ± 1.8 mm, with 2.4 ± 1.4 mm along the x axis, 2.9 ± 1.7 mm along y, and 2.8 ± 1.4 mm along z. The final orientation percentage error was 0.14%, with $1.5 \pm 1.3^\circ$ in x, $1.9 \pm 1.4^\circ$ in y, and $3.5 \pm 3.7^\circ$ in z.

5.5 Pose estimation

Once the platform has been calibrated and the poses of the two robotic arms in the global reference frame are known, the SCR can be actuated and localized. The EKF parameters for the estimation of both the orientation and position as described in Section 5.3.4 can be found in Table 5.1. Additionally, as stated earlier the orientation observer needs to be initialized with an accurate estimate R_0. In this work, this was founding using the benchmark data. In a clinical realistic environment, this could be found using static localization methods [22]. The position observer was initialized at the center of the workspace.

Table 5.1: EKF parameters for real-time orientation and position estimation.

	Orientation	**Position**
Initial State	R_0	[0, 0, 0]
State $\mathbf{P_0}$	$\text{diag}(10^{-5}I)$	$\text{diag}(10^{-6}I)$
Input $\mathbf{Q_k}$	$\text{diag}(5^{-2}I)$	$\text{diag}(10^{-5}I)$
Measurement $\mathbf{N_k}$	$\text{diag}(2^{-4}I,\ 3.4^{-8}I)$	$\text{diag}(5^{-4}I)$

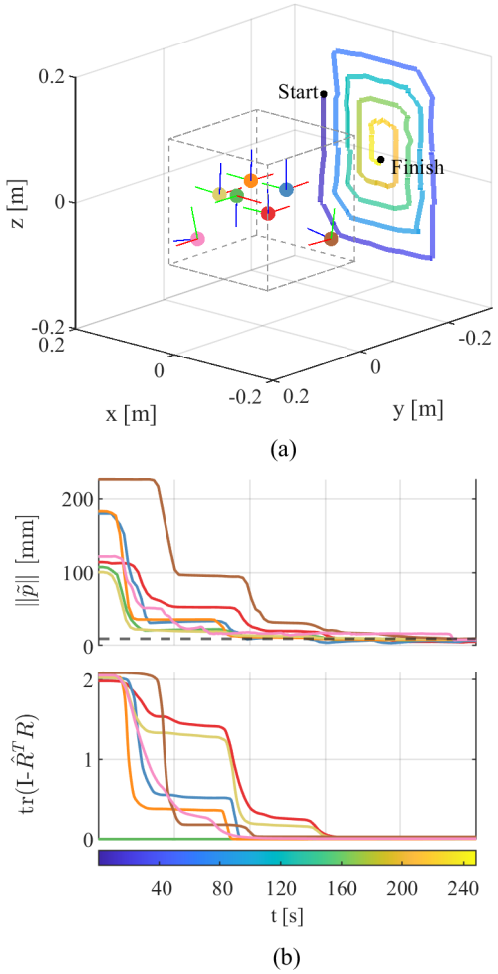

Figure 5.9: Results for calibration procedure. (a) Workspace containing the eight tested points together with the spiral path travelled by the EPM. (b) Error norm in position and orientation for each point vs the EPM path.

5.5.1 Singularity Conditions

As shown in Section 5.2.3, certain configurations of the two EPMs generate singularity regions in which the estimation of the position becomes challenging. As such, alternative EPM configurations which produce the same SCR deflection and tip position need to be found in order not to lose functionality of the SCR while simultaneously avoiding singularity conditions. Given the high non-linearity of the magnetic fields generated by two EPMs, and the flexibility of the dEPM platform, these alternative EPM configurations can be easily achieved.

Figs. 5.10, 5.11, 5.12, and 5.13 show the singularity EPM configuration and the alternative EPM configuration ((a) in green and brown respectively) which produce the same SCR

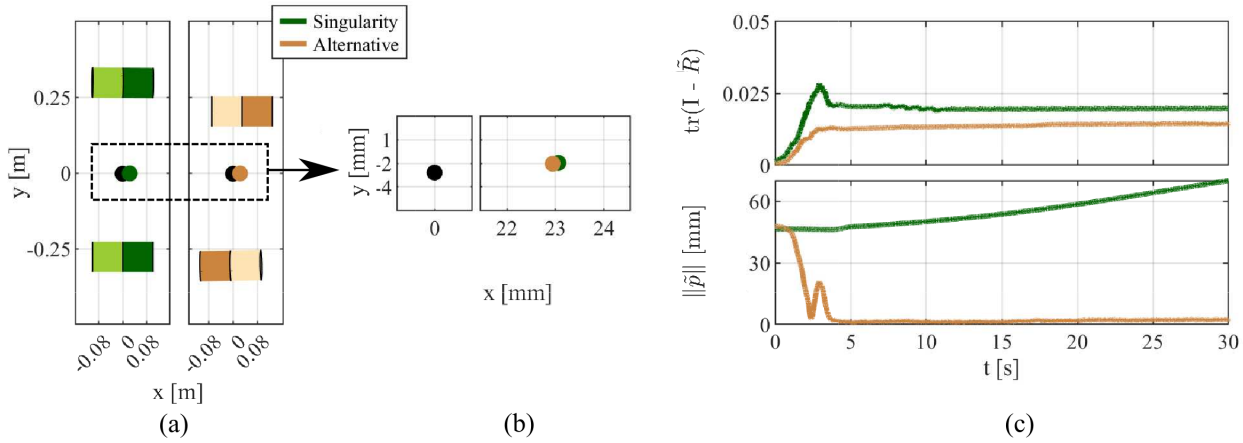

Figure 5.10: Movement along the positive X axis. (a) Shows the two EPM configurations; (b) The position of the continuum robot for the two EPM configurations; (c) Orientation and Position error for the two EPM configurations.

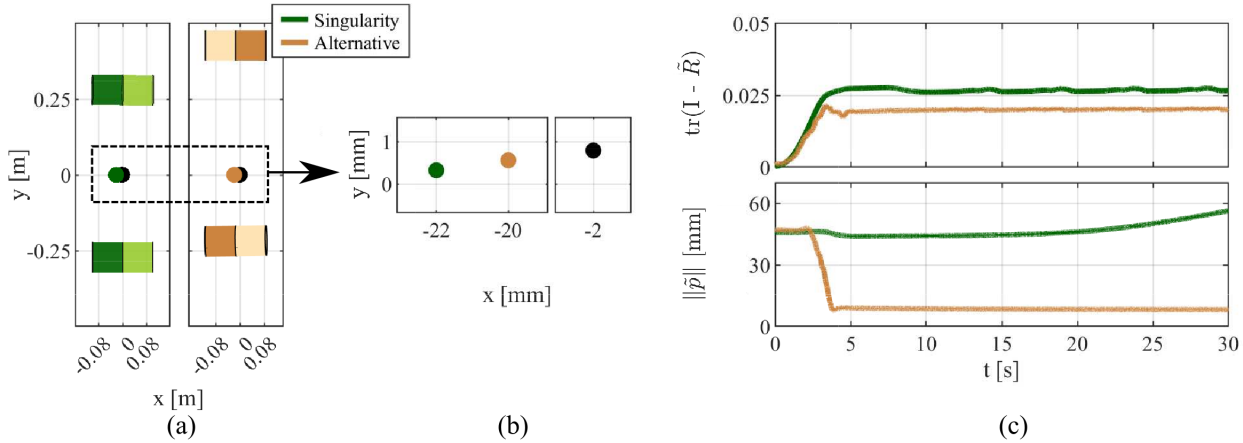

Figure 5.11: Movement along the negative X axis. (a) Shows the two EPM configurations; (b) The position of the continuum robot for the two EPM configurations; (c) Orientation and Position error for the two EPM configurations.

tip deflection ((b), black dot denoting starting SCR tip position), and the localization results for both cases ((c)) (see Suplementary Video 1). The system was initialized (at $t = 0$) with the EPMs away from the workspace, and therefore in the absence of any magnetic field measurements, and the EPMs were moved into their final positions (shown in (a)). We can see, that for the singularity conditions, the observer executed very poorly, not converging to the correct solution, with an average error in position norm of 53.1 ± 20.3 mm. Conversely, the alternative EPM configurations that produced the same SCR deflection yielded much better results, with an average error of 4.5 ± 1.8 mm, converging to the right position in under 10 seconds.

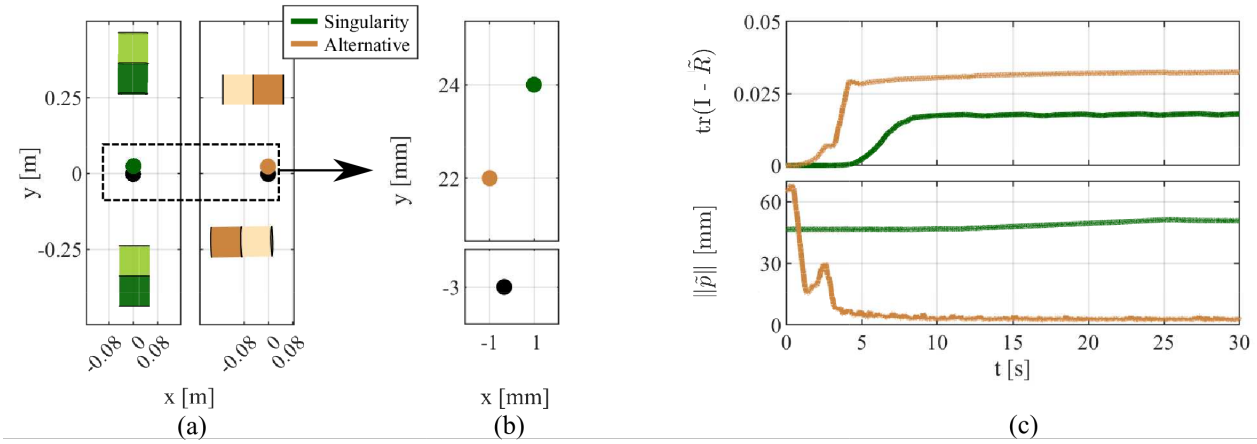

Figure 5.12: Movement along the positive Y axis. (a) Shows the two EPM configurations; (b) The position of the continuum robot for the two EPM configurations; (c) Orientation and Position error for the two EPM configurations.

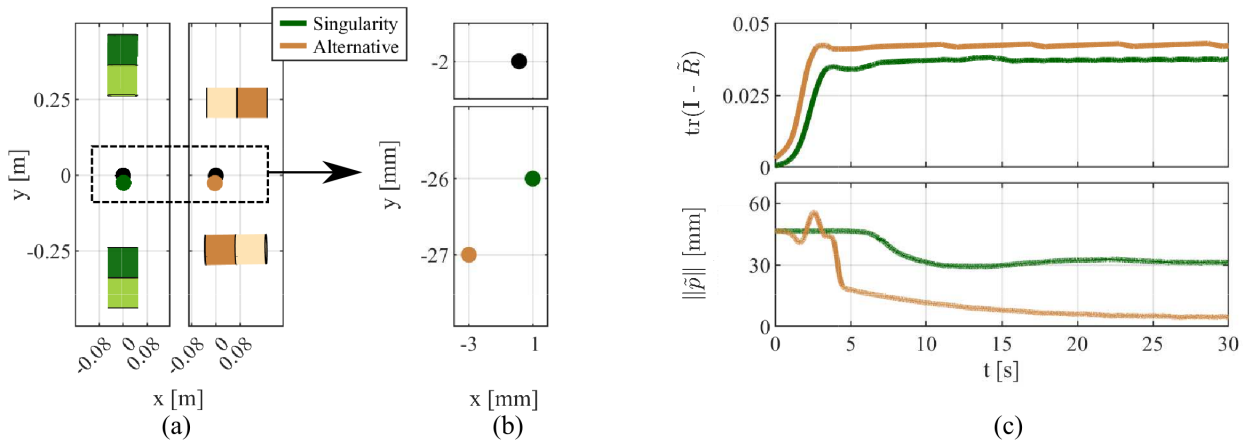

Figure 5.13: Movement along the negative Y axis. (a) Shows the two EPM configurations; (b) The position of the continuum robot for the two EPM configurations; (c) Orientation and Position error for the two EPM configurations.

Since the orientation estimation does not depend on the magnetic field measurements, the errors in orientation were similar across all cases, with an average percentage error of 0.63%, with $1.0 \pm 0.7°$ for x, $0.6 \pm 0.5°$ for y, and $5.2 \pm 0.2°$ for z.

5.5.2 Random Continuous Movement

To analyse the stability of the localization against gyroscope drift and possible momentary singularity regions, the EPMs were moved along random paths while the SCR was actuated freely for a total length of 10.5 min. Fig. 5.14 depicts the full 6-DOF pose estimation results for random movements of the EPMs over the whole time period, together

with the error over time for both the orientation and position. Additionally, an expanded view of the estimated state for the first and last minute can be found in Fig. 5.15. The full time length estimation can be seen in the Supplementary Video 2.

As we can see in Fig. 5.14(b) the observer maintained orientation errors under 1% during the first half of the running time. However, this error increased towards the end, mainly due to inaccurate rotation around gravity (Fig. 5.15(b)). This is expected since there is only a single inertial measurement present in the system, leaving the rotation around gravity to be estimated solely on the biased gyroscope output. This bias, when integrated over time, makes the estimate drift. In this work, this bias was considered constant, and that assumption was enough to maintain an accurate orientation estimate for the first 5 min, with average errors of 0.21%, the equivalent of $2.5 \pm 1.6^\circ$ around x, $1.5 \pm 1.2^\circ$ around y, and $2.8 \pm 2.2^\circ$ around z. However, by the end of the running time, 10 min and 30 seconds, the error of orientation around gravity was of 26.4° increasing the error in the orientation estimation up to 5.2%.

When looking at the position estimation, we can see that the observer converged to the right state within the first 15 seconds, with an average error of 3.5 ± 2.7 mm in norm after convergence during the first 5 min, and of 4.1 ± 3.8 mm for the full time-scale. Additionally, the error spike at the end of the time period is due to the removal of magnetic field when the EPMs are moved away from the workspace. Since the EPMs are travelling along random paths, there are moments of magnetic singularity affecting the estimate of the position. However, we can see that the observer is able to quickly re-converge to the right state. Furthermore, the position errors for the first 5 min are around 58% lower when compared to our previous work [22]. This is due to the fact that the orientation is estimated independently of the position and magnetic field measurements. In our previous work, both the position and orientation estimates are affected by magnetic singularity regions.

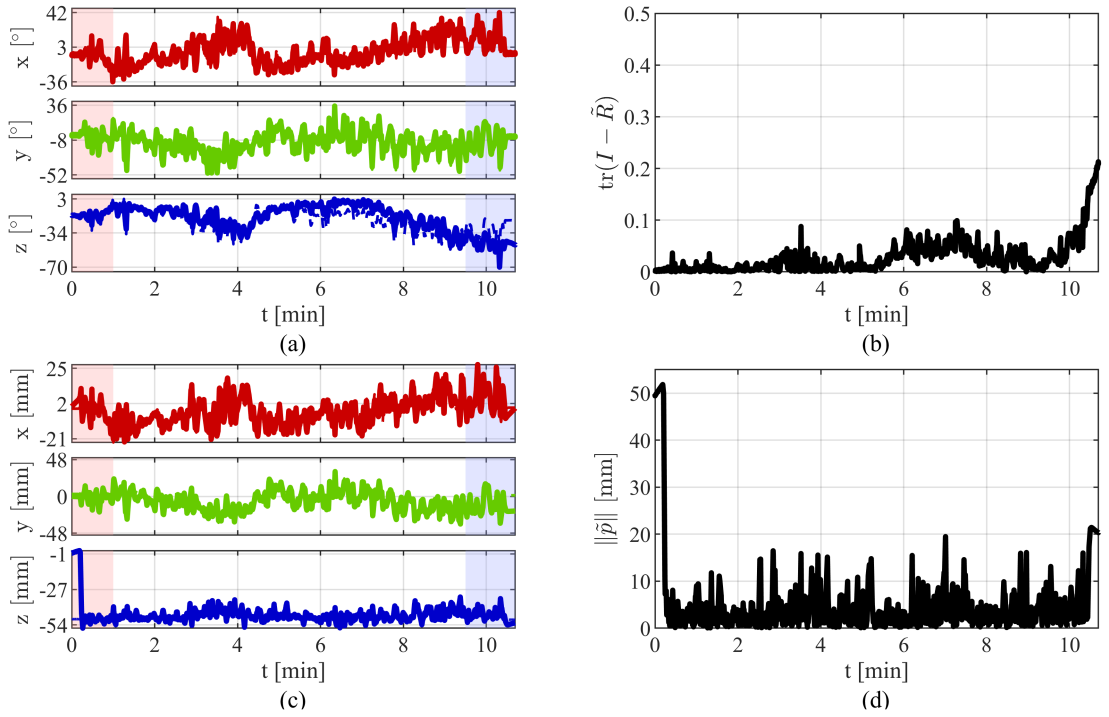

Figure 5.14: Results for the 6-DOF localization for when the EPMs are travelling along random paths. Full lines denote the estimated state against the ground truth data (dashed lines). The estimated rotational angles (a) and the error in the estimation of the rotation matrix (b). The estimated positional values (c), and its corresponding error norm (d).

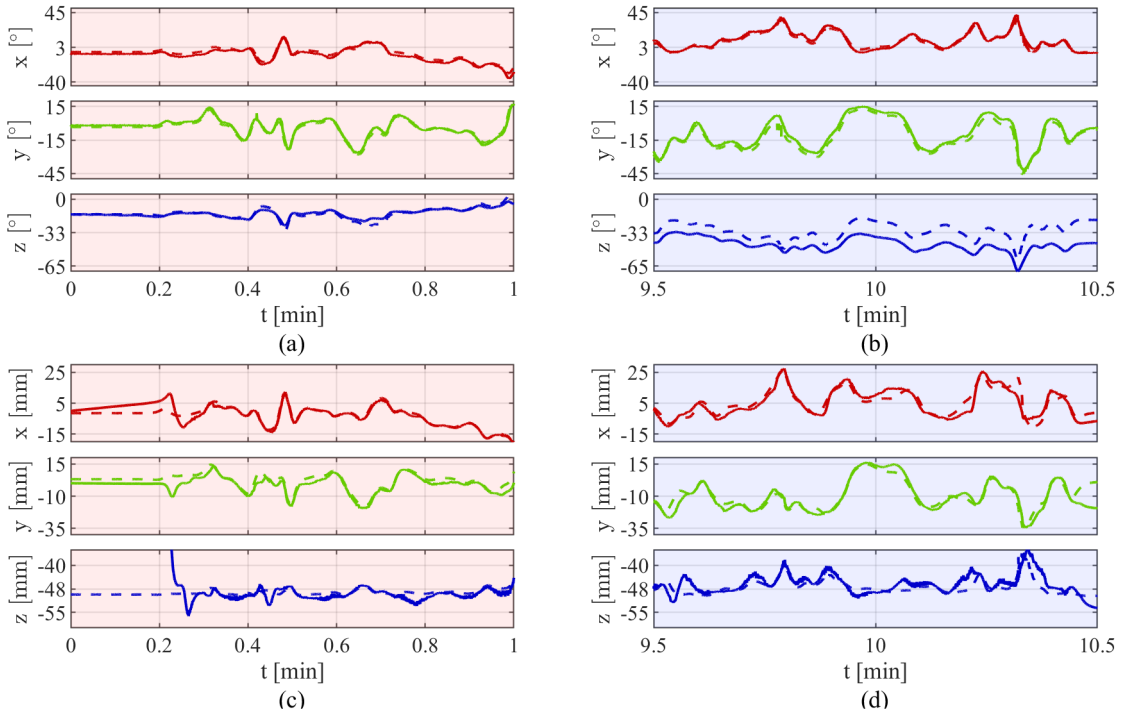

Figure 5.15: Expanded view of the estimated state against ground truth data for the first ((a) and (c)), and last ((b) and (d)) minute.

5.5.3 Maximum Error in Initial State Estimate

A known disadvantage of an EKF is the negative impact the initial estimate of the state may have on the observer's convergence. As expressed in Table 5.1, the initial positional state was defined as the workspace origin, translating into an initial error of 4.9 cm. To evaluate the maximum initial error the observer can withstand and still converge, the localization algorithm was tested against a range of initial state errors.

Figure 5.16 plots the state error at 30 seconds for initial state errors of up to 40 cm. As it can be seen, the observer converges in less than 30 seconds for errors of up to 35 cm. When the error was of 40 cm the observer failed to converge. Given that in this work we assume a cubic workspace of size length of 20 cm, it is expected that the EKF will converge as long as the initial state is inside the workspace.

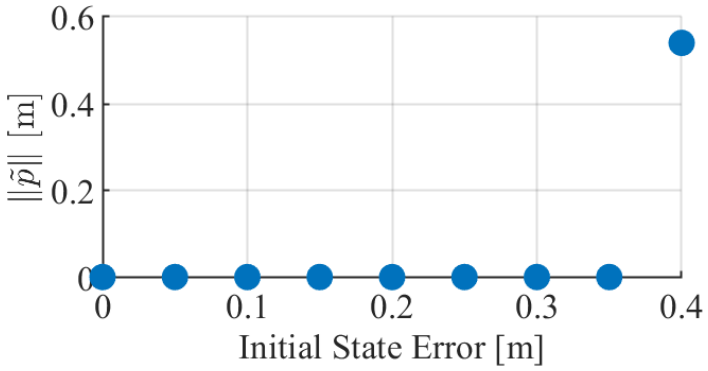

Figure 5.16: Expanded view of the estimated state against ground truth data for the first ((a) and (c)), and last ((b) and (d)) minute.

5.6 Conclusions

In the present work, we introduced a novel approach for the localization of magnetically actuated robots under two EPMs by means of an IMU and magnetic field sensor. We discuss how the relative pose between two EPMs affects the observability of the system and show that alternative EPM configurations ensure localization accuracy without loss of manipulability. Although we have shown the case for two EPMs, the method is easily applicable to additional EPMs, as long as the singularity conditions are studied and

defined.

To ensure accurate localization estimates, the platform needs to be calibrated, i.e. the relative pose between the EPMs must be known. In this work, we proposed a calibration method that relies on a single triaxial magnetic field sensor and sees the EPM travel an optimized path to ensure the whole workspace of $20 \times 20 \times 20$ cm^3 is accurately calibrated.

We tested our localization technique on a SCR and showed that we are able to accurately track the SCR tip across the workspace in real-time. Overall, the localization achieved errors of 3.5 mm in position norm and 0.21% in orientation, with an error of 2.8° for rotation around gravity during the first five minutes of running. These are comparable to previous magnetic localization works. Additionally, the refresh rate of the proposed algorithm was 280 Hz, thus enabling closed-loop control strategies. In this work the orientation is estimated independently from the position. This was achieved by using accelerometer and gyroscope measurements and applying a common observer in the special orthogonal group. This has the advantage of the orientation estimate being unaffected by the movements of the EPMs maintaining an accurate estimate even during possible singularity regions. However, it requires accurate initialization and it drifts over time due to the gyroscope bias. Since the estimation of the position relies on the orientation being known, orientation errors will eventually affect the estimation of the position. A solution is to initialize and reset the orientation estimate every few minutes by applying a static localization method [22].

Future work will see the inclusion of the SCR model to predict its actuation given the EPMs poses. This, alongside the gyroscope and accelerometer measurements, is expected to produce a drift-free orientation estimate. Additionally, EPM path-planning to avoid singularity conditions while maintaining accurate SCR actuation will be implemented which will further improve the localisation results.

Bibliography

[1] T. Xu, J. Zhang, M. Salehizadeh, O. Onaizah, and E. Diller, "Millimeter-scale flexible robots with programmable three-dimensional magnetization and motions," *Science Robotics*, vol. 4, no. 29, p. eaav4494, 2019.

[2] W. Hu, G. Z. Lum, M. Mastrangeli, and M. Sitti, "Small-scale soft-bodied robot with multimodal locomotion," *Nature*, vol. 554, no. 7690, pp. 81–85, 2018.

[3] S. Salmanipour, O. Youssefi, and E. D. Diller, "Design of multi-degrees-of-freedom microrobots driven by homogeneous quasi-static magnetic fields," *IEEE Transactions on Robotics*, vol. 37, no. 1, pp. 246–256, 2020.

[4] G. Pittiglio, M. Brockdorff, T. da Veiga, J. Davy, J. H. Chandler, and P. Valdastri, "Collaborative magnetic manipulation via two robotically actuated permanent magnets," *IEEE Transactions on Robotics*, 2022.

[5] J. Davy, T. Da Veiga, G. Pittiglio, J. H. Chandler, and P. Valdastri, "Independent control of two magnetic robots using external permanent magnets: A feasibility study," in *2023 International Symposium on Medical Robotics (ISMR)*, pp. 1–7, IEEE, 2023.

[6] G. Pittiglio, P. Lloyd, T. da Veiga, O. Onaizah, C. Pompili, J. H. Chandler, and P. Valdastri, "Patient-specific magnetic catheters for atraumatic autonomous endoscopy," *Soft Robotics*, 2022.

[7] Y. Kim, G. A. Parada, S. Liu, and X. Zhao, "Ferromagnetic soft continuum robots," *Science Robotics*, vol. 4, no. 33, p. eaax7329, 2019.

[8] Y. Kim, E. Genevriere, P. Harker, J. Choe, M. Balicki, R. W. Regenhardt, J. E. Vranic, A. A. Dmytriw, A. B. Patel, and X. Zhao, "Telerobotic neurovascular interventions with magnetic manipulation," *Science Robotics*, vol. 7, no. 65, p. eabg9907, 2022.

[9] L. Barducci, B. Scaglioni, J. Martin, K. L. Obstein, and P. Valdastri, "Active sta-

bilization of interventional tasks utilizing a magnetically manipulated endoscope," *Frontiers in Robotics and AI*, vol. 9, 2022.

[10] L. Barducci, G. Pittiglio, J. C. Norton, K. L. Obstein, and P. Valdastri, "Adaptive dynamic control for magnetically actuated medical robots," *IEEE robotics and automation letters*, vol. 4, no. 4, pp. 3633–3640, 2019.

[11] G. Pittiglio, A. L. Orekhov, T. da Veiga, S. Calò, J. H. Chandler, N. Simaan, and P. Valdastri, "Closed loop static control of multi-magnet soft continuum robots," *IEEE Robotics and Automation Letters*, 2023.

[12] J. W. Martin, B. Scaglioni, J. C. Norton, V. Subramanian, A. Arezzo, K. L. Obstein, and P. Valdastri, "Enabling the future of colonoscopy with intelligent and autonomous magnetic manipulation," *Nature machine intelligence*, vol. 2, no. 10, pp. 595–606, 2020.

[13] J. C. Norton, P. R. Slawinski, H. S. Lay, J. W. Martin, B. F. Cox, G. Cummins, M. P. Desmulliez, R. E. Clutton, K. L. Obstein, S. Cochran, *et al.*, "Intelligent magnetic manipulation for gastrointestinal ultrasound," *Science robotics*, vol. 4, no. 31, p. eaav7725, 2019.

[14] F. Bianchi, A. Masaracchia, E. Shojaei Barjuei, A. Menciassi, A. Arezzo, A. Koulaouzidis, D. Stoyanov, P. Dario, and G. Ciuti, "Localization strategies for robotic endoscopic capsules: a review," *Expert review of medical devices*, vol. 16, no. 5, pp. 381–403, 2019.

[15] S. Pane, G. Faoro, E. Sinibaldi, V. Iacovacci, and A. Menciassi, "Ultrasound acoustic phase analysis enables robotic visual-servoing of magnetic microrobots," *IEEE Transactions on Robotics*, vol. 38, no. 3, pp. 1571–1582, 2022.

[16] P. E. Dupont, B. J. Nelson, M. Goldfarb, B. Hannaford, A. Menciassi, M. K. O'Malley, N. Simaan, P. Valdastri, and G.-Z. Yang, "A decade retrospective of medical robotics research from 2010 to 2020," *Science Robotics*, vol. 6, no. 60, p. eabi8017, 2021.

[17] T. da Veiga, J. H. Chandler, P. Lloyd, G. Pittiglio, N. J. Wilkinson, A. K. Hoshiar, R. A. Harris, and P. Valdastri, "Challenges of continuum robots in clinical context: a review," *Progress in Biomedical Engineering*, vol. 2, no. 3, p. 032003, 2020.

[18] K. M. Popek, T. Schmid, and J. J. Abbott, "Six-degree-of-freedom localization of an untethered magnetic capsule using a single rotating magnetic dipole," *IEEE Robotics and Automation Letters*, vol. 2, no. 1, pp. 305–312, 2016.

[19] A. Z. Taddese, P. R. Slawinski, M. Pirotta, E. De Momi, K. L. Obstein, and P. Valdastri, "Enhanced real-time pose estimation for closed-loop robotic manipulation of magnetically actuated capsule endoscopes," *The International journal of robotics research*, vol. 37, no. 8, pp. 890–911, 2018.

[20] D. Son, X. Dong, and M. Sitti, "A simultaneous calibration method for magnetic robot localization and actuation systems," *IEEE Transactions on Robotics*, vol. 35, no. 2, pp. 343–352, 2019.

[21] C. Fischer, Q. Boehler, and B. J. Nelson, "Using magnetic fields to navigate and simultaneously localize catheters in endoluminal environments," *IEEE Robotics and Automation Letters*, 2022.

[22] T. da Veiga, G. Pittiglio, M. Brockdorff, J. H. Chandler, and P. Valdastri, "Six-degree-of-freedom localization under multiple permanent magnets actuation," *arXiv:2303.11059*, 2023.

[23] D. Son, X. Dong, and M. Sitti, "A simultaneous calibration method for magnetic robot localization and actuation systems," *IEEE Transactions on Robotics*, vol. 35, no. 2, p. 343–352, 2019.

[24] Q. Boehler, S. Gervasoni, S. L. Charreyron, C. Chautems, and B. J. Nelson, "On the workspace of electromagnetic navigation systems," *IEEE Transactions on Robotics*, 2022.

[25] F. Carpi and C. Pappone, "Stereotaxis niobe® magnetic navigation system for en-

docardial catheter ablation and gastrointestinal capsule endoscopy," *Expert review of medical devices*, vol. 6, no. 5, pp. 487–498, 2009.

[26] P. Ryan and E. Diller, "Magnetic actuation for full dexterity microrobotic control using rotating permanent magnets," *IEEE Transactions on Robotics*, vol. 33, no. 6, p. 1398–1409, 2017.

[27] B. J. Nelson, S. Gervasoni, P. W. Chiu, L. Zhang, and A. Zemmar, "Magnetically actuated medical robots: An in vivo perspective," *Proceedings of the IEEE*, 2022.

[28] C. Fischer, T. Quirin, C. Chautems, Q. Boehler, J. Pascal, and B. J. Nelson, "Gradiometer-based magnetic localization for medical tools," *IEEE Transactions on Magnetics*, 2022.

[29] C. Di Natali, M. Beccani, N. Simaan, and P. Valdastri, "Jacobian-based iterative method for magnetic localization in robotic capsule endoscopy," *IEEE Transactions on Robotics*, vol. 32, no. 2, pp. 327–338, 2016.

[30] A. J. Petruska and J. J. Abbott, "Optimal permanent-magnet geometries for dipole field approximation," *IEEE transactions on magnetics*, vol. 49, no. 2, pp. 811–819, 2012.

[31] R. Mahony, T. Hamel, and J.-M. Pflimlin, "Nonlinear complementary filters on the special orthogonal group," *IEEE Transactions on automatic control*, vol. 53, no. 5, pp. 1203–1218, 2008.

[32] G. Pittiglio, S. Calo, and P. Valdastri, "On the observability and observer design on the special orthogonal group based on partial inertial sensing," *IEEE Transactions on Automatic Control*, 2020.

[33] T. Da Veiga, J. H. Chandler, G. Pittiglio, P. Lloyd, M. Holdar, O. Onaizah, A. Alazmani, and P. Valdastri, "Material characterization for magnetic soft robots," in *2021 IEEE 4th International Conference on Soft Robotics (RoboSoft)*, pp. 335–342, IEEE, 2021.

Chapter 6

Discussion

Given this highly intricate panorama, a literature review on this topic was of high necessity in order to analyse and compare the recent developments in the area, but also to highlight these active areas of research that are fundamental for the full realisation of these devices. Chapter 2 does just that. Published in 2020, this chapter provides a thorough literature review on the topic of medical continuum robots, by offering a critical analysis of different actuation modes (magnetic, pneumatic and mechanical) against the development of fabrication, modelling, control, and sensing strategies. By identifying the current gaps in the literature, this chapter paves the way for the research work done and presented in the subsequent chapters.

With the ultimate goal in mind of a fully autonomous magnetic soft continuum robot, the first fundamental lack of knowledge I found pertained to the robot's behaviour itself, i.e. the properties of the materials used in these devices were not known. This is crucial for reliable and accurate actuation as it will dictate how strong of a magnetic field should be generated in order to deflect and move the robot. With this goal in mind, Chapter 3, published in 2021, sets out a characterisation methodology for these materials, both from a mechanical and magnetic perspective, providing a modelling and simulation solution for magnetically actuated soft robots. This allowed me to understand what concentrations of magnetic particles are feasible and useful for different soft elastomers, while at the same

time, understanding what strength of magnetic fields are necessary to achieve meaningful deflection and actuation.

Now that the behaviour of the continuum robot under an external magnetic field is well defined, the focus can be shifted towards actuation and pose tracking. To this end, a significant amount of work on the development of a magnetic actuation platform for soft continuum robots was first carried out [1; 2; 3]. While these works are not extensively described in the body of this thesis, they provide the foundation of the development of the dual External Permanent Magnet platform (dEPM) upon which the pose tracking work was built. To track the tip pose of a SCR, multiple solutions could be considered, such as imaging techniques or electromagnetic tracking. However, these tend to either be harmful for the patient, or not work reliably enough with magnetically actuated soft continuum robots. The use of the magnetic actuation systems for simultaneous actuation and localisation has, therefore, grown as it provides a cheap and safe way to track in real-time the pose of a device within the actuation workspace. In fact, the embodiment of magnetic field sensors together with an inertial measurement unit (IMU) has been in place for capsule robots for a few years, while it is now starting to make its way to continuum robots.

One of the main hurdles of estimating the full position and orientation by means of a magnetic field sensor together with an IMU is the absence of the Earth's magnetic field measurement. In other applications, the Earth's magnetic field is used as an inertial measurement. However, in magnetic actuation platforms, the magnetic field measurements are not constant and they overpower the Earth's magnetic field, effectively eliminating that inertial measurement for orientation reference. A possible work-around to this is the integration of gyroscope measurements over time. However, this is prone to drift as it compounds the measurement noise, quickly leading to wrong estimates. In Chapter 4 I address this issue by making use of multiple measurements of the magnetic field for different poses of the external permanent magnets. While this allowed the full 6-DOF estimation of the pose of the SCR it can only be used in static or slow-moving SCR as it assumes that the SCR has remained static across the multiple magnetic field measure-

ments. Additionally, in this work I also explored the relationship between multiple EPMs and the effectiveness of magnetic localisation, and I concluded that any additional EPMs beyond two has little to no effect in the accuracy of the localisation estimation. This chapter, then, answers the questions "How can I estimate the full 6-DOF pose?" and "How many EPMs are needed to do so effectively?".

With these questions answered, and with the SCR and its materials properties and behaviour described in Chapter 3 I was, then, in a position where I could develop a pose estimation algorithm for SCRs actuated under multiple EPMs, which is presented in Chapter 5, however in order to get a few additional details are needed in terms of singularity regions, localisation algorithm, and limitations in miniaturisation.

One of the main differences when it comes to magnetic localisation with 1 vs multiple EPMs is the fact that the singularity regions of the magnetic field are not constant. Whereas a single EPM has well defined singularity regions, the relative pose between multiple EPMs affects the resulting magnetic field leading to relative singularity regions where localisation is not possible. In Chapter 5 I started by exploring this concept and defining singularity regions which should be avoided during actuation in order to maintain observability and accurate pose estimations.

Another key element in magnetic localisation is the algorithm used. Several methods have been shown as previously discussed, from offline maps to particle filters. In this work, I explored the use of Extended Kalman Filters (EKF) as these are widely used in other state estimatino problems and have the advantage of being less computationally expensive when compared to particle filters leading to higher refresh rates. However, unlike particle filter, they require an initial estimate which could impact the performance of the observer. Additionally, it also requires the definition of several parameters such as state and measurement covariance matrices which also impact the the observer performance. In Chapter 5, I showed how an EKF can indeed be used in magnetic localisation algorithms, being comparable in localisation accuracy to results previously obtained with a particle filter [4] for a single EPM, with the advantage of higher refresh rates (280 Hz

vs 100 Hz).

Lastly, two final consideration need to be made regarding fabrication and scalability. With the goal of reaching deeper inside the human body in a minimally invasive way, these SCR should be able to be scaled down as small as possible. However, the inclusion of magnetic field and inertial sensors limits the minimum possible size. Current chips allow a minimum diameter of 6 mm which is compatible with several minimally invasive procedures, such as gastroscopy for example. However, advances in sensor chip design and manufacture will futher reduce footprints size while maintaining the required sensitivity and accuracy for this application. Additionally, research in soft stretchable sensors will possibly allow the direct fabrication of SCR utilising sensorised materials, bypassing the need of hard chips. Another aspect to consider is the fact that the SCR is magnetic itself, thus generating an internal magnetic field. This means that the embedded magnetic field sensor will measure this internal field in addition to the external fields for actuation. In Chapter 6 I evaluated this effect for the current design and saw that this internal field was constant across deflections. However, for more intricate SCR design, or for more sensitive sensors, a more robust model on how the current SCR deflection affects the readings of this internal magnetic field will be needed to further reduce localisation errors.

To summarise the discussion, I started by looking into the literature and identifying the gaps and active areas of research in magnetically actuated soft continuum robots. In doing so, I realised that there was a lack of knowledge on the magnetic materials - which was hindering their simulation and actuation accuracy - and that magnetic localisation methods had stalled and were not keeping up with newer magnetic actuation platforms. Given this, I started by carrying out a material characterisation which provided me with information on how to fabrication such devices and what kind of magnetic fields/concentrations are needed in order to generate meaningful deflections and actuation. Knowing this, I started looking into localisation methods based on multiple EPMs. I looked into how multiple EPMs affect the localisation accuracy, and developed a localisation algorithm based on EKF which achieved compare localisation accuracy to single EPM systems but with 2.8 times higher refresh rates.

Bibliography

[1] G. Pittiglio, M. Brockdorff, T. da Veiga, J. Davy, J. H. Chandler, and P. Valdastri, "Collaborative magnetic manipulation via two robotically actuated permanent magnets," *IEEE Transactions on Robotics*, 2022.

[2] G. Pittiglio, P. Lloyd, T. da Veiga, O. Onaizah, C. Pompili, J. H. Chandler, and P. Valdastri, "Patient-specific magnetic catheters for atraumatic autonomous endoscopy," *Soft Robotics*, 2022.

[3] J. Davy, T. Da Veiga, G. Pittiglio, J. H. Chandler, and P. Valdastri, "Independent control of two magnetic robots using external permanent magnets: A feasibility study," in *2023 International Symposium on Medical Robotics (ISMR)*, pp. 1–7, IEEE, 2023.

[4] A. Z. Taddese, P. R. Slawinski, M. Pirotta, E. De Momi, K. L. Obstein, and P. Valdastri, "Enhanced real-time pose estimation for closed-loop robotic manipulation of magnetically actuated capsule endoscopes," *The International journal of robotics research*, vol. 37, no. 8, pp. 890–911, 2018.

Chapter 7

Conclusions

In the present thesis, the main goal was to develop a magnetically actuated SCR compatible with closed-loop control for minimally invasive surgery. To this end, material design, fabrication, and pose estimation algorithms were developed and implemented. As surgical robots move towards soft, flexible, and continuum designs, several challenges in their development and adoption still need to be address to make them a fully realised reality.

Difficulties in modelling and simulating such soft magnetically actuated structures are well documented. In an attempt to ease their implementation and validation, and to further reduce errors between simulation and reality, a material characterisation of commonly employed magnetic elastomers was introduced and described in Chapter 3. This was done at a time when information on these materials was lacking, leading to the use of theoretical material parameters - or even those of their non-magnetic counterparts - in modelling and simulation. The characterisation consisted first on tensile testing and evaluating the materials' stress-strain curves. These were fitted to a series of hyperelastic models, and it was observed that higher-order models, such as Ogden with 3 terms and Polynomial with 5 terms, exhibited the best results with the lowest fitting errors. Additionally, with increasing magnetic content, there was a reduction in the hyperelastic behaviour of the materials. The materials were also characterised in magnetic terms. For this, a

platform based on a load cell for the estimation of the material's magnetic remanence was developed. Lastly, to evaluate the effect the material parameters have on the simulation and modelling of magnetically actuated SCR, two different types of SCR were fabricated and actuated under uniform magnetic fields. The use of the material parameters led to a reduction of 37% when compared to using theoretical parameters. This vastly highlights the need for better material characterisation, especially when dealing with new and novel types of soft elastomers, in order to ensure accurate modelling and simulations.

With material and fabrication of magnetically actuated SCR completed, localisation of such devices was the next big challenge to tackle. This is a fundamental aspect as it allows for closed-loop control, autonomous navigation, and delivery of functionality. As such, significant progress has been made on the topic. However, new actuation platforms to address the actuation challenge of SCR have been emerging based on multiple magnetic field sources, such as multiple external permanent magnets (EPMs) [1] or multiple electromagnets [2]. This has made a lot of the previous localisation work not applicable to SCR as these works have largely been based on a single EPM. Therefore, new localisation strategies which take into account the additional magnetic field sources in the workspace are needed to fully localise a SCR under actuation.

In Chapter 4, the concept of localisation with respect to multiple EPMs is first introduced. This localisation takes inspiration from previous works in using the output from an accelerometer and magnetic field sensor as measurements. The main goal was to be able to estimate the full 6-DOF pose of a SCR without any prior pose information. In a realistic clinical scenario, prior pose information is not readily available, especially when the SCR is inside the patient's body. This is a challenging task. Traditional methods rely on the Earth's magnetic field for attitude estimation, however, such measurement is not available in magnetic actuation systems. This problem was solved by taking multiple measurements of the magnetic field for different configurations of the EPMs. It was showed that with at least two magnetic field measurements plus gravity, the estimation of the full 6-DOF pose is possible. Additionally, the effect that multiple EPMs have on the stability of the localisation method was analysed. It was shown that when multi-

ple EPMs are present in the workspace, the localisation method converges faster when compared to a single EPM. However, beyond two EPMs no difference was seen. This indicates that two EPMs are enough, from a localisation perspective, to generate highly non-linear magnetic fields and field gradients to ensure accurate localisation. When only one EPM is present, the magnetic field generated is symmetric about the EPMs axis, taking longer to converge. Due to the need of multiple magnetic field measurements for different EPM configurations for each iteration of the localisation observer, the estimation update rate is slower than desirable, being incompatible with fast moving SCR. However, this localisation method is able to fully localise quasi-static devices without any prior pose information. The estimated state can then be passed on a faster localisation method.

Chapter 5 sees the development of a second localisation technique which is capable of running in real-time, being compatible with fast moving robots and closed loop control. A SCR was fabricated following the techniques and findings described in Chapter 3 and by incorporating an accelerometer, gyroscope, and magnetic field sensor. In order to be compatible with real-time and fast actuation, this method only takes a single measurement of the magnetic field and therefore requires the accurate initialisation of the rotation around gravity. This can be easily achieved with the localisation method introduced in Chapter 4. Additionally, this Chapter sees the definition of the singularity regions for when two EPMs are present in the workspace. Single EPM platforms have constant and well-defined singularity regions. However, when multiple EPMs are present, these regions change depending on the EPMs relative pose. It was shown that localisation within those singularity regions is challenging, but that alternative EPM configurations which produce the same SCR deflection are possible to localise in. This shows that EPM paths should be optimised for actuation and localisation together in order to ensure accurate localisation throughout the surgical procedure.

Future Work

The work presented in this thesis mainly aims at providing a technical innovation to challenges in the development of soft continuum magnetic robots. By developing material

characterisation methodologies, and localisation techniques intended for SCR under multiple EPM control, this thesis allows the further development of these devices to provide better and safer surgical procedures in a minimally invasive way.

Future work will see the development of closed-loop control strategies based on the localisation developed. This together with EPM path planning and optimisation for avoiding the singularity conditions defined will allow for autonomous navigation and deployment of the next generation of SCR.

Given the continuous nature of continuum robots, full shape sensing and localisation is the final goal. The use of fibre Bragg grating sensors for shape sensing is a solution. However, this technology does not provide localisation information, and can be prohibitively expensive. The sensing strategy developed can be deployed along the full length of the SCR to allow full shape sensing and localisation. This can be integrated with a SCR model based on the material parameters defined to further increase actuation and control accuracy. Additionally, as MEMS technology evolves and new and smaller ICs become available, the sensing strategy developed can be further reduced and miniaturised. Indeed, sensors with different footprint, sensitivity, and sensing range can be used when clear application and requirements are known - such as maximum magnetic field applied and SCR diameter. As research in the development of soft sensors gains momentum, the direct use of sensorised materials in the fabrication of SCR will allow seamless localisation and shape sensing.

Lastly, localisation of such devices will enable delivery of functionality. SCR can the be a vessel for virtually any kind of functionality as long as there is a clinical need. Reaching deeper inside the anatomy in a minimally invasive way for better diagnostic or treatment procedures has long been a motivation of SCR. The embedding of an ultrasound probe at the SCR tip would allow the autonomous navigation of such probe. This could be used for ultrasound diagnostics, and or photo-accoustic imaging with a second SCR containing a laser ablation fibre.

Bibliography

[1] G. Pittiglio, M. Brockdorff, T. da Veiga, J. Davy, J. H. Chandler, and P. Valdastri, "Collaborative magnetic manipulation via two robotically actuated permanent magnets," *IEEE Transactions on Robotics*, 2022.

[2] Q. Boehler, S. Gervasoni, S. L. Charreyron, C. Chautems, and B. J. Nelson, "On the workspace of electromagnetic navigation systems," *IEEE Transactions on Robotics*, 2022.